

# IMFUFA **tekst**

- I, OM OG MED MATEMATIK OG FYSIK

## **Small Scale Drum Setup for Measuring Rolling Resistance**

Development of a New Drum Setup Capable  
of Model Testing

Morten Lau Larsen  
IMFUFA, Roskilde University  
Phd thesis

**nr. 518 – 2022**

Roskilde University,  
Department of Science and Environment, IMFUFA  
P.O. Box 260, DK - 4000 Roskilde  
E-mail: imfufa@ruc.dk



## **Small Scale Drum Setup for**

### **Measuring Rolling Resistance**

Development of a New Drum Setup Capable of Model Testing

Morten Lau Larsen  
IMFUFA, Roskilde University  
Phd thesis

IMFUFA tekst nr. 518/2022 — 154 sider — ISSN: 0106-6242

---

In this thesis, we measure the rolling resistance on different surface textures by using two simplified experimental drum test rigs (version 1 and version 2). Version 2 is based on version 1, introducing several improvements, which make up a big part of the thesis. The aim of the test rigs is to validate models of rolling resistance, by measuring rolling resistance using a small internal drum under controlled circumstances.

We use three solid and a single pneumatic wheel, with a diameter of 114 mm – 150 mm for the measurements. The surface textures we use are five types of sandpaper at different grit sizes, and ten 3D printed surfaces with different geometric patterns. The 3D printed surfaces consist of a ramp pattern and identical cuboids on a regular square array.

The measurements show both test rigs are capable of repeatable results, with clear improvements for version 2. All the tested wheels indicate an increased rolling resistance coefficient for larger surface textures and rolling speeds.

In connection with model validation, we develop a simple rolling resistance model based on the energy in a spring, which predicts an inversely proportional relation between "peak fraction" and rolling resistance. Using the measurements from different surface textures we investigate the correlation of rolling resistance with the peak fraction and MPD. Based on these measurements we observe no correlation between MPD and rolling resistance, whereas peak fraction is, to some extent, capable of predicting the rolling resistance.

We conclude that this simplified experimental approach, under controlled circumstances, is able to obtain good accuracy and repeatability, and is useful for developing and validating rolling resistance models.

---

---

# Small Scale Drum Setup for Measuring Rolling Resistance

---

---

DEVELOPMENT OF A NEW DRUM SETUP CAPABLE OF MODEL TESTING

AUTHOR

MORTEN L. LARSEN

SUPERVISORS

TINA HECKSHER

ASSOCIATE PROFESSOR

JEPPE C. DYRE

PROFESSOR



PH.D. THESIS

*IMFUFA, DEPARTMENT OF SCIENCE AND ENVIRONMENT*

*ROSKILDE UNIVERSITY, DENMARK*

DECEMBER 2021



# English Abstract

In this thesis, we measure the rolling resistance on different surface textures by using two simplified experimental drum test rigs (version 1 and version 2). Version 2 is based on version 1, introducing several improvements, which make up a big part of the thesis. The aim of the test rigs is to validate models of rolling resistance, by measuring rolling resistance using a small internal drum under controlled circumstances.

We use three solid and a single pneumatic wheel, with a diameter of 114 mm – 150 mm for the measurements. The surface textures we use are five types of sandpaper at different grit sizes, and ten 3D printed surfaces with different geometric patterns. The 3D printed surfaces consist of a ramp pattern and identical cuboids on a regular square array.

The measurements show both test rigs are capable of repeatable results, with clear improvements for version 2. All the tested wheels indicate an increased rolling resistance coefficient for larger surface textures and rolling speeds.

In connection with model validation, we develop a simple rolling resistance model based on the energy in a spring, which predicts an inversely proportional relation between “peak fraction” and rolling resistance. Using the measurements from different surface textures we investigate the correlation of rolling resistance with the peak fraction and MPD. Based on these measurements we observe no correlation between MPD and rolling resistance, whereas peak fraction is, to some extent, capable of predicting the rolling resistance.

We conclude that this simplified experimental approach, under controlled circumstances, is able to obtain good accuracy and repeatability, and is useful for developing and validating rolling resistance models.

## Danish Abstract

I denne afhandling måles rullemodstand på forskellige overfladeteksturer ved brug af to forenklede eksperimentelle tromleopstillinger (version 1 og version 2). Af de to opstillinger er version 2 en videreudvikling af version 1. Videreudviklingen udgør en større del af afhandlingen. Opstillingerne har til formål at kunne validere rullemodstandsmodeller, ved at måle rullemodstand på en lille indvendig tromle under kontrollerbare forhold.

Til målingerne benyttes tre solide, og et enkelt pneumatisk hjul med diameter 114 mm – 150 mm. Som overfladeteksturer benyttes fem typer sandpapir med forskellig kornstørrelse og ti 3D printede overflader med forskellige geometriske mønstre. De 3D printede overflader består af en gentagende rampe og gentagne bokse med fast mellemrum.

Målingerne viser, at opstillingerne kan producere repeterbare resultater, med en klar forbedring i reproducerbarheden for version 2. For alle anvendte hjul og overflader, indikerer målingerne, at rullemodstandskoefficienten stiger for større overfladeteksturer og rullehastighed.

I forbindelse med modelvalidering, udvikles en simpel rullemodstandsmodel baseret på energien i en fjeder, som forudser en omvendt proportional sammenhæng mellem “peak fraction” og rullemodstand. Ud fra målingerne på de forskellige overflader undersøges korrelationen til rullemodstands for peak fraction og MPD. Fra målingerne kan vi se, at MPD ikke korrelerer med rullemodstanden, hvorimod peak fraction i et omfang kan bruges til at forudsige rullemodstanden.

Vi konkluderer, at denne forenklede eksperimentelle tilgang, under kontrollerbare forhold, kan opnå en god nøjagtighed og repeterbarhed, og er nyttig i arbejdet med at udvikle og validere rullemodstandsmodeller.

# Preface

This thesis describes the work done from January 2019 to December 2021, at IMFUFA at the Department of Science and Environment at Roskilde University (RUC). The project is a continuation of work package 1 (WP1) in the Roads Saving Energy Project (ROSE) 2016-2018, involving Roskilde University, the Danish Road Directorate, and other partners.

The initial idea behind the Ph.D. scholarship was to use the already developed test rig to measure rolling resistance for different wheels and surfaces and to try to validate different models. Unfortunately, further development on the test rig was needed, which, together with some measurements, forms the basis of this thesis. Behind the scenes, there was a huge amount of work in developing the setup and troubleshooting various issues, which has resulted in plenty of scrapped data. It is estimated that less than 30 % of the collected data is presented in this thesis. Personally, this has been the reason for much hair-pulling during the experimental development. Niels Boye Olsen, associate professor emeritus at the institute, has a sad but in our case fitting saying:

*“Proof of concept is easy. But any attempt of improvement is a deterioration”*

However, as Albert Einstein, allegedly, once said:

*“If we knew what it was we were doing, it would not be called research, would it?”*

## Acknowledgements

This work would not have been possible without the people surrounding me for the last three years.

Firstly, I would like to thank my supervisors: Tina Hecksher and Jeppe Dyre. Tina Hecksher, who has been my main supervisor and helped me both in the good times and the bad times, by showing the way through the labyrinth of research. Jeppe Dyre, as my co-supervisor, has helped me in the quest for interesting textures and model testing.

I have had the pleasure of being a part of RUC for ten years, with the last seven as a “IMFUFAner”. To all the people at IMFUFA, I owe you all a lot of gratitude, as you have been like a second family, helping both on a personal and professional level. I would like to thank the whole team in the workshop:

Ebbe, Bjarne, Preben, Torben, Ib, Bo, Thorbjørn, and Oliver, who all have helped in the development of the test rigs.

I would like to give very deep and special thanks to my office mate Marc Dam, who has become a very dear friend to me and has helped me countless times. In our fight against bad data, the bond became strong. Also, no one should underestimate the benefits of having a mathematician as an office mate.

Due to the COVID-19 pandemic, my change of environment was stopped ahead of time, making my visit to IFSTTAR, Nantes, only last 10 days. Still, I would like to thank Julien Cesbron and Fabienne Anfosso-Ledee for a warm welcome to Nantes, and for being part of my Ph.D.

This thesis would not have been possible without some outside help. Financially the research is supported by the VILLUM Foundation's Matter (Grant No. 16515), by Innovation Fund Denmark as a part of the ROSE Project (No. 5160-00009B), and by the Danish Road Directorate. For the experiments, we thank Continental AG for kindly providing the CON wheel and Lykke M. Iversen for visiting us with a profilometer from the Danish Road Directorate.

Last but not least, I thank my supportive family, for continuously showing affectionate support, patience, and care when things got rough and everything else fell apart.

To you, the reader. I am far from the world's greatest writer, but I hope you will enjoy your reading. Good luck!

Morten Lau Larsen

Roskilde, December 31, 2021

# Common Notations and Abbreviations

RR	Rolling Resistance
MPD	Mean Profile Depth
MSD	Mean Segment Depth
Ver1	Test Rig Version 1
Ver2	Test Rig Version 2
CP	Contact Patch
$\mu_{RR}$	Rolling Resistance Coefficient
$F_L$	Load Force
$F_{RR}$	Rolling Resistance Force
$P_f$	Peak Fraction
$\tau$	Torque

# Contents

English Abstract	i
Danish Abstract	ii
Preface	iii
Common Notations and Abbreviations	v
<b>1 Introduction</b>	<b>1</b>
<b>2 Material Properties and Rolling Resistance</b>	<b>3</b>
2.1 Material Mechanics of Solids . . . . .	3
2.2 Forces in Rolling Motion . . . . .	7
2.2.1 Force Calculations . . . . .	9
<b>3 Characterising Surface Texture</b>	<b>11</b>
3.1 MPD in Detail . . . . .	13
3.2 Enveloping . . . . .	14
<b>4 A Toy Model - Stored Energy</b>	<b>17</b>
<b>5 Experimental Drum Setup</b>	<b>19</b>
5.1 Background . . . . .	19
5.2 Test Rig Design . . . . .	21
5.2.1 Rolling Resistance Calculation . . . . .	22
5.2.2 Comparability of Flat and Curved Surfaces . . . . .	23
5.3 Test Rig Construction . . . . .	24
5.3.1 Test Rig Version 1 . . . . .	24
5.3.2 Test Rig Version 2 improvements . . . . .	26
5.3.3 Calibration . . . . .	31
5.3.4 Load-Dependent Bearing Friction . . . . .	32
5.3.5 Measured Load Hysteresis . . . . .	33
5.4 Measuring Protocol . . . . .	34
5.4.1 Test Rig Version 1 . . . . .	34
5.4.2 Test Rig Version 2 Changes . . . . .	36
5.5 Test Wheels . . . . .	38

---

5.6	Surfaces . . . . .	39
5.6.1	Sandpaper . . . . .	39
5.6.2	Geometric Pattern - 3D Print . . . . .	41
5.7	Data Treatment Protocol . . . . .	43
<b>6</b>	<b>Contact Patch Experiments</b>	<b>44</b>
6.1	Contact Patch Measuring . . . . .	44
<b>7</b>	<b>Measurements and Results</b>	<b>47</b>
7.1	Repeatability . . . . .	47
7.2	Load, Speed and Temperature . . . . .	49
7.3	Surface Texture . . . . .	54
7.3.1	Sandpaper . . . . .	55
7.3.2	Geometric Pattern - 3D Print . . . . .	58
7.4	Asymmetry . . . . .	63
7.5	Contribution from Tape and Print - Tex0 . . . . .	64
7.6	Contact Patch Experiment . . . . .	66
<b>8</b>	<b>Summary</b>	<b>70</b>
	<b>Bibliography</b>	<b>73</b>
<b>A</b>	<b>Appendix: Ver2 measurements</b>	<b>79</b>
<b>B</b>	<b>Appendix: Slope Analysis</b>	<b>87</b>
<b>C</b>	<b>Appendix: Articles</b>	<b>89</b>
C.1	Laboratory for Validation of Rolling-Resistance Models . . . . .	89
C.2	Draft: Laboratory for Validation of Rolling Resistance Models. II. Rolling Resistance of Periodic 3D-Printed Surfaces . . . . .	117

# 1 Introduction

As the global climate crisis worsens, there is an increased worldwide focus on decreasing air pollution and reducing greenhouse gas emissions, with carbon dioxide,  $\text{CO}_2$ , being one of the main culprits (EPA, 2021). In 2019 it was estimated that 27 % of the total  $\text{CO}_2$  emission in the European Union (EU) was due to fuel consumption within the transport sector (EEA, 2021). For the United States (US) this number was 24 % in 2019 (EPA, 2021). For both the EU and the US the total amount of  $\text{CO}_2$  emissions have kept increasing from 1990 through 2019. Because of this development, the focus on reducing the fuel consumption in motorised vehicles has intensified (Andersen, 2015).

For a vehicle in motion, a set of resistive forces must be overcome to continue moving. These forces can collectively be called the driving resistance (Sandberg et al., 2011b). The energy to overcome the driving resistance comes from the consumption of fuel, which leads to the emission of  $\text{CO}_2$  and other air pollutants.

As presented by Michelin (2003), the resistive forces in the driving resistance consist of internal frictional, gravitational, inertial, aerodynamic and rolling resistance forces. The internal frictional forces correspond to the mechanical friction in/between the vehicle engine and the drive train, as well as brake drag. Gravitational forces are present when driving uphill or downhill. Inertial forces are the forces which oppose the acceleration or deceleration of a vehicle and aerodynamic forces are the result of a vehicle's movement through the air which depend on the size and shape as well as the speed of the vehicle.

Rolling resistance (RR) forces, which are the focus of this thesis, come from the interaction between the rotating wheel and the road. Depending on the driving style, each force contributes different amounts to the total driving resistance. For typical trips, RR continually varies between 10 % and 70 % of the total driving resistance, but is on average between 20 % and 30 % as seen in Fig. 1.1. By minimising one of the forces in the driving resistance, the energy usage in vehicles can be optimised, leading to lower  $\text{CO}_2$  emissions.

The typical way of defining RR is as the dissipation of energy for a travelled distance, but RR is also sometimes defined as the forces working in the direction opposite the rolling direction. When rolling on a surface, deformation can happen in the surface or in the wheel, where energy can dissipate due to viscoelastic effects (Sandberg et al., 2011b). RR due to energy dissipation in the surface is often referred to as structural RR, and is more relevant for heavier vehicles, because a higher load is required for a significant deformation

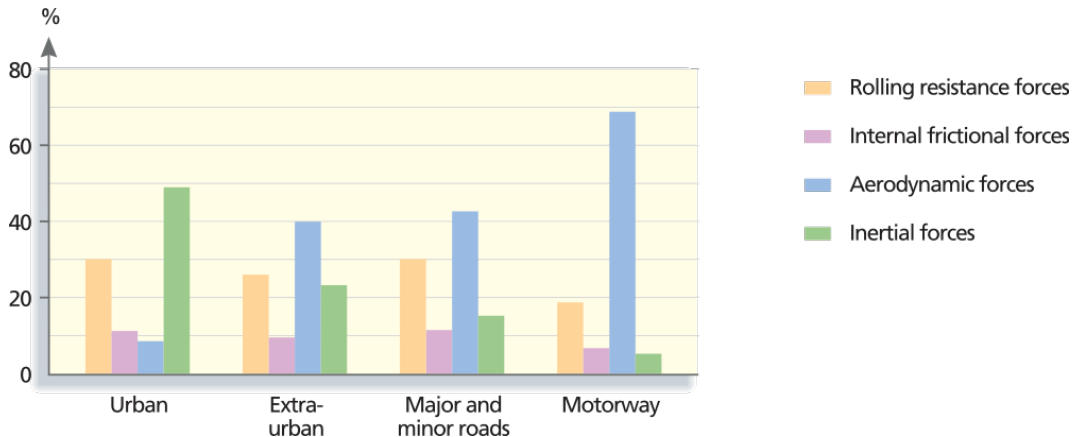


**Figure 1.1:** Forces in percentages of the total driving resistance, for different driving styles. Figure from Michelin (2003).

of a surface. This category is studied in detail by Nielsen et al. (2020). In this thesis, we focus on RR due to the local deformation and energy dissipation in the wheel, which we call “wheel RR” as opposed to structural RR. Together with material properties, wheel RR is introduced in Chap. 2. For simplicity, in the rest of this thesis RR refers to wheel RR.

Much of the current experimental research focuses on in situ experiments (Bergiers et al., 2011), lab experiments using real size car tyres (Ejmsont and Sommer, 2021) or highly detailed finite element models (FEM) when investigating RR (Bazi et al., 2018; Mashadi et al., 2019). Even with the recent progress in the research of RR using real tyres and road pavement, using simple experimental setups for model investigation is still rare.

In this study the primary goal is to develop a small idealised drum test rig capable of testing RR models (Chap. 5). The work in this thesis is an extension of the work done by Hansen and Larsen (2017), where a “version 1” was developed. The development of “version 2” of the test rig forms the foundation for a potential model validation lab for surface textures, and is the main focus in this thesis.

The secondary goal is to test a simple RR model (Chap. 4). This will, in part, be achieved by measuring the RR of small test wheels, solid and pneumatic, on highly controllable surface textures (Chap. 7), using the presented test rigs. It is important to note that direct comparison with measurements using real-world tyres and/or pavement is not of interest, since the goal of the test rig is to test RR models. For model testing, the parameters can be very extreme and idealised, as we will see for the 3D printed surface textures.

## 2 Material Properties and Rolling Resistance

Rolling resistance (RR) is defined by the International Organization for Standardization (ISO) as “Loss of energy (or energy consumed) per unit of distance travelled” (ISO, 2018). Loss of energy is caused by the hysteresis in the viscoelastic material induced by the deflection and deformation during rolling (Sandberg et al., 2011b). Other studies define RR as a combination of aerodynamic drag, hysteresis loss and surface friction (Clark and Dodge, 1979). In this thesis, we use the ISO definition.

To study RR we need to understand how different materials behave under deformation, and how forces affect a rolling object.

### 2.1 Material Mechanics of Solids

In this section, we will go into how solids behave when forces are applied. Before diving into the different classes of solids, it is important to explain the quantities of stress and strain.

Stress,  $\sigma$ , describe the forces acting on a body per unit area.  $\sigma$  is a tensor, which for a cubical element can be written in the matrix form

$$\sigma_{ij} = \begin{pmatrix} \sigma_{11} & \sigma_{12} & \sigma_{13} \\ \sigma_{21} & \sigma_{22} & \sigma_{23} \\ \sigma_{31} & \sigma_{32} & \sigma_{33} \end{pmatrix},$$

where  $\sigma_{ij}$  is the component, parallel to the  $i$ -direction, of the force per unit area acting on a face perpendicular to  $j$  (Ferry, 1980). Stress can be divided into internal and external stress, with forces acting within the material or acting on the surface of the material.

When a material is subjected to external stress it will deform in response. The local deformation is called strain,  $\epsilon$ . Similar to stress, strain can be written in a matrix form:

$$\epsilon_{ij} = \begin{pmatrix} \epsilon_{11} & \epsilon_{12} & \epsilon_{13} \\ \epsilon_{21} & \epsilon_{22} & \epsilon_{23} \\ \epsilon_{31} & \epsilon_{32} & \epsilon_{33} \end{pmatrix}.$$

Depending on how external forces are acting on the material, different terms are used for describing both stress and strain. Figure 2.1 shows five terms often used: Tension, compression, bending, shear and torsion. Tension is the type of stress/strain in which two sections of material on either side of a plane tend to be pulled apart or elongated. Compression is the opposite of tension and involves pressing a material together. Bending involves applying forces in a manner that results in compressing the material on one side and tensioning it on the other. Shear involves applying forces in parallel but opposite directions which causes the material to slide in the direction of the forces. Torsion is caused by forces twisting a material.

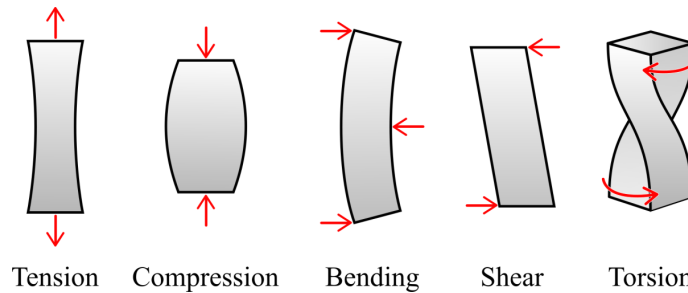


**Figure 2.1:** Types of stress and strain. The red arrows indicate where forces are being applied on the bodies.

A material which regains its original shape after deformation is called elastic. For small stresses, this is the case for most materials, as the materials are kept below the yield strength where plastic (permanent) deformation occurs. For elastic deformation, no energy is dissipated and the work done is zero.

The generalised Hooke's law, which expresses the linear relationship between stress and strain in all directions, is written in the form of a fourth-order tensor

$$\sigma_{ij} = C_{ijkl}\epsilon_{kl}, \quad (2.1)$$

where  $C$  is the modulus of elasticity and consists of 81 entries called elastic constants. This is a big system to keep track of, but by assuming the material is isotropic, i.e. has the same properties in all directions, it is possible to reduce the number of independent constants from 81 to 2. From the knowledge of two elastic moduli, the rest can be calculated, e.g. shear modulus  $G$  for shearing elasticity and the Young's modulus  $E$  for tension and compression elasticity. The reduction of the generalised Hooke's law and the calculation of elastic moduli is not shown here, but we refer to the work of Gould and Feng (2018).

Here we will only consider Young's modulus. If the stress is applied in a uniaxial behaviour, the relationship between stress and strain can be described

by:

$$\sigma = E\epsilon. \quad (2.2)$$

Materials where the stress depends on the strain rate in addition to the strain itself are called viscoelastic. Viscoelastic materials exhibit both elastic and viscous properties. For describing the viscoelastic behaviour, materials are often modelled by the Kelvin-Voigt model or the Maxwell model. These models are also known as Kelvin-Voigt solids and Maxwell fluids (Flügge, 1975). These two types of viscoelastic material can be modelled by a dashpot and a spring, as illustrated in Fig. 2.2.

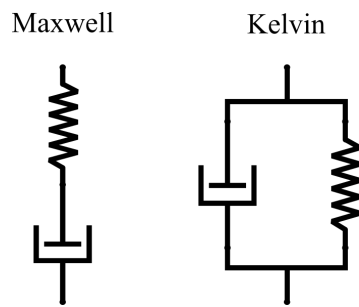


**Figure 2.2:** Illustration of the Maxwell and Kelvin-Voigt models

For a Kelvin-Voigt solid, when constant stress is applied the strain will increase towards a plateau, as seen in Fig. 2.3(a). When the stress is removed, the strain decreases towards zero. The viscous properties, modelled by the dashpot, give the delayed response in strain, while the elastic properties, modelled by the spring, ensure the material will return to its original shape after being deformed. The delayed response to the applied stress causes energy, in the form of heat, to be dissipated during the deformation. This behaviour is known as hysteresis (Vincent, 1982). Figure 2.3(b) shows the relationship between stress and strain for a viscoelastic material undergoing cyclic deformation, where there is a delay between the application (loading) and release (unloading) of stress. The dissipated energy from hysteresis is equal to the area between the loading and unloading curves (Lakes, 2009).

If strain,  $\epsilon$ , is given by a sinusoidal function with angular frequency  $\omega$ , then the relationship between stress,  $\sigma$ , and strain for a linear viscoelastic material is as follows (Nakajima, 2019):

$$\begin{aligned} \epsilon &= \epsilon_0 e^{i\omega t} \\ \sigma &= \sigma_0 e^{i\omega t} e^{i\delta}, \end{aligned} \quad (2.3)$$

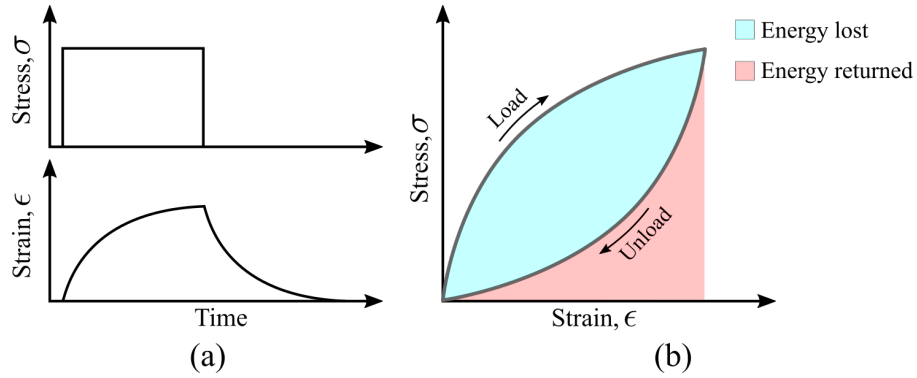


**Figure 2.3:** Viscoelastic material. (a) Stress and strain plots for application (loading) and release (unloading) of constant stress. (b) Stress-strain plot for cyclic deformation.

where  $t$  is the time,  $\delta/\omega$  is the time lag between stress and strain and  $\omega$  is related to the frequency  $f$  by  $\omega = 2\pi f$ . This is illustrated in Fig. 2.4.

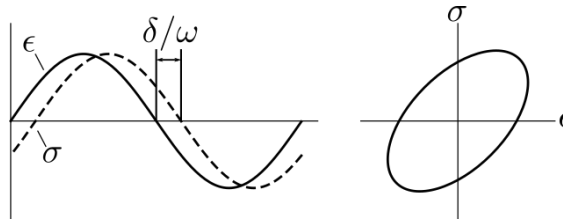


**Figure 2.4:** Sinusoidal strain and stress relation.

The modulus of a material is the relation between strain and stress. Here we write it for the Young's modulus:

$$E^* = \frac{\sigma}{\epsilon} = \frac{\sigma_0}{\epsilon_0} e^{i\delta}, \quad (2.4)$$

where  $E^*$  is the complex elastic modulus. As  $E^*$  is complex, it consists of a real part and a imaginary part. These can be expressed by

$$\begin{aligned} E' &= \text{Re}\{E^*\} = (\sigma_0/\epsilon_0) \cos \delta \\ E'' &= \text{Im}\{E^*\} = (\sigma_0/\epsilon_0) \sin \delta \end{aligned} \quad (2.5)$$

$E'$  is a measure for the stored energy and  $E''$  is a measure for the dissipated energy. The ratio of the two moduli is referred to as the loss tangent,  $\tan \delta = E''/E'$ . For the sinusoidal deformation,  $E'$  is recovered per cycle, while  $E''$  is lost as heat per cycle (Ferry, 1980).

For different temperatures the viscoelastic properties vary. Figure 2.5 shows a typical  $E''$  frequency sweep commonly seen in rheology, illustrating how energy loss changes at different frequencies (Brinson and Brinson, 2015; Michelin, 2003; Nakajima, 2019). From this it is clear that for a given temperature, a peak in energy loss is to be expected. If the temperature is changed, the peak shifts in frequency. For a fixed frequency below the peak, an increase in temperature will result in a decrease in  $E''$ . If the fixed frequency is above the peak an increase in temperature would result in an increase in  $E''$ .

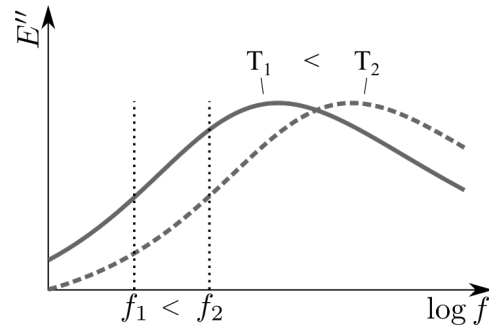


**Figure 2.5:** Illustration of a relation between the loss modulus,  $E''$ , and the strain velocity (frequency) of a viscoelastic material. Also shown is the influence of temperature,  $T$ , on the frequency dependence of  $E''$ .

Depending on the location compared to the peak, the energy loss is expected to increase or decrease for changes in temperature and frequency.

As we will see in the following section and Chap. 7, the dependence of  $E''$  on temperature, strain velocity (frequency) and strain amplitude all play a key role in the study of RR due to the fact that energy loss in a wheel causes RR.

## 2.2 Forces in Rolling Motion

For a wheel to stop its rolling motion, a resistive force needs to be present. From this point of view, RR is often seen as a force opposing the rolling motion. In this section, we will look at the forces acting on a rolling wheel in a steady-state, i.e. no acceleration.

If a wheel is subject to an external load,  $F_L$ , on an incompressible surface, the wheel will deform creating a contact area. This contact area between the wheel and the surface is called the contact patch. For a stationary wheel, the resultant forces from the surface on the contact patch are symmetric around the wheel centre as shown in Fig. 2.6(a) and balance out  $F_L$ . In the case of rolling motion the forces on the contact patch change. As material moves

under the centre of rotation, the material compresses as it enters the contact patch and relaxes as it leaves. Because of the viscoelastic properties of the material, the resultant vertical forces from the surface are offset towards the front of the contact patch as shown in Fig. 2.6(b), instead of being symmetric around the wheel centre. The offset,  $\delta$ , of the resultant vertical force,  $F_Z$ , affects the wheel with a torque,  $\tau_Z$ , opposite the rotation.

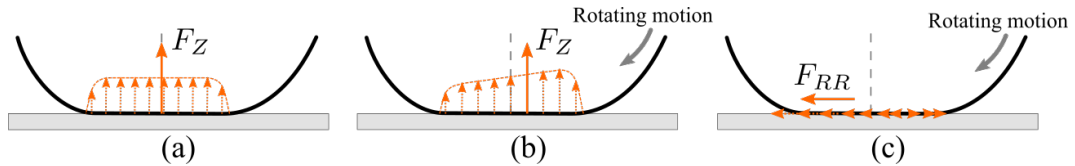


**Figure 2.6:** Forces from the contact patch acting on a wheel. (a) Vertical forces on a stationary wheel, (b) Vertical forces on a rolling wheel, (c) Horizontal forces on a rolling wheel. Adapted from Michelin (2003).

On the contact patch, horizontal forces will affect the wheel due to shearing in the material (Michelin, 2003), as shown in Fig. 2.6(c). The resultant horizontal force is called the RR force,  $F_{RR}$ , and opposes the motion of the wheel.  $F_{RR}$  gives rise to a torque,  $\tau_{RR}$ , around the centre of the wheel in the direction of rotation.

For a wheel to roll in a steady-state, the sum of the torques and forces must both be equal to zero. This is only true if a driving force,  $F_{drive}$ , is affecting the wheel opposite to  $F_{RR}$ . In Fig. 2.7 the balancing forces and torques are shown for a rolling wheel.

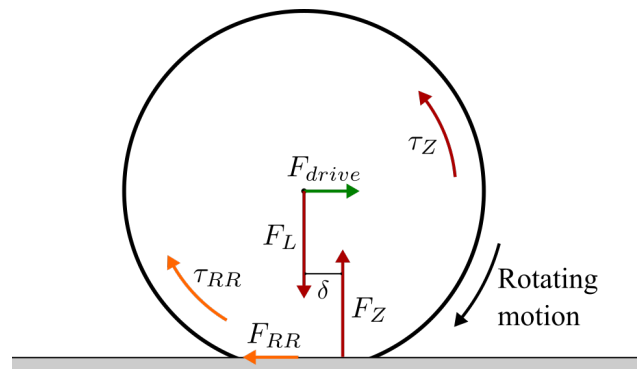


**Figure 2.7:** Illustration showing the balancing forces for a rolling wheel. Shown is: Driving force,  $F_{drive}$ ; load,  $F_L$ ; rolling resistance force,  $F_{RR}$  and corresponding torque,  $\tau_{RR}$ ; vertical resultant force from the contact patch,  $F_Z$  and corresponding torque,  $\tau_Z$ ; offset of the vertical forces due to viscoelastic properties,  $\delta$ .

It turns out that there is a near-linear relationship between RR and load (Sandberg et al., 2011b). To allow comparison between different tyres, we introduce the RR coefficient. The standard notation of RR coefficient is  $C_r$  (ISO, 2018). However, due to the resemblance to the friction coefficient, we denote the RR coefficient as  $\mu_{RR}$ . Thus we write

$$F_{RR} = \mu_{RR} F_L. \quad (2.6)$$

### 2.2.1 Force Calculations

In the following, forces for steady-state rolling motions are calculated in two dimensions, with the frame of reference following the surface.

For a wheel we can calculate the forces acting on it, by studying the system in two dimensions, as shown in Fig. 2.8(a).

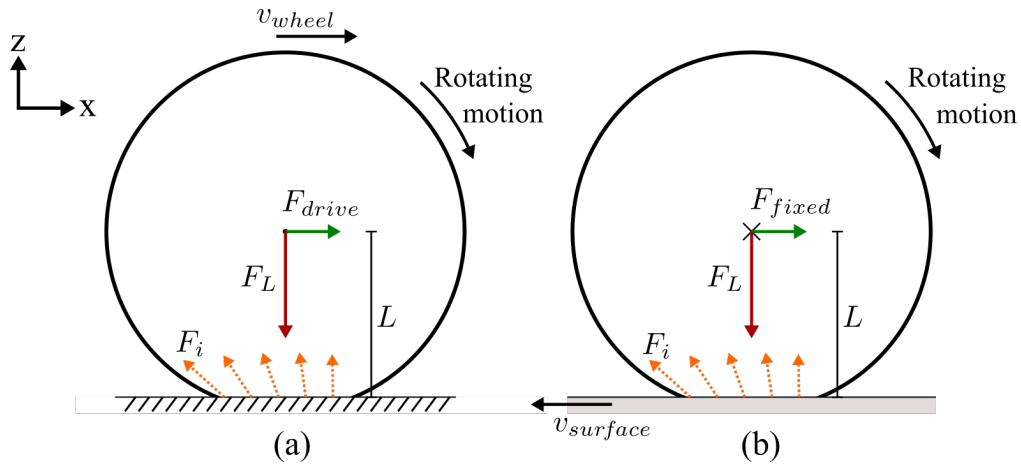


**Figure 2.8:** Force diagram showing a rolling wheel in a steady state with surface as frame of reference (a) and wheel centre as frame of reference (b). Shown is speed,  $v$ ; Load,  $F_L$ ; driving force,  $F_{drive}$ ; fixating force,  $F_{fixed}$ ; resultant forces from the contact patch,  $F_i$  and the distance from the surface to the wheel centre,  $L$ .

If  $x_i$  is a position where the wheel is in contact with the surface, the contact patch can be expressed by  $\sum_i x_i$ .

For a wheel rolling on a flat surface the total vertical force,  $F_{tot}^z$ , must be zero, since there is no movement in the vertical direction. Thus, the load,  $F_L$ , must be balanced with the vertical forces on the contact patch,  $F_i^z$ ,

$$\sum_i F_i^z = -F_L, \quad (2.7)$$

If the wheel is in a steady-state, the same must apply to the total horizontal forces,  $F_{tot}^x$ , since there is no acceleration. Therefore,

$$F_{drive} = - \sum_i F_i^x, \quad (2.8)$$

where  $F_i^x$  are the horizontal forces on the contact patch and  $F_{drive}$  is the force needed to maintain a steady motion. As mentioned previously the horizontal resultant force,  $F_{tot}^x$ , is called the rolling resistance force,

$$F_{tot}^x = \sum_i F_i^x = F_{RR}. \quad (2.9)$$

The resultant forces on the contact patch can be written as  $\bar{F}_i = (F_i^x, 0, F_i^z)$ , while the position vector from the wheel centre to the contact patch can be written as  $\bar{r} = (x_i, 0, L)$ , where  $L$  is the distance from the contact patch to the wheel centre.

Hence, the total torque,  $\bar{\tau}_{tot}$ , on the wheel centre can be expressed by

$$\bar{\tau}_{tot} = \bar{F}_i \times \bar{r} = (0, LF_i^x - x_i F_i^z, 0). \quad (2.10)$$

Since  $\bar{\tau}_{tot} = \bar{0}$  in a steady-state the following must be true

$$LF_i^x = x_i F_i^z. \quad (2.11)$$

For the steady-state, all work on the rolling wheel is done by  $F_{drive}$ , while the material on the wheel is static when affected by  $F_i$ . The energy loss over time is

$$P_{loss} = vF_{drive} = vF_{RR}. \quad (2.12)$$

If the reference frame follows the wheel the surface will be in motion, as shown in Figure 2.8(b). In this system, the forces would be the same. However, the driving force,  $F_{drive}$ , on the wheel is changed with  $F_{fixed}$  fixating the wheel. Because the centre does not move,  $F_{fixed}$  is not doing any work. The work on the wheel is instead done by  $F_i$ . This is the situation for the drum test rig presented in Chap. 5, where  $F_{tot}^x = F_{RR}$  is measured by the reacting force on the surface.

### 3 Characterising Surface Texture

The best way to describe a surface texture is to have a full 3-dimensional plot of it, showing all shapes and sizes. However, comparing textures using 3-dimensional plots is difficult. By having a simple measure for complex surface textures, we can easily quantify and compare them. Unfortunately, the usage of simple measures comes with some limitations, such as loss of information. Two very different textures may have the same measure. Thus, it is important to evaluate if a measure has the desired properties.

In this section, we will present different measures used for surface textures in the research of RR. The term “surface texture measure” will be used interchangeably with “surface texture parameter”, and “surface texture” will be omitted if it is obvious from the context.

Surface textures are often classified into four groups by size: Unevenness, megatexture, macrotexture and microtexture. The texture sizes are divided by wavelength,  $\lambda$ , and peak-to-peak amplitude,  $A$ , as follows (Sandberg et al., 2011a; Hall et al., 2009):

- Unevenness:  $\lambda = 0.5$  to 50 m
- Megatexture:  $\lambda = 50$  to 500 mm,  $A = 0.1$  to 50 mm
- Macrotexture:  $\lambda = 0.5$  to 50 mm,  $A = 0.1$  to 20 mm
- Microtexture:  $\lambda < 0.5$  mm,  $A = 1$  to 500  $\mu\text{m}$

In studies of RR between vehicle tyres and pavement textures, microtextures are not found to have a significant effect on RR (Andersen, 2015). Due to the size of the test rigs and the chosen textures, as presented in Chap. 5, only macro- and microtextures are studied in this thesis.

Historically, different measures have been developed and used to quantify surface texture when studying RR. In the following, some of the most common measures are presented.

**International Roughness Index (IRI)** is the most commonly used measure worldwide for evaluating and managing road systems (Sandberg et al., 2011a). It is based on the quarter-car model (Sayers, 1989), i.e. a mathematical model of a single wheel and suspension system. The commonly used units are metres per kilometre (m/km) and millimetres per metre (mm/m).

**Root Mean Square (RMS)** measures the variability of a profile, and is defined as

$$\text{RMS} = \sqrt{\frac{1}{L} \int_0^L y^2(s) ds}$$

where  $L$  is the total length of the profile,  $y(s)$  is the height of the profile at a specific position  $s$ .

**Skewness (SKEW)** is a measure of asymmetry of the amplitude distribution (see Fig. 3.1). The measure indicates whether the profile curve exhibits a majority of peaks directed upward (positive skew) or downward (negative skew). The calculation of SKEW is specified and standardised by ISO (1997, 2019):

$$\text{SKEW} = \frac{1}{\text{RMS}^3} \left( \frac{1}{L} \int_0^L y^3(s) ds \right)$$

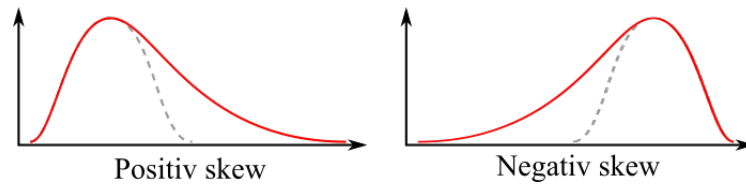


**Figure 3.1:** Illustration of different skewnesses.

**Mean Texture Depth (MTD)** is also called the “volumetric patch method” and was previously known as the “sand patch method”. It has been used since the mid 1900s and is measured by pouring a pile of sand (or glass beads) of a known volume onto the surface. The sand is spread evenly into a circle, levelled with the top peaks of the surface. The measure is then calculated by

$$\text{MTD} = \frac{4V}{\pi D^2}, \quad (3.1)$$

where  $V$  is the volume of sand and  $D$  is the diameter of the resulting circle.

**Mean profile depth (MPD)** is, alongside IRI, one of the most commonly used measures for surface texture on pavement and is the standard measure used for quantifying macrotextures. MPD was created to correlate with volumetric methods, e.g. the sand patch test, and be calculated

from surface profiles. The calculation procedure is specified and standardised by ISO (1997, 2019), and is described in further detail later. No theoretical or intuitive basis has been found for this method, except that it should correlate with MTD (Bergiers et al., 2011; Anfosso-Lédée et al., 2016).

**Texture Penetration Area (TPA)** is a relatively new measure to better reflect the contact area between road and tyre, introduced by Andersen (2015). TPA is based on the energy dissipation in a wheel when exerted to deformation by the texture. The measure achieves this by including the enveloping of the tyre. Andersen showed that for predicting the RR coefficient, TPA outperforms MPD for the majority of combinations of tyre type, aggregation length and enveloping function. Enveloping is discussed later.

In this study, we will be using MPD as the main texture measure as it is the standard measure for quantifying the macrotexture, and has been known to have a small correlate with RR (Sandberg et al., 2011a; Sohaney and Rasmussen, 2013; Goubert et al., 2014; Ejsmont et al., 2017). We acknowledge that other measures can be used, and in some cases are more descriptive (e.g. IRI is used for studying energy dissipation in dampers).

### 3.1 MPD in Detail

With the arrival of laser profilers, it has become possible to measure highly detailed surface profiles at driving speeds. The volumetric measure MTD has little relation to surface profiles and therefore a new measure was sought. As a large amount of research using MTD already exists, a new measure would ideally correlate with MTD. In the 1980s and 1990s the new measure Mean Profile Depth (MPD), standardised in ISO (2019), was developed to be calculated only from profile measurements (Sandberg et al., 2011a, 2018), making it easy and quick to calculate from the 2D laser measurements. As MTD and MPD correlate well, the measure Estimated Texture Depth (ETD) is sometimes used as an estimate of MTD based on MPD. The conversion from MPD to ETD is (ISO, 2019):

$$\text{ETD} = 1.1 \text{ MPD}$$

The procedure for calculating MPD, as presented in ISO (2019), can be summarised in the follow steps:

1. Use profile data for at least 1 m with the minimum resolution: Longitudinal  $\leq 1$  mm, vertical  $\leq 0.05$  mm.

2. Correct invalid, i.e. missing and spurious, data points by interpolation.
3. Apply a 2nd order Butterworth filter to the profile in forwards and backwards direction: High-pass with cutoff at wavelength 174.2 mm and low-pass with cutoff at wavelength 2.4 mm.
4. Divide the profile into 100 mm segments.
5. Divide the segments into two subsegments of 50 mm and find the peak height of each subsegment.
6. Determine the Mean Segment Depth (MSD) as seen in Fig. 3.2.
7. Repeat step 4-6 for each 100 mm segment.
8. Average the MSD, optionally removing extreme outliers, of at least 10 segments to calculate the MPD value.

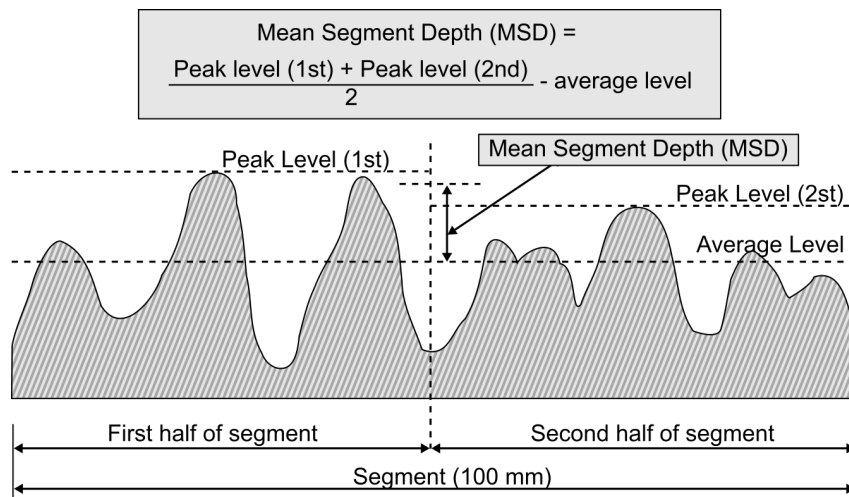


**Figure 3.2:** Illustration of the MSD calculation procedure. The illustration is a modification from Sandberg et al. (2011a).

As research in the influence of texture on RR grows, the need for a precise measure grows as well. With the understanding of enveloping, Sandberg et al. (2018) recommend an improvement of MPD using enveloped profiles, while Andersen (2015) has developed TPA as a new texture measure for road macrotexture.

## 3.2 Enveloping

Before going further we need to introduce the “envelope” of a profile, which is becoming more used as seen in the study by Sandberg et al. (2018) and the calculation of TPA by Andersen (2015). Compared to IRI and MPD, the

envelope is not directly a surface texture parameter, but a correction for how only part of a tyre is in contact with a surface (Goubert and Sandberg, 2018).

When a tyre rolls on a textured surface, it is pushed down into the surface by its weight, and the peaks/spikes of the surface are indented into the tyre. However, because of the viscoelastic properties of the tyre, the tyre might not come into full contact with the surface, since the surface usually has valleys/grooves as presented in Fig. 3.3. The pseudo-profile, which simulates the contact line between tyre/surface and tyre/air over the valleys, is called the enveloped profile. Since the 1990s, it has been known that enveloping plays an important role in noise generation (Andersen, 2015), and because enveloping is related to how a tyre deforms, it also plays an important role in the generation of RR. Depending on the specific method used, different tyre properties, e.g. Young's modulus or the Poisson ratio, may be needed when determining how a tyre is enveloping a surface texture.

In this thesis, enveloped profiles or measures calculated from enveloped profiles are not used for analysing surface textures. This choice is made for the following reasons: 1. MPD is a well-established surface measure which only depends on the texture, whereas enveloping includes additional parameters specific to the different wheels and is yet to be used widely, and 2. To develop and test RR models on a newly developed test rig, the implementation of a new enveloped measure is not in focus and is a study on its own.

As presented by Goubert and Sandberg (2018), the most commonly used methods, for finding the enveloped profile, are:

- A mathematical/empirical method proposed by von Meier et al. (1992)
- A tyre-physics-based method originally proposed by Clapp et al. (1988)
- A tyre-physics-based method improved by Fong (1998)
- A tyre-physics-based method improved by Klein and Hamet (2004)
- The indenter method proposed by Gottaut and Goubert (2016)

In the study by Goubert and Sandberg (2018), the enveloped profile was measured for a car tyre using a simple triangular surface texture with a compressible plasticise in the gaps. While the measurements of the profile show that the used algorithm is only an estimate for the actual enveloped profile, especially for the mathematical/empirical method, they conclude that applying enveloping using the indenter method can improve the correlation of the RR coefficient with the MPD measure.

The procedure for the indenter method is illustrated in Fig. 3.3 and can be summarised as follows for a texture profile,  $\bar{y}[\bar{x}] = (y_1(x_1), \dots, y_N(x_N))$ :

1. Divide the profile into segments representing the length of the tyre contact patch, e.g. 90 mm.

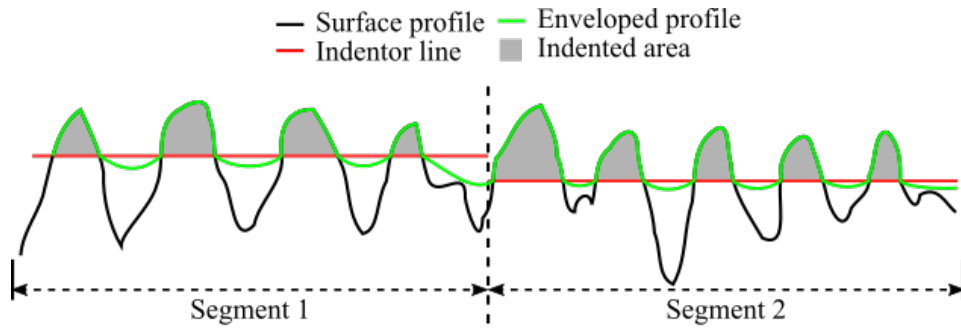


**Figure 3.3:** Illustration of the envelope procedure as described by Gottaut and Goubert (2016).

2. To remove slope in the first segment, calculate a regression line and subtract it from the profile in the specific segment.
3. Place a horizontal indenter line at the maximum profile height  $y_{i,max} - k$ , initially with  $k = 0$  in the segment.
4. The area,  $A$ , under the profile and over the horizontal line, is calculated and compared to a predefined value  $S$ . If  $S < A$ ,  $k$  is increased by a specific step size, e.g. 0.01 mm, and the process is repeated from step 3.
5. If  $S \geq A$ , the points above the horizontal line are stored as  $(x_{i,env}, y_{i,env})$
6. Repeat steps 2–5 for all segments.
7. To obtain the full enveloped profile, the data points not stored are updated using interpolation between the nearest stored points.

As discussed by Goubert and Sandberg (2018) the interpolation method should be chosen carefully. While the measured enveloped profile in the study indicates that a cubic spline interpolation may be a good choice, a simple linear interpolation shows good results with fewer problems at small  $S$ -values. No standardisation has been done on this procedure and the measures involved.

It is worth noting that when comparing the procedure for calculating the enveloped profile using the indenter method proposed by Gottaut and Goubert (2016), the process of increasing the indentation until a specific value has been reached is similar to the enveloping method and TPA method as described by Andersen (2015). The work by Ejsmont and Sommer (2021) also shows a similar idea for descriptive measures used in researching RR.

## 4 A Toy Model - Stored Energy

In this chapter, a new toy model is presented. The same model is presented in the “work in progress”-paper, included as Appendix C.2. The toy model is based on using stored energy to predict RR due to local deformation from textures for a given load, speed and wheel material. The model is highly idealised as it is based on comparing surfaces consisting of identical cuboids on a regular square array (see Sec. 5.6.2).

In Sec. 2.1 solid materials are described as having elastic properties, modelled by a spring capable of storing and releasing energy. In the case of a perfect spring, the energy is  $k(\Delta x)^2/2$ , where  $k$  is the spring constant and  $\Delta x$  is the change, from equilibrium length, in the length of the spring. If a material is modelled by multiple springs as seen in Fig. 4.1, the total energy stored in the springs carrying a given load depends on the number of springs. For  $N$  springs the total energy is

$$E_{tot} = \frac{1}{2}Nk(\Delta x)^2.$$

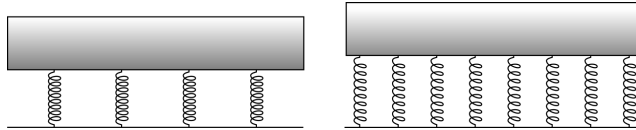


**Figure 4.1:** Illustration of a simple spring model. Assuming the same load, each spring to the left stores four times as much energy as each spring to the right.

For  $N$  springs the total force is  $Nk\Delta x$ , implying  $\Delta x \propto 1/N$  for a given load. When this is substituted into the energy expression, we see that for a given load the total energy stored in the springs, is inversely proportional to  $N$ ,

$$E_{tot} \propto 1/N. \quad (4.1)$$

Thus, as the number of springs is increased, the total stored energy decreases. In the situation shown in Fig. 4.1, the case with twice as many springs stores half as much energy.

Now consider a material that does not behave like a perfect spring and has energy loss due to hysteresis. As a wheel made of this material rolls

over a surface with discrete peaks of equal size, for a given speed, the wheel deformation takes place on a distinctive time scale. This time scale corresponds to a well-defined frequency range and determines the material's loss and storage moduli. Just as in the case of the perfect spring, where the storage modulus controls the spring deformation, in this case, the loss modulus also controls the spring deformation. Hence the inverse proportionality of Eq. (4.1) applies to energy loss as well.

The toy model thus predicts that for a given load, speed and wheel material, RR is inversely proportional to the number of springs involved. For the surface texture of Fig. 5.14 the number of springs is proportional to the peak fraction<sup>1</sup>,  $P_f$ . This is because, for geometric reasons, the total area of the wheel, which at any given time is close to the surface, is independent of  $P_f$ . Thus the toy model predicts that RR is inversely proportional to  $P_f$ .

We note that the wheel deformation not only consists of the highly localised deformations deriving from each peak being pressed into the wheel. There is also a “global” wheel deformation, the magnitude of which depends on the load but not the nature of the surface. This global deformation also results in an energy loss, but it is to a good approximation independent of  $P_f$ , because it is controlled by the frequency-dependence of the elastic modulus at the wheel rotation frequency. This frequency-dependence is incidentally much smaller than that controlling the peak-derived losses associated with indentations.

The toy model assumes that the total RR is a sum of the “local” and the “global” losses. This leads to the following expression for how the RR coefficient,  $\mu_{RR}$ , depends on the peak fraction for a given load, speed and wheel material:

$$\mu_{RR} = C_0 + C_1/P_f. \quad (4.2)$$

For a given wheel, the two constants,  $C_0$  and  $C_1$ , in general, depend on the temperature, the load and the speed. For the case of a surface having no texture ( $P_f = 1$ ) the RR coefficient in the model due to global loss is

$$\mu_{RR}^{\text{global}} = C_0 + C_1. \quad (4.3)$$

Hence, by subtracting  $\mu_{RR}^{\text{global}}$  from the total RR coefficient, the model expresses the contribution from local loss, i.e. contribution from texture,

$$\mu_{RR}^{\text{local}} = \mu_{RR} - \mu_{RR}^{\text{global}} = C_1 (1/P_f - 1). \quad (4.4)$$

This expression is tested in Sec. 7.3.2, where the results are consistent with Eq. (4.2) and thus the toy model.

---

<sup>1</sup>Peak fraction is the fraction of the contact patch which is peaks.

## 5 Experimental Drum Setup

In this chapter, we present the experimental test rigs used for measuring rolling resistance (RR). The test rigs have been the main workhorses of this study, and have been through extensive development and troubleshooting. First, we briefly review previous experiments in the field of RR, where the drum method is one out of many. The setup is then introduced as a general design, followed by a detailed description of the construction of the two test rigs. Notice we use the noun test rig for the specific, and setup for test rigs of similar design. From the knowledge of how the test rigs are constructed, we present the different experimental protocols used. Finally, we present the different wheels and surfaces used and the data treatment protocol.

### 5.1 Background

Measuring RR is a difficult task and requires the use of rather advanced equipment and methodology. For a passenger car at a load of approx. 3.5 kN (gross vehicle weight of 1400 kg distributed evenly onto four wheels), RR is in the range of 30 N – 40 N, or about two orders of magnitude smaller than the load (Zöller, 2014).

Since the beginning of the twentieth century, several methods have been used to measure vehicle/tyre RR (Andersen, 2015). They can be divided into two overall categories: “in situ” methods and laboratory methods. In situ is Latin and translates directly to “on-site” or “in position”. There are pros and cons to each method. Where the in situ methods measure directly on the systems we want to study, the uncontrollable parameters are usually many, while the laboratory methods are more controllable but also much more idealised, making the results less connected to the real world. Depending on the purpose of a study, the choice of method may differ.

Back in 2011, Sandberg et al. (2011b) classified methods for measuring RR into the following categories:

**Fuel consumption** is measuring the total fuel consumed by the engine for a vehicle to maintain a certain speed and has been used in many different ways. An example is the study by Sandberg (1990), where frequent measurements of engine inflow were used to see if a correlation exists between fuel consumption and the road surface. Compared to other methods

fuel consumption directly measures the used energy, which depends on all the resistive forces in driving resistance, including the internal forces from friction in the engine as well as the energy consumption of auxiliary equipment, e.g. light, radio and heater.

**Coast down** lets a vehicle coast freely from an initial speed and position. The engine and gear train are disengaged by putting the vehicle in neutral, making the driving force independent of the internal forces in the transmission and the engine. According to Sandberg et al. (2011b) this method has been used since the 1920s, and is still a common method for measuring RR. For instance, in the work by Karlsson et al. (2011) coast down methods are used on a private car and on a heavy goods vehicle to estimate how macrotexture and unevenness affect RR, while also comparing to the trailer and drum methods.

**Trailer** is measuring the force opposing the motion of the wheel. While the principle is the same, different technologies are used for constructing trailers capable of measuring RR (Zöller, 2014). This method is more idealised since it removes forces unrelated to the tyre-pavement interaction, e.g. drag and internal friction. This is a newer method for measuring RR, known since the 1980s (Sandberg et al., 2011b), and is today a very common method (Sandberg et al., 2011a; Vieira et al., 2019). Should the total driving resistance, excluding resistance from the engine and transmission, be of interest, one could simply tow a car in neutral<sup>1</sup> as seen in the work by Synak and Kalasova (2020).

**Drum** moves the measurements from the pavement into the laboratory by driving a single wheel internally or externally on a drum, i.e. internal or external drums, with an applied load. The RR will resist the rotation of the drum and can be measured in several ways, e.g. drum torque input, drum deceleration or motor power consumption. External drums have been used (at least) since 1922 (Holt and Wormeley, 1922), and are commonly used by tyre manufactures for testing tyres, from which several standardisations have been made (ISO, 2005, 2018; ASTM E1845 - 09, 2009). For research purposes, the drum method often deviates from the standards as different physical properties are investigated. This is clear from the smaller drum method presented by Pexa et al. (2020) using two external drums, and the large internal drum at Federal Highway Research Institute (BASt) with an inner diameter of 5.5 m, where large realistic road surface replicas can be mounted (Sandberg et al., 2011b, pp.

---

<sup>1</sup>This is technically still a trailer

51). Compared to the previous methods the drum method is the most idealised as almost all disturbances from the outdoors and the vehicle have been removed, e.g. temperature and wind. Unfortunately, the use of a drum introduces curvature. This causes the interaction between surface and wheel to differ compared to flat pavement. The implications of using curved surfaces are presented in Sec. 5.2.2.

As the research in RR expands, so does the methods used to investigate it. New methods like the one presented by Ejsmont and Owczarzak (2019) adds to the research on RR. This method is based on measuring the energy loss of a bouncing (oscillating) tyre on a pavement sample. Due to the method being a stationary test the RR is not measured directly but estimated.

Methods using cylindrical wheels in a circular motion have also been used (Heinz and Grosch, 2007; Araújo et al., 2019). However, these methods give rise to an undesirable skidding when purely measuring RR, which is alleviated by using a conical wheel.

By having conical wheels roll in a circular motion on a disc, the equipment can measure the resistive forces (Riahi et al., 2020). This laboratory method makes it easier to obtain highly controllable measurements on small pavement samples. For lack of a better name, we will call this the “Conical wheel method”.

## 5.2 Test Rig Design

The test rigs used in this study are small-scaled internal drums capable of measuring RR with high controllability of load, rotation velocity and ambient temperature while keeping running costs to a minimum. Unique for the test rigs are the small surface drum for internal measuring. The internal drum makes it easy to fit and attach textures, as the centrifugal forces when the drum rotates helps keeping the texture in place. The size of the drum excludes the possibility of using real car or truck tyres but is acceptable since the goal of the setup is surface model validation where the use of real tyres is not necessary. By using small solid rubber wheels on simple surfaces the method becomes even more idealised compared to the usage of pneumatic tyres. Of the previously mentioned method and studies, only the conical wheel method presented by Riahi et al. (2020) uses solid wheels to measure RR, while the rest of the methods mainly uses pneumatic wheels, i.e. car tyres.

For the test rig the resisting forces opposing rotation correspondence to bearing friction, wind resistance and RR. By measuring the amount of torque a motor is applying to maintain a constant angular velocity, the RR can be calculated.

### 5.2.1 Rolling Resistance Calculation

This section is rewritten from the work Larsen et al. (2021).

For the wheel inside the test rig, when angular velocity is constant no angular acceleration is present, implying the vector sum  $\sum \vec{\tau} = \vec{0}$ , where  $\tau$  is torque. The sum of torques around the centre of the wheel can be expressed by

$$\vec{\tau}_{\text{wheel}}^{\text{O}} = \vec{\tau}_{\text{RR}} + \vec{r} \times \vec{F}_{\text{drum} \rightarrow \text{wheel}} + \vec{\tau}_{\text{loss}}^{\text{wheel}} = \vec{0} \quad (5.1)$$

where  $\vec{\tau}_{\text{RR}}$  is the RR torque,  $\vec{r} \times \vec{F}_{\text{drum} \rightarrow \text{wheel}}$  is the torque deriving from the drum driving the rotation of the wheel, and  $\vec{\tau}_{\text{loss}}^{\text{wheel}}$  is the torque coming from friction in the wheel bearing and air resistance (see Fig. 5.1).

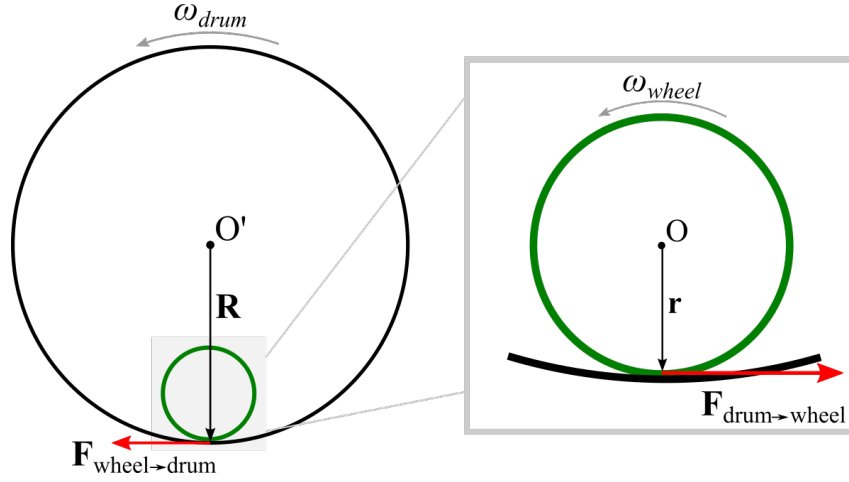


**Figure 5.1:** Diagram showing the drum and wheel for the internal drum setup, and force around the centres respectively (Larsen et al., 2021).

The sum of torques around the centre of the drum can be expressed similarly by

$$\vec{\tau}_{\text{drum}}^{\text{O}'} = \vec{\tau}_{\text{motor}} + \vec{R} \times \vec{F}_{\text{wheel} \rightarrow \text{drum}} + \vec{\tau}_{\text{loss}}^{\text{drum}} = \vec{0}, \quad (5.2)$$

where  $\vec{\tau}_{\text{motor}}$  is the torque delivered by the motor,  $\vec{R} \times \vec{F}_{\text{wheel} \rightarrow \text{drum}}$  is the torque opposing the rotation coming from the wheel, and  $\vec{\tau}_{\text{loss}}^{\text{drum}}$  signifies the total torque due friction, drag, etc., on the drum.

Due to the principle of action and reaction (Newton's third law),  $\vec{F}_{\text{wheel} \rightarrow \text{drum}} = -\vec{F}_{\text{drum} \rightarrow \text{wheel}}$ . Thus for the  $z$ -components, we obtain

$$F_{\text{wheel} \rightarrow \text{drum}} = \frac{1}{r} (\tau_{\text{RR}} + \tau_{\text{loss}}^{\text{wheel}}) = \frac{1}{R} (\tau_{\text{motor}} - \tau_{\text{loss}}^{\text{drum}}) \quad (5.3)$$

which gives the following

$$\tau_{\text{motor}} = \tau_{\text{loss}}^{\text{drum}} + \frac{R}{r} (\tau_{\text{RR}} + \tau_{\text{loss}}^{\text{wheel}}). \quad (5.4)$$

From “skim test reading” (ISO, 2005) we can determine the two loss terms, i.e., the “parasitic losses”. Skim test reading is a measurement where the wheel is only just in contact with the drum surface and rotates without skidding and deformation. At this measurement  $\tau_{RR} = 0$ , due to no deformation, making it possible to express

$$\tau_{\text{motor}}^{\text{skim test}} = \tau_{\text{loss}}^{\text{drum}} + \frac{R}{r} \tau_{\text{loss}}^{\text{wheel}}. \quad (5.5)$$

Consequently, the RR force,  $F_{RR}$ , can be found by subtracting the skim test reading from the measurement with load as follows

$$F_{RR} = \frac{\tau_{RR}}{r} = \frac{1}{R} \left( \tau_{\text{motor}} - \tau_{\text{motor}}^{\text{skim test}} \right), \quad (5.6)$$

where  $\tau_{\text{motor}}$  is the measured quantity, both in the skim test reading and with load applied to the wheel. This procedure assumes that the loss in the various bearings in the setup is load-independent, which is as a good approximation as seen in Sec. 5.3.

### 5.2.2 Comparability of Flat and Curved Surfaces

While a drum is an easy method for measuring RR in controllable environments, the drum introduces a surface with curvature: Convex for an external drum and concave for an internal drum. Due to the curvature, the interaction between the wheel and surface of a drum differs from that of a flat surface. Because of this, the contact area is either larger or smaller compared to a flat surface.

In 1976 the following formula was developed by Clark (1976), showing the relationship between the RR on a flat surface,  $F_{RR,\text{flat}}$ , and the RR on a drum,  $F_{RR,\text{drum}}$ :

$$F_{RR,\text{drum}} = F_{RR,\text{flat}} \sqrt{1 + \frac{r}{R}}, \quad (5.7)$$

where  $r$  is the wheel radius and  $R$  is the drum radius. For an internal drum, we have  $R < 0$ . The formula was later verified in Luchini (1982), where they investigated a method for converting truck tyre measurements on an external drum to the equivalent on a flat surface.

For the work in this thesis, the absolute values of the RR are of lesser importance, as the goal of the test rig is to test and validate RR models. Because the conversion from curved surfaces to flat surfaces is a proportionality constant only depending on the wheel and drum size, the conversion is less important for model testing, as results from drum measurements are directly

translatable to flat surfaces. Hence, throughout this thesis, RR measurements are simply noted as  $F_{RR}$  and  $\mu_{RR}$ , neglecting the drum subscript in  $F_{RR,drum}$  and  $\mu_{RR,drum}$ .

## 5.3 Test Rig Construction

Until now we have discussed the overall design and properties of an internal drum. In this section we present the technical information for the two test rigs used in the thesis, followed by the calibration procedure. Presented is also the information about the bearing load dependence and potentiometer hysteresis.

The test rigs used in the study is of similar internal drums design, referred to as “version 1” and “version 2”. For simplicity, test rig version 1 and version 2 will in the remaining be noted, respectively, as Ver1 and Ver2. The test rigs are developed as a part of the research project ROSE carried out in the period 2016–2018 involving Roskilde University, the Danish Road Directorate, and other partners (Pettinari et al., 2017).

Ver1 was developed and tested prior in the master thesis by Hansen and Larsen (2017), where improvements were deemed necessary due to design and construction issues.

### 5.3.1 Test Rig Version 1

Figure 5.2 shows a photo and a schematic illustration of test rig version 1 (Ver1). The test rig consists of three main sections: Drum, wheel section, motor section.

The drum is a steel cylinder with an inner diameter of 538 mm, and is attached to a 30 mm iron shaft. The drum and axle are supported by two bearing stands (SKF SE 509) on each side, containing a heavy-duty bearing (SKF 1209 EKTN9), allowing the drum to rotate with low resistance. Connected to one end of the shaft is a tachometer (see Fig. 5.3) constructed of a light sensor and a disc with a pattern of 200 radial lines.

The wheel section consists of an interchangeable wheel with modified bearings (SKF 6304) connected to a pivoting arm attached via a 110 mm iron shaft. Modification of the bearings consists of removing the shielding and changing the pre-applied lubrication with low viscosity lubrication. This was done due to extensive heating for longer measurements, using the pre-applied lubrication. A pivoting arm of length 375 mm is connected to an actuator through a spring. By moving the actuator, the spring tension is either increases or decreases, thus increasing or decreasing the load between drum and wheel. The

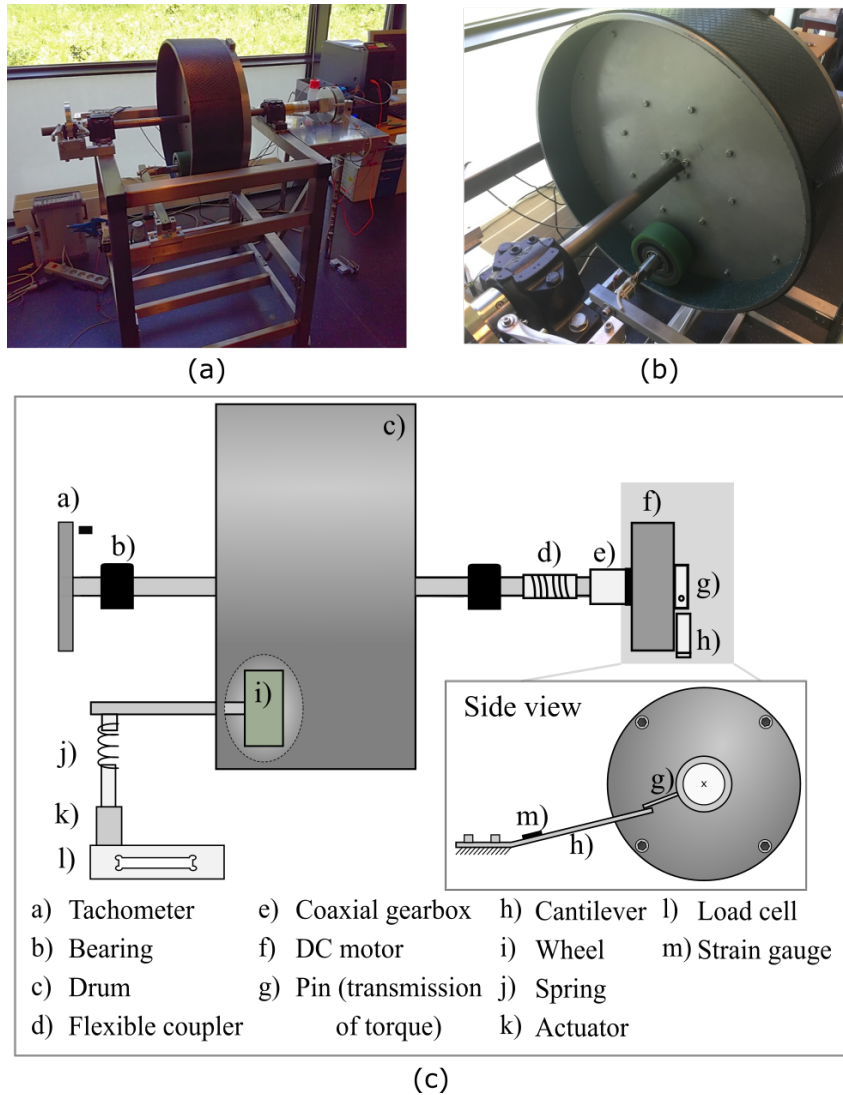


**Figure 5.2:** Test rig version 1. (a) Photo of the full test rig (b) Photo showing the inside of the drum with sandpaper attached. (c) Schematic illustration of the test rig showing how the different mechanical components are connected. Figures are taken from Hansen and Larsen (2017); Larsen et al. (2021)

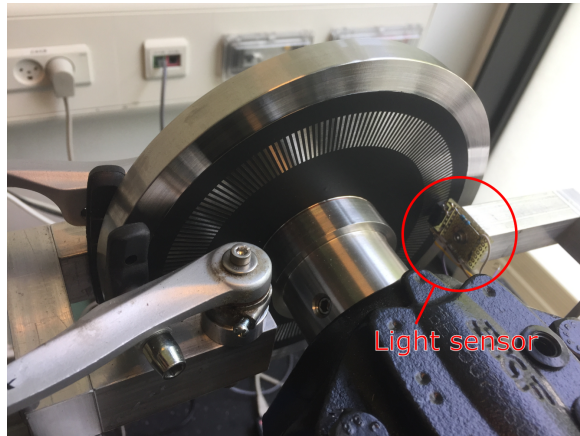


**Figure 5.3:** Picture of tachometer for test rig version 1 which consists of a light sensor and patterns with the 200 radial lines

actuator is mounted on top of a load cell, which measures the tension of the spring, and the load between wheel and drum.

For rotating the drum a 110 W DC motor (*GPM12*) is attached to the shaft, supported by a bearing stands centred horizontally on the drum's rotational axis for free rotation. The driving force from the motor is transferred to the drum shaft via a coaxial gearbox with a ratio 5:1. When the drum rotates, a small circular pin is pressed against a cantilever, due to the torque provided by the motor. The deformation of the cantilever is measured using two strain gauges mounted in a half-bridge configuration on the cantilever. From the deformation, we can calculate the torque provided by the motor. For more information about Ver1, see Hansen and Larsen (2017).

### 5.3.2 Test Rig Version 2 improvements

Test rig version 2 (Ver2), shown by a photo and a schematic illustration in Fig. 5.4, is a similar setup to Ver1 with important improvement. Major improvements consist of temperature control of the entire test rig, a new motor section design and improved drum deviation. Other smaller improvements include:

- Adjustable aluminium frame as setup mount for easier maintenance and further development
- Increased drum axle diameter to minimise bending
- Linear rail for improved wheel-height adjustment and rigidity
- New load cell for measuring the load between wheel and drum

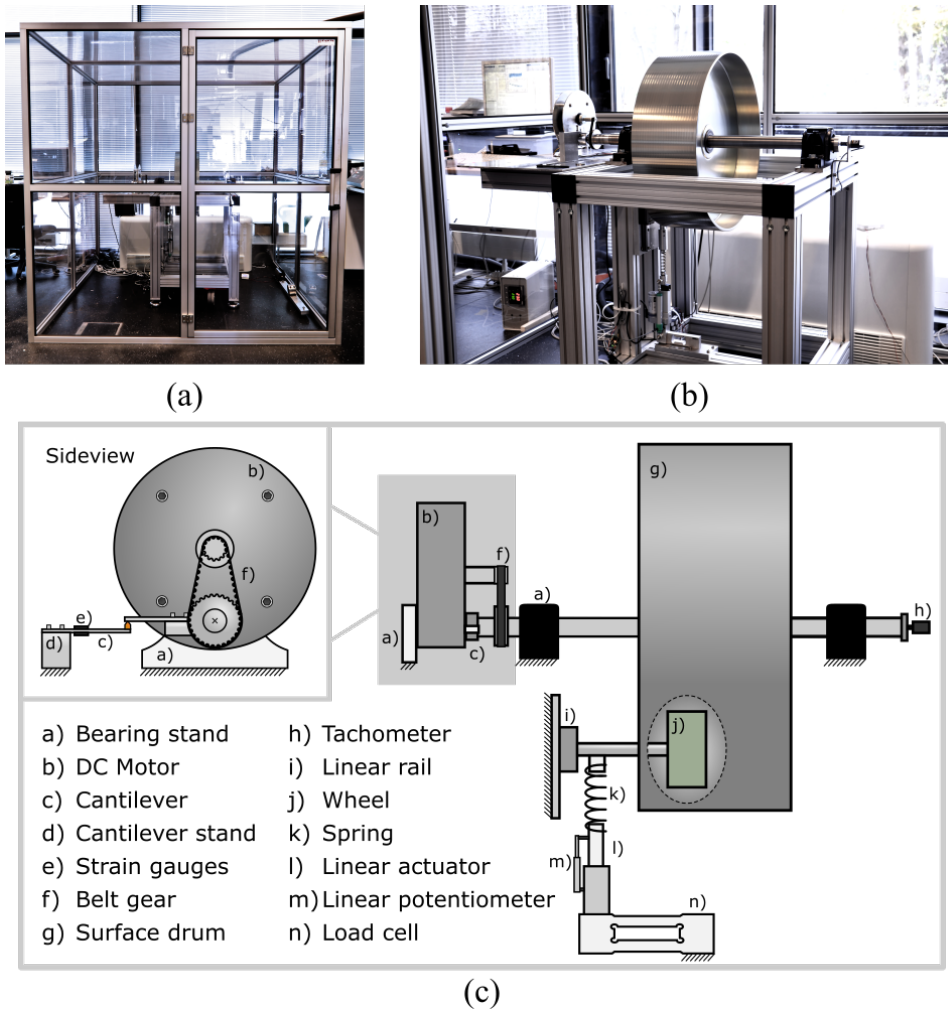


**Figure 5.4:** Test rig version 2. (a) The thermo-controlled cage of see-through acrylic panels forming a cube of side length 2 m with a door housing the test rig. (b) The steel drum with attached motor (left side of drum) and tachometer (right side of drum), mounted on an aluminium frame. The white box on the floor behind the frame is the air cooler and blower. The test wheel is placed to the left of the drum (hidden in the picture). (c) Schematic illustration of the test rig and how the different components are connected.

In the following, we will go through the improvements in Ver2, together with a presentation of the electrical construction.

The improved drum is a cylinder with an inner diameter of 538 mm made of galvanised iron. The drum is pre-processed by a lathe and is attached to the shaft by a self-centring attachment, making the inner diameter deviation below 0.01 mm. This is an important improvement when compared to Ver1, which has a deviation of approx. 1 mm. The smaller deviation improves the precision of the skim tests. To reduce the change of bending, due to the weight of the drum, a bigger iron shaft of 40 mm in diameter is used in Ver2. The drum and the shaft have a total weight of approx. 47 kg.

The tachometer in Ver1 for measuring the rotational velocity, have some smaller deviation due to centring issues. In Ver2 these issues are removed by updating to a commercial tachometer (E6A2-CW5C) with 100 cycles per.

For the wheel section, the improvements in Ver2 consist of using a vertical linear rail, connected to the wheel via a 30 mm iron shaft (see Fig. 5.5). As the load is increased in Ver1, it has been observed that the wheel tilts slightly towards the spring. By decreasing the shaft length to the wheel, and exchanging the pivoting arm with a vertical linear rail, the positioning of the wheel in Ver2 is more stable as load increases.

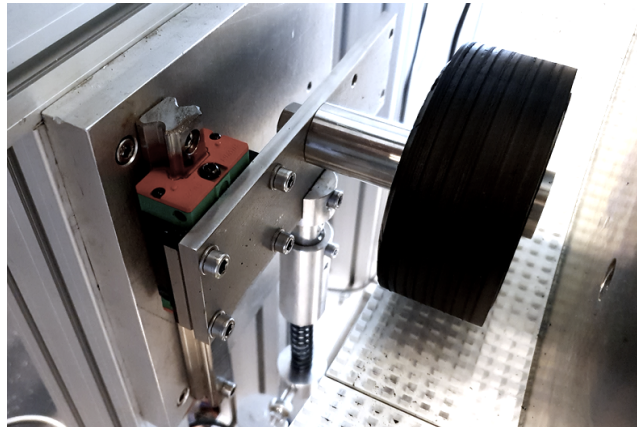


**Figure 5.5:** Picture shows the vertical linear rail in Ver2 connected to the wheel axle and an adjustable attachment to the spring. Also shown is the attachment of CON wheel and Tex9.

In the motor section, multiple changes have been made for Ver2. Instead of a coaxial gearbox, we use a belt gear with a ratio 5:1, to transfer the force from the motor to the drum. This is done because of a presumption of energy loss in the coaxial gearbox, as the gearbox becomes hot to the touch. Because of the belt gear, the motor is placed off-centre and balanced corresponding

to the shaft rotational axes as seen in Fig. 5.4(c). Preliminary tests have shown it is highly important, that all connections from the motor to the drum shaft are centred around the same rotational axis, to minimise errors in the measurements.

In Ver1 the pin and cantilever responsible for measuring the torque on the motor are grinding material away, making a small indent in the cantilever. This made measurements unreliable. As the indent was only noticeable after months of measuring is considered not to have had an effect in the work by Hansen and Larsen (2017). To remove the grinding of material, the design of the pin and cantilever are, in Ver2, changed to a flat pin and a cantilever with a thickness of 2.0 mm. The cantilever is also raised so the pin and cantilever are parallel when in contact. However, as grinding would still happen (see Fig. 5.6(a)) a triangular prism of bronze alloy is placed to lower the friction and wear (see Fig. 5.6(b)).

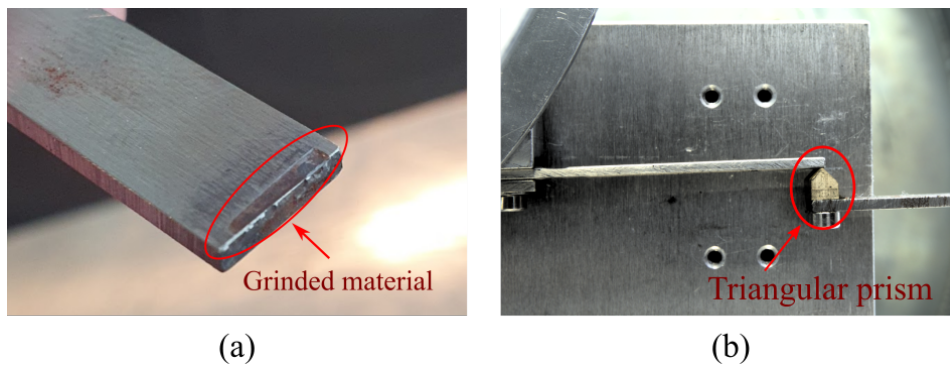


**Figure 5.6:** Pictures of test rig version 2 (a) Close-up picture of the cantilever tip, showing the indent from grinding. (b) Triangular bronze alloyed prism placed between the cantilever and pin from the motor to reduce friction and remove grinding.

As a new addition, Ver2 is placed inside a thermo-controlled cage consisting of a closed cubed room of side length 2 m. The cage is made of an aluminium frame and 2 mm thick acrylic panels and is installed by placing the frame on the floor. For temperature control, a heater and a cooler are placed inside the cage, controlled by a regulator which is measuring the temperature close to the wheel inside the drum. The cooler runs constantly to circulate the air while regulating the flow of cooling water. The heater is regulated by turning the power on and off. Stable temperatures can be achieved in the interval 16–39 °C with an estimated accuracy of 0.2 °C.

To control and perform measurements, multiple electrical components are needed. Figure 5.7 shows a schematic illustration of the electrical components.

The main electrical component is the computer running MATLAB, which is controls and receives all data to and from the test rig. From the computer, multiple electrical components are connected via Universal Serial Busses (USB).

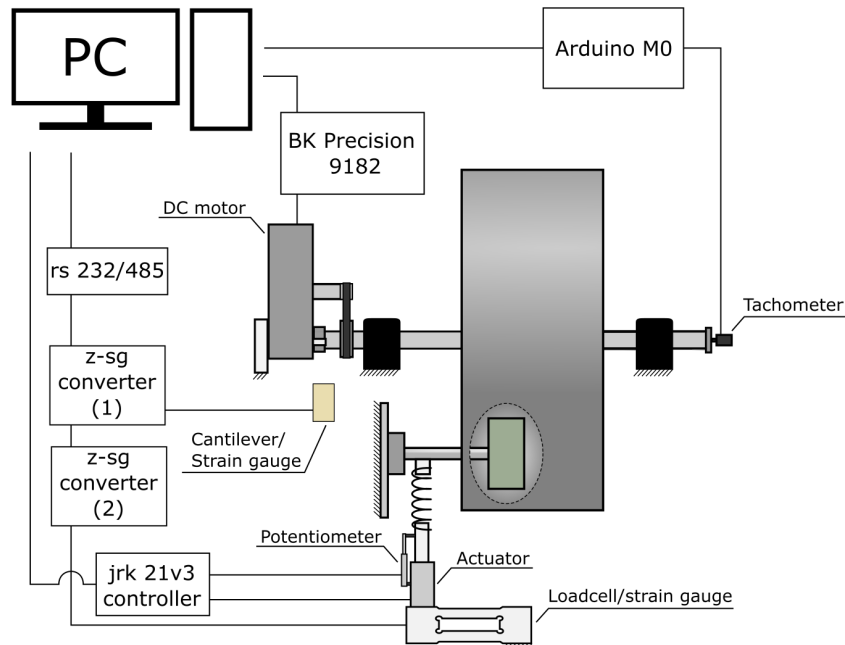


**Figure 5.7:** Schematic illustration of the electrical components and connection in test rig version 2.

Using an Arduino M0 board connected to the tachometer, the Arduino logs the cycles count for one second at a time and stores it. The cycle count for the latest interval can then be read by the computer.

For controlling the voltage on the DC motor, a power supply (BK Precision 9182) is connected via a two-wire connection. The power supply is controlled by the computer.

The actuator and the potentiometer are both connected to a motor controller (jrk 21v3). This can adjust the actuator to a specified position measured by the potentiometer. The position is specified from the computer.

The load cell is a piece of aluminium with strain gauges attached, capable of measuring shear deformation. As well for the strain gauges on the cantilever, the load cell is individually connected to a strain gauge input module (Z-SG). For the cantilever and load cell two strain gauges are mounted in a half-bridge configuration. The strain gauge input modules are connected to a USB to RS 232/485 converter, which is connected to the computer.

### 5.3.3 Calibration

To convert the electrical reading from the strain gauges, as forces are applied to the cantilever and load cell, we need to calibrate the strain gauges. For the strain gauge input modules, a calibration can be performed with a single known applied force. However, a test of the module calibration showed that using a series of measurements improved the calibration.

The calibration readings shown in this section are only for Ver2 measurements. Calibration readings for Ver1 are shown in Hansen and Larsen (2017).

#### Load Cell

To calibrate the load cell a scale is mounted to the wheel, while the actuator is in the highest setting. Here the wheel should not be in contact with the drum. The actuator is then lowered in discrete steps, which caused the spring to stretch and increases the force pulling the wheel towards the drum. This force corresponds to the load on the wheel when in contact with the drum. As the actuator is lowered the load and the strain gauges reading  $S_r$  are recorded. For the calibration protocol, the load is only increased, which is similar to the measuring protocol.

Shown in Fig. 5.8(a) is the readings and fitted linear relation for a single wheel. The calibration is performed for all test wheels and used temperatures. These calibrations show the same slope for the fitted linear relation.

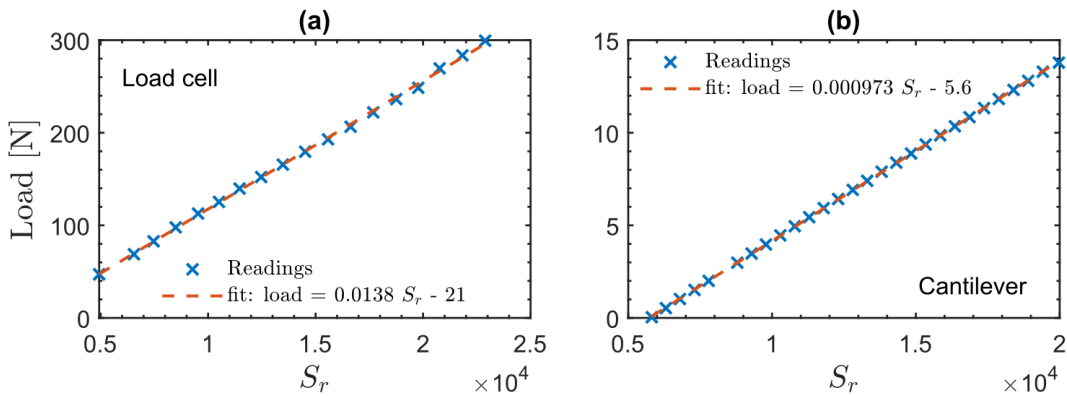


**Figure 5.8:** Calibration data showing the linear relation between load and string gauge readings  $S_r$  at 23°C (a) Load cell readings with shaft and wheel attached. (b) Cantilever readings.

To test if the measured force from the load cell corresponds to the load between the wheel and drum, we performed an additional measurement between

the drum and wheel shaft. This showed that the measure from the load cell corresponded to the load on the drum with little to no difference.

### Cantilever

To calibrate the cantilever, weights are suspended on a triangular prism where the pin from the motor is in contact. For each weight attached the strain gauges reading  $S_r$  and force were recorded. Shown in Fig. 5.8(b) are the readings at 23 °C and fitted linear relation. The calibration was performed for all the used temperatures, showing a small decrease in the slope of the fitted linear relation for a higher temperature. Compared to the load cell, which is independent of the used temperatures, the temperature dependence of the cantilever may come from the usage of thinner material and/or the strain gauges. To solve this issue the cantilever was calibrated for each tested temperature.

### 5.3.4 Load-Dependent Bearing Friction

In Sec. 5.2 we show the calculation of the RR force,  $F_{RR}$ , with the argument that bearings in the test rig are approximately load-independent. It is commonly known that bearing friction changes as different loads are applied. To prove the bearing friction is approximately load-independent, we calculate the changes in bearing frictions for Ver2 between skim test load and max load (approx. 210 N).

Both test rigs use four bearings: Two (SKF 1209 EKTN9) on the drum shaft, supporting the majority of the test rig, and two (SKF 6304) on the wheels. Each wheel has a pair of bearings, and are not interchanged from wheel to wheel. However, these bearings are of the same type and are assumed identical in friction.

The bearing friction values  $\tau_f(F_L)$  are acquired from the manufacture SKF bearing selecting tool<sup>2</sup>, for temperatures at 25°C and 180 rpm. Because the wheel bearings were modified with low viscosity lubrication, the acquired values are not correct for the bearings used in our test rigs. However, the calculation still shows an upper limit.

At the skim test, the drum bearings support approx. 470 N due to the weight of the shaft and the drum. When the wheel load is 210 N the drum bearings supports approx. 680 N. As the load is equally divided between the bearings, each bearing supports 235 N when no load is applied from the wheel, and 340 N when a load is applied from the wheel. From SKF we find  $\tau_f^{drum}$

---

<sup>2</sup><https://skfbearingsselect.com/>

for a single drum bearing:

$$\begin{aligned}\tau_f(235 \text{ N}) &= 0.0158 \text{ Nm} \\ \tau_f(340 \text{ N}) &= 0.0193 \text{ Nm}.\end{aligned}$$

Because the drum is affected by both bearings, the total  $\tau_r^{drum}(N)$  on the motor from the drum bearings is 0.0316 Nm and 0.0386 Nm. From this we find the unresolved contribution from the drum bearings on the motor when subtracting skim tests:

$$0.0386 \text{ Nm} - 0.0316 \text{ Nm} = 0.0070 \text{ Nm}.$$

The same calculation can be done for the wheel bearings. As an example we look at the Polyurethane (PUR) wheel, which is described in detail in Sec. 5.5. At skim test the weight of the wheel (2.6 kg) is supported by the bearings. Like before, we find  $\tau_f^{wheel}(N)$  for a single wheel bearing:

$$\begin{aligned}\tau_f(13 \text{ N}) &= 0.0021 \text{ Nm} \\ \tau_f(105 \text{ N}) &= 0.0066 \text{ Nm}.\end{aligned}$$

For both wheel bearings  $\tau_f^{wheel}$  results in 0.0042 Nm and 0.0132 Nm. Using the relation  $\tau^{drum} = \tau^{wheel} \frac{r}{R}$ , where  $r$  is the wheel radius and  $R$  is the drum radius, we find the contribution from the drum bearings on the motor is, respectively, 0.0008 Nm and 0.0026 Nm. Thus, the unresolved contribution from the wheels is

$$0.0026 \text{ Nm} - 0.0008 \text{ Nm} = 0.0018 \text{ Nm}.$$

Hence, the total unresolved contribution from the drum and wheel bearing is

$$0.0070 \text{ Nm} + 0.0018 \text{ Nm} = 0.0025 \text{ Nm}.$$

This corresponds to approx. 1.6 % of the total amount of  $\tau_{motor}$  for the PUR wheel in Ver2. Because the unresolved contributions only affect the results within the known uncertainties of our measurements (see Sec. 5.4), we argue that the bearing friction does not have an effect on the results, and consider the bearings to be approximately load-independent.

### 5.3.5 Measured Load Hysteresis

When the wheel is in contact with the drum, a contraction in the actuator increases the load on the wheel as the spring is being stretched. Notice that actuator position "0" correspond to the actuator being fully extended while

contracting at higher position settings. As the actuator extends or contracts, it is assumed that the measured load is independent of the movement. However, load measurements on Ver2 show this is not the case, as hysteresis is observed (see Fig. 5.9(a)). In the actuator position 2000-2500 (approx. 200 N) we observe a difference of 12-13 N, between increasing loads or decreasing loads. The decrease in difference close to the lowest and highest positions may indicate that there is friction in the vertical linear rail or hysteresis in the potentiometer.

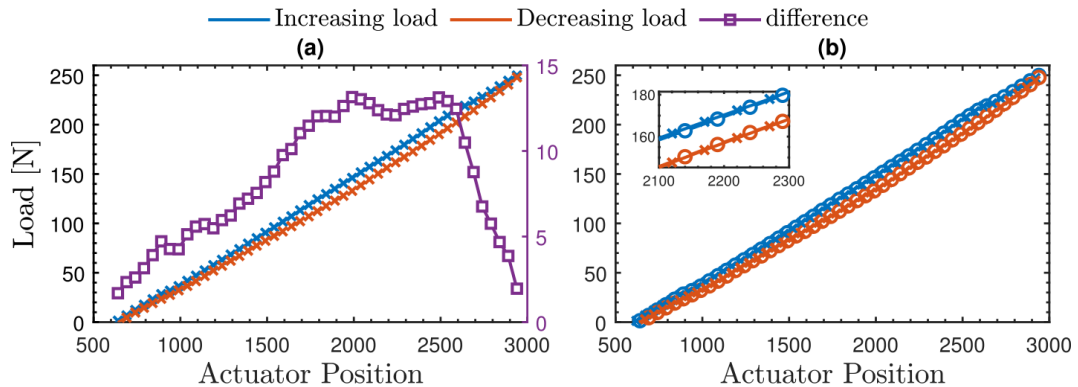


**Figure 5.9:** Load measurements for test rig version 2 at different actuator positions with contact between wheel and drum, while the drum is rotating. (a) Measurements for increasing and decreasing the position of the actuator. Also plotted is the difference between increasing and decreasing load measurements, scaled by the right y-axis. (b) Two repeated measurements to show reproducibility for increasing and decreasing positions.

Even though the measured loads depends on the actuator movements, by only increasing or decreasing the actuator position, the load measurements are still reproducible as shown in Fig. 5.9(b). This fact is very important for the measuring protocol.

## 5.4 Measuring Protocol

Just as the constructional aspects of the test rig have been improved from Ver1 to Ver2, so has the measuring protocol been updated to improve Ver2. Because the measuring protocols are still similar, we will start by introducing the protocol used for Ver1, followed by the protocol updates in Ver2.

### 5.4.1 Test Rig Version 1

For given static parameters, i.e., surface texture and wheel, an experiment consists of a series of measurements of varying speed and load. For Ver1

in this thesis, most of the measurement runs consist of two different speeds and five different loads, leading to a total of 10 different combinations. This includes skim test load. As described in Sec. 5.2, the skim test identifies the contribution to the RR from parasitic losses, e.g. air resistance, bearing friction, etc.

When performing multiple measurements runs with the same static parameters, the measurements are planned such that no measurements runs with identical static parameters are performed consecutively. This is to minimise the effect of any “inherited” properties.

When performing multiple measurement runs with the same static parameters, the measurements are planned such that no measurement runs with identical static parameters are performed consecutively. This is to minimise the effect of any “inherited” properties.

The attachment of surface textures is done by thin double-sided tape. When changing surface textures, the tape is removed from the texture, i.e. sandpaper or 3D prints, and drum. Because measurements are performed directly on the drum, any residue is meticulously removed.

As the test rig consists of moving parts which give incentive to vibration, continuously maintenance is performed between each measurement run. This consists of removing any unwanted tensions in the wheel section by loosening and re-tightening bolts and cleaning the open-wheel bearings and re-applied lubrication, as dust increased the friction in the bearings.

Two lists containing angular velocity target values and actuator position target values are given to the control software. The actuator position values set the actuator and specify the spring deformation, hence, the load on the test wheel. Due to hysteresis in the load measurement, as shown previously, the load is only changed by increasing the actuator position.

The angular velocity is regulated by increasing or decreasing the DC motor voltage using a PID-controller. When the drum has maintained a stable rotational velocity for 30 minutes, the power to the motor is kept constant, and a fixed number of data points are logged for averaging.

When data for a single target have been collected, the angular velocity is changed to the next target value. When the target values for the angular velocity have been examined, a new target value for the load is set, and so on (compare Fig. 5.10). Each measurement runs for Ver1 containing 10 different combinations, which took around 24 hours.

While measuring the rotational velocity, load and torque by the motor  $\tau_{motor}$ , are monitored continuously. An example of the output from one measurement run is shown in Fig. 5.10, illustrating the protocol. The gap between each target setting is the stabilisation time.

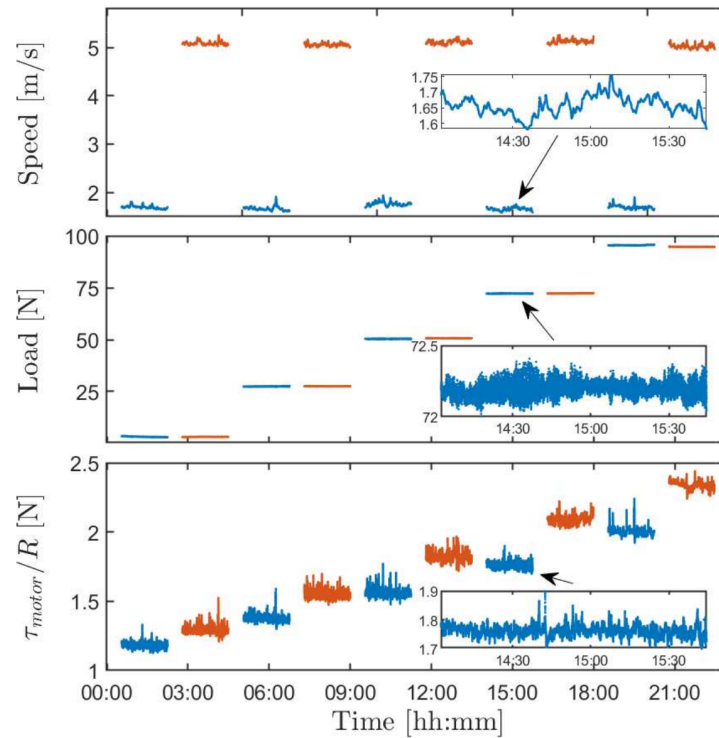


**Figure 5.10:** Raw data from test rig version 1 illustrating the protocol for a measurement run with NBR wheel on the steel surface. Each run starts at “zero” load, providing the skim test reading for determining the parasitic losses, then loops through the target speeds (here two), before changing to higher load and repeating. Figure taken from Larsen et al. (2021)

#### 5.4.2 Test Rig Version 2 Changes

Due to the improvement of Ver2, several changes have been added to the measuring protocol for better data collecting. The improvements can be listed as:

- Thermo-controlled cage protocol
- Reduced measuring time
- Continuously speed control

With the introduction of the thermo-controlled cage, it is possible to control the ambient temperature of the test rig, adding a new controllable static parameter. When changed, approximately 24 hours is given from setting a new temperature, to the start of a new measurement. This is to ensure the test rig has reached a stable temperature before starting.

To reduce the measuring time in Ver2, the PID-controller is upgraded to

automatically estimate when the drum has reached a stable rotational velocity. The estimation is done by evaluating the last 60 seconds of the measured rotational velocity. If the measurements are stable within a specific margin of error, the drum is estimated stable. After the stabilisation time, additional 10 minutes is measured with velocity adjustment. An example of the output from one measurement run is shown in Fig. 5.11, as data is continuously logged. The small gaps in the data comes from a transition between different settings and the starting of the PID-controller. Due to these improvements, the measuring time for a single target combination is reduced from approx. 120 minutes to approx. 15 minutes.

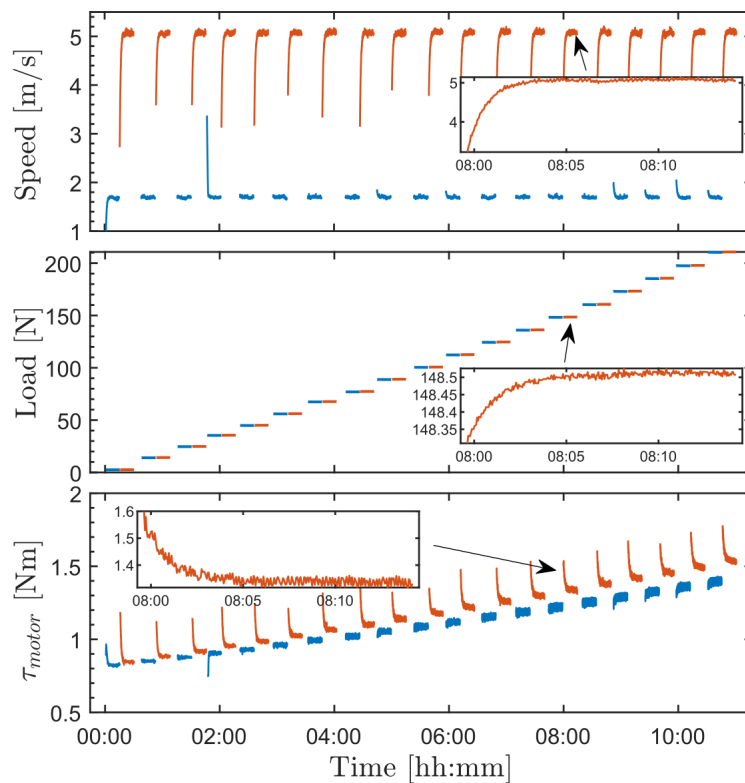


**Figure 5.11:** Raw data from test rig version 2 illustrating the protocol for a measurement run with NBR wheel on steel surface. Each run starts at “zero” load, providing the skim test reading for determining the parasitic losses, then loops through the target speeds (here two), before changing to higher load and repeating.

## 5.5 Test Wheels

For the experiments, four different wheels were used (NBR, PUR, CON and POW) as shown in Fig. 5.12.



**Figure 5.12:** Picture of the used test wheels. From the left; Nitrile butadiene rubber (NBR), Polyurethane rubber (PUR), Continental Rubber (CON) and Powerslide CST 150 Air Tire (POW).

**NBR** is nitrile butadiene rubber, a material which is softer than PUR and CON. The rubber is cast onto an aluminium rim on which two ball bearings are attached. The wheel is 126 mm in diameter and 50 mm in width. The rubber thickness is 16 mm, the weight of the wheel is 1.2 kg.

**PUR** is polyurethane. This specific wheel is used for indoor pallet lifters. The rubber is cast onto an iron rim on which two ball bearings are attached. The wheel is 124 mm in diameter and 50 mm in width. The rubber thickness is 10 mm, the weight of the wheel is 2.6 kg.

**CON** is a rubber mixture aimed at reducing the RR of truck tyres produced by the tyre manufacture Continental AG, the detailed composition of which is not known to us. The rubber is glued onto an aluminium rim on which two ball bearings are attached. The wheel is 114 mm in diameter and 45 mm in width. The rubber thickness is 10 mm, the weight of the wheel is 1.1 kg.

**POW** is the roller-skating wheel “Powerslide CST 150 Air Tire”, made of Natural rubber / Styrene Butadine rubber. The wheel is 150 mm in diameter and 31 mm in width, with a weight of 0.31 kg. Compared to the other test wheels, POW has a C-shaped profile, similar to a standard bicycle wheel.

Test have shown a softer wheel give rise to larger RR changes for different parameters. Because of this, we chose a low tyre pressure of 1.0 bar for the POW wheel. Additionally, 1.0 bar is specifically used as the study by Veldt (2020) investigates pressures at 1.0, 2.0, and 3.0 bar, which is used in Sec. 7.6. Before every measurement, the POW wheel was regulated to 1 bar.

All solid wheels are attached to the test rigs using the same steel shaft. Changing the wheel is done by simple pressing the shaft on and off and locking with an end cap. Due to the difference in axle size, POW is attached using a separate steel shaft.

## 5.6 Surfaces

For the experiments, a total of 18 different surfaces textures were used. These consisted of measurements directly on the drum, i.e. steel surface, five types of sandpaper, and 11 different 3D printed surfaces textures.

### 5.6.1 Sandpaper

For the used sandpaper, different grit sizes were chosen according to the grit size standard FEPA: P400, P160, P60, P32 and P24.

The profiles of the different sandpapers were measured using a profilometer, borrowed from the Danish Road Directorate, (see Fig. 5.13(a)). By placing the sandpaper below the profilometer on a flat floor, a laser sensor in the profilometer measures the distance from the sensor to the surface of the sandpaper. The position of the sensor is measured with an accuracy of 0.1 mm, and the distance from the sensor to the surface is measured with an accuracy of 0.1  $\mu\text{m}$ . A total of seven different paths was measured, each at 1.5 m, for each type of sandpaper. Examples of the resulting curves are shown in Fig. 5.13(b). The Mean Profile Depth (MPD) value was calculated according to ISO (2019) based on these profiles.

For P400, P60, P36, and P24 sandpapers, a detailed 3D height scan of 4mm  $\times$  4mm area is added in Fig. 5.13(b) to illustrate the difference in surface texture. These 3D scans of the surfaces were performed by Univ Gustave Eiffel, IFSTTAR using the InfiniteFocus system from Alicona.

When fitted inside the drum, the sandpaper was fitted by cutting the ends at a 45° angle to minimise sudden bumps as the sandpaper repeats.

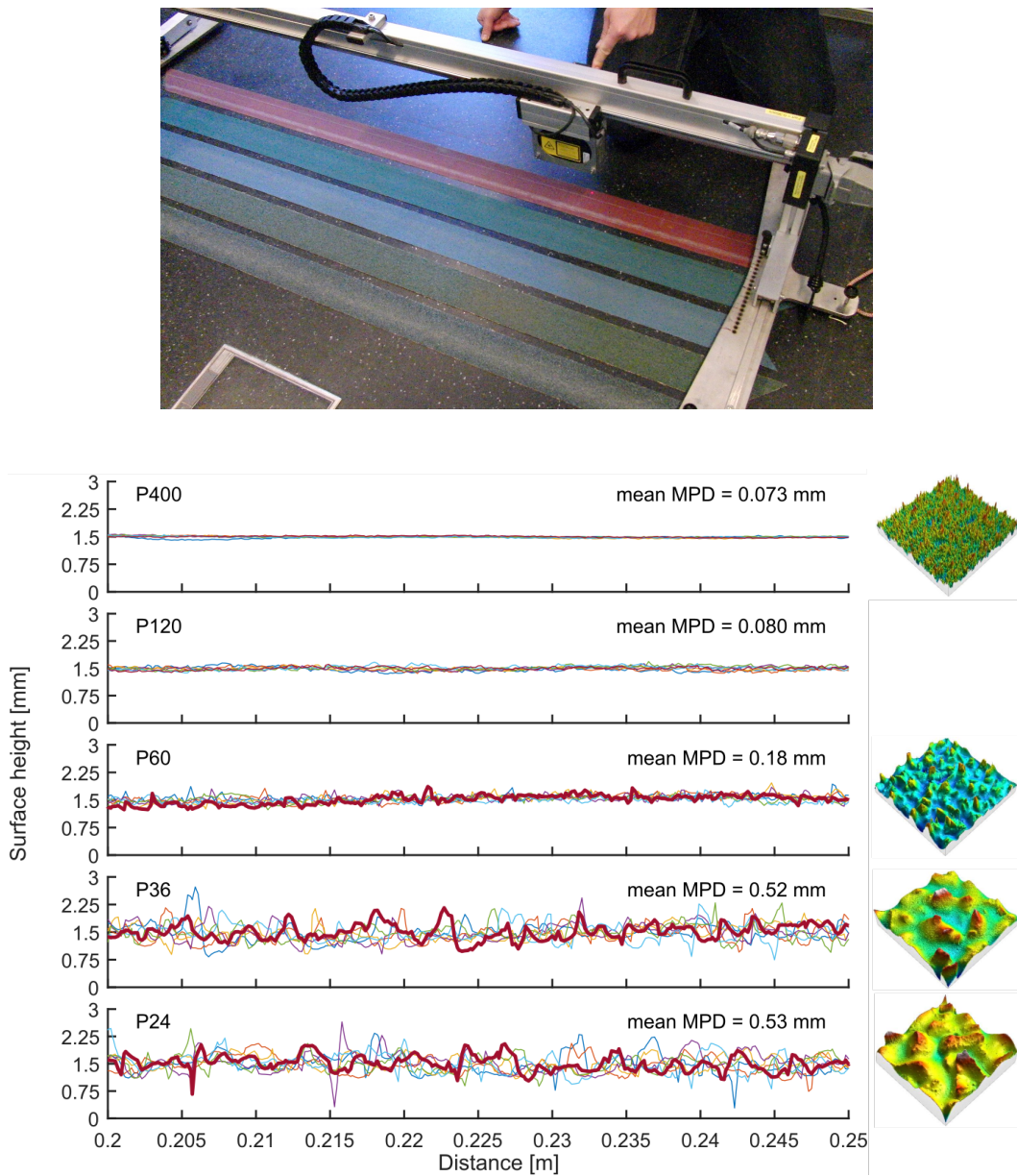


**Figure 5.13:** Profile characterisation of sandpapers used in the experiment. (a) Profilometer used to measure the surface profile of the five types of sandpaper. (b) Texture measurements for the following sandpapers: P400, P120, P60, P36 and P24. Each plot shows a section of the seven contour measurements over a length of 1.5 m. The MPD is calculated from the entire length of the seven contours. To the right of each contour plot (except for the P120 sandpaper) a high-resolution 3D height scan of a 4 mm×4 mm area is shown, made by Univ Gustave Eiffel, IFSTTAR. Figure taken from Larsen et al. (2021).

### 5.6.2 Geometric Pattern - 3D Print

By 3D printing technology, surfaces textures can be produced and tested in various shapes and sizes, compared to sandpapers and road replicas.

For an easy approach, the main chosen texture is made of identical cuboids on a regular square array, which from a geometrical perspective is a simple body, while having an easy calculated MPD and peak fraction. In Fig. 5.14 the texture with the cube design is shown with the different parameters, together with a ramp surface texture design. The ramp design is created to investigate the influence of asymmetric texture for RR.

By using double-sided tape added to the part as seen in Fig. 5.14(b), nine parts are attached inside the drum. Additional RR is to be expected from energy loss due to the tape. The magnitude of this contribution is tested by measurements on a flat 3D printed surface (Tex0), see Sec. 7.5.

The MPD is calculated (based on the ISO standard (ISO, 2019)), by averaging MSD as presented in Sec. 3.1. Referring to Fig. 5.14 this leads to

$$\text{MPD} = \frac{HWD}{(D+W)^2}. \quad (5.8)$$

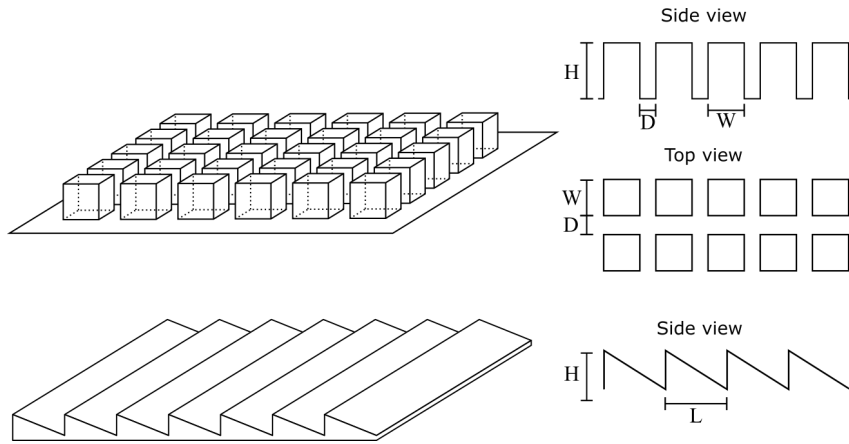


**Figure 5.14:** Illustration of the cube texture design, and ramp texture design with the used parameters; peak height (H), distance between peaks (D) width of peaks (W) and length of ramps (L).

In Chap. 4 the toy model predicts that the RR is inversely proportional to  $P_f$ . For the presented cube design  $P_f$  can be calculated by

$$P_f = \frac{W^2}{(W+D)^2}. \quad (5.9)$$

Notice that the calculation is exclusively based on surface textures dimensions. As we will discuss in Sec. 7.3.2, this does not fully describe the interaction between wheel and surface texture.

For a texture on a flat surface, there is no boundaries for how big or small homogeneous geometrical textures can be in the travelling direction. Unfortunately, this is not the case for textures in a drum. When a drum is rotating, the texture needs to repeat itself for every full rotation. If not, the texture is not homogeneous in the travelling direction. To achieve homogeneous geometrical textures on a drum, the surface texture is limited to have textures that repeat at the length of the drum circumference. See the produced textures and measurements results in Chap. 7.3.2.

Other types of textures were considered, such as hemispheres and pyramids, but was scrapped because of the load dependence when calculating contact patches.

The different surface textures in this study are produced by using a Fused Deposition Modeling (FDM) system (Ultimaker 3). Because optimal parameters are not easy, when 3D printing and may vary between locations, only the nozzle size of 0.4 mm and layer height 0.1 mm to 0.2 mm is noted. Because the Ultimaker 3 cannot print the full drum surface within one print, the surface is divided into nine equally sized parts, see Fig. 5.15. Parts with the same texture is printed with the same layer height. the layer height is chosen so a single part would take approx. 22 hours to print.

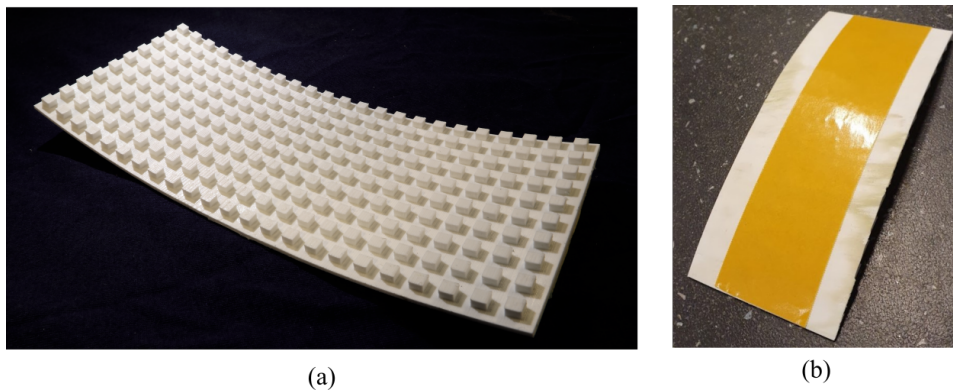


**Figure 5.15:** (a) One of nine 3D printed surface parts, printed with a curvature to fit the surface drum. (b) Picture showing surface part with thin double-sided tape used for attaching the surface part to the drum.

Polylactic Acid (PLA) was selected as the printing material due to the low cost and the higher tensile strength of 110 MPa, when compared to Ac-

rylonitrile Butadiene Styrene (ABS) which have a tensile strength of 44 MPa<sup>3</sup>. PolyVinyl Alcohol (PVA) was used for supportive structure when printing, because of the curvature on the printed part.

## 5.7 Data Treatment Protocol

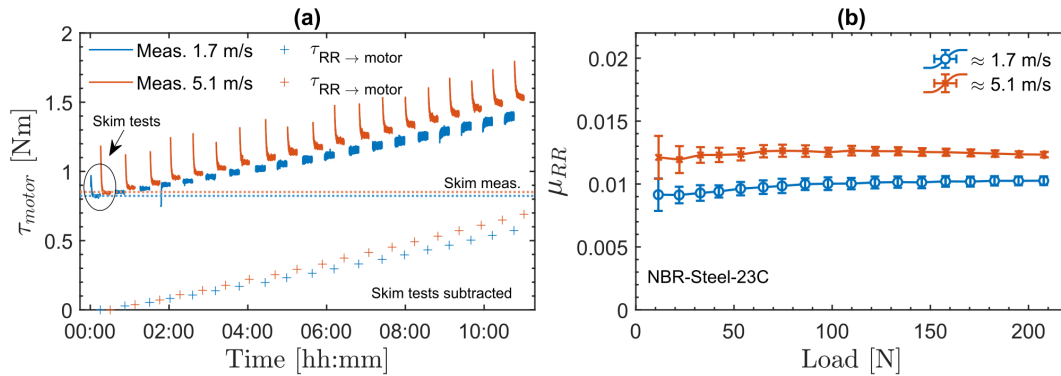
To ensure a stabilised value, the load and resistance forces are determined by averaging only part of the data points for each target setting: For Ver1 the last quarter, for Ver2 the last 5 minutes.

Figure 5.16(a) shows an example for Ver2 of how the skim measurements marked by the dotted lines is subtracted from the motor-torque, to determine the torque contribution from RR, shown by the crosses. From this we obtain the RR,  $F_{RR}$  (Eq. (5.6)).

The RR coefficient is defined as,  $F_{RR}$ , divided by the load,  $F_L$ .

$$\mu_{RR} = F_{RR}/F_L \quad (5.10)$$

When calculating  $\mu_{RR}$ , load measurements are assumed “zero” at skim measurements by subtracting the skim test values. This removes possible load measurements from friction in the linear rail and makes measurement independent of the wheel weight. Figure 5.16(b) shows the  $\mu_{RR}$  average values plotted as a function of the average load for the target position, with the standard deviation as error bars.



**Figure 5.16:** Determining the rolling resistance coefficient for test rig version 2. (a) Plot of the measured torque, showing how parasitic losses from skim test reading are subtracted. (b) Rolling resistance coefficient,  $\mu_{RR}$ , as a function of load for the NBR wheel on a steel surface obtained from the data in (a). Error bars indicated standard deviation.

<sup>3</sup>Tensile strength values is obtained from dk.rs-online.com

## 6 Contact Patch Experiments

The area of a tyre which is in contact with the surface will be larger or smaller depending on the load. This area is called the contact patch or footprint of a tyre and is a property which has been studied previously. For instance, El-Zomor (2019) shows that, for a car tyre, the contact patch decreases as tyre pressure increases, and concludes that the load and inflation pressure of the tyre are important factors for the contact patch. From this one could argue that studies which investigate the influence of tyre pressure, such as the studies by Sina et al. (2015) and Mashadi et al. (2019), are directly linked to the investigation of contact patches, even though there is no mention of it.

Studies using smaller pneumatic tyres for measuring rolling resistance (RR) are not uncommon. An example of this is to use bicycle wheels to investigate tyre properties such as RR and contact patches Dressel (2013); Dressel and Sadauckas (2020). In a recent study by Veldt (2020) the influence of tyre pressure on RR was measured for the POW wheel using the Ver1. As shown in Fig. 6.1, measurements for the POW wheel with different tyre pressures were performed for a range of different loads and speeds. In Fig. 6.1,  $\mu_{RR}$  is plotted for the POW wheel at tyre pressures of 1 bar – 4 bar as a function of load at speeds of 2.1 m/s, 3.4 m/s and 5 m/s.

For the measured tyre pressures,  $\mu_{RR}$  decreases as the tyre pressure increases, with a smaller decrease for higher tyre pressures. This is especially noticeable at higher loads. Similar results have been found in other studies (Michelin, 2003; Sina et al., 2015; Mashadi et al., 2019). A possible explanation for this is a relation between the contact patch and  $\mu_{RR}$ , which we to find in Sec. 7.6.

### 6.1 Contact Patch Measuring

To measure the contact patch between a wheel and a surface we considered using black colouring. However, colouring needs to be applied directly to the wheel, which could interfere with later RR measurements. Thus using colouring was scrapped for pressure-sensitive sheets.

The pressure-sensitive sheets used in these measurements are the Fujifilm Prescale Ultra Super Low Pressure (LLLW) sheets, which consist of two separate sheets: A developer and a colour-forming sheet. By pressing the sheets

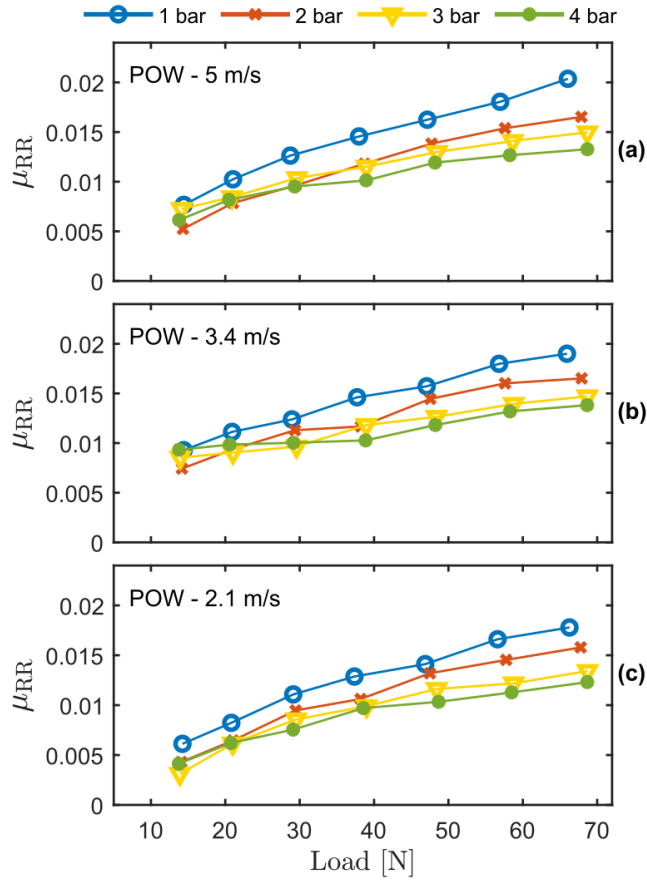


**Figure 6.1:** Rolling resistance coefficient,  $\mu_{RR}$ , as a function of speed and pressure, at speeds of 2.1 m/s, 3.4 m/s and 5 m/s. Data is taken from Veldt (2020).

together, a reaction happens on the developer sheet. Depending on the pressure, more or less colour appears. In this thesis, the magnitude and pressure distribution between the tyre and surface is not evaluated. Only the area in which there is contact is considered.

As mentioned in Sec. 5.2.2, the curvature of the drum influences the size of the contact patch. As the surface curves in the same direction as the wheel, more of the surface will be in contact with the wheel and therefore increase the RR. Hence we measure on both the curved drum surface and a flat surface.

The measuring is performed by placing the desired surface and test wheel on Ver2 and placing the pressure-sensitive sheets in between. When testing a flat surface, an additional steel plate, with a thickness of 7 mm, is then placed inside the steel drum beneath the test wheel. For more consistent measurements the drum is locked in place when contact patch measurements

are performed. This is especially important for measurements on flat surfaces. The desired load is applied between the wheel and drum surface and sustained for 2 minutes. The pressure-sensitive sheets are then photographed within 30 minutes of applying the load, for later analyses as seen in Fig. 6.2.

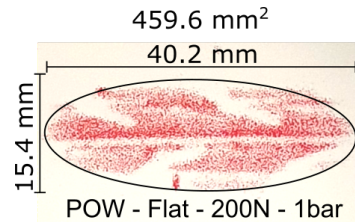


**Figure 6.2:** Picture of a pressure sensitive sheet after load has been applied by the POW wheel. Noted in the picture are the dimensions of the contact patch and a fitted ellipse with area size.

When analysing contact patches on the pressure-sensitive sheets, the marking is measured using area calculation in the vector graphics software Inkscape, by assuming the contact patches are ellipses. The ellipse is fitted to the marking by eye.

Initially, all wheels were tested on a steel surface with multiple textures. However, due to unclear edges on the pressure-sensitive sheets and deformations from the camera lens, only results from the POW wheel on curved and flat steel surfaces were obtained. These results are shown in Sec. 7.6.

## 7 Measurements and Results

In this chapter, the results from the experimental work are presented for the rolling resistance (RR) measurements and the contact patch measurements.

The RR measurements presented have been made using test rig version 1 (Ver1) and test rig version 2 (Ver2). Ver1 is used for measuring RR as a function of the load on five different grit sizes of sandpaper and a steel surface. Ver2 is used for a much larger set of experiments, shown in Tab. 7.2.

The number of repetitions of each experiment varies from 1 to 11 times, due to the importance of the individual experiment and time constraints. It would have been preferred to have done all measurements using Ver2, but due to the extensive development of and issues with Ver2, Ver1 was used for the sandpaper measurements. The use of Ver1 is also a natural follow-up to the work by Hansen and Larsen (2017). Ver2 was prioritised for measurements using geometric patterns, see Tab. 7.1.

The following RR measurements for Ver2 are a mean of all identical measurement runs. The number of repetitions is shown on each figure as #R. #R is excluded if only one measurement run was performed. For a full overview of all individual measurements using Ver2 see Appendix A. Most of the work presented in this section is to be published in two papers, which can be found in Appendix C.1 and C.2.

### 7.1 Repeatability

To test the repeatability of Ver2 between every interchanging of textures, a measurement using of NBR wheel on the steel surface was performed, thus making multiple measurements in the same configuration over a long period of time. Besides showing the repeatability of the test rig, this would also indicate if any significant changes have happened over a longer time period due to wear and tear.

Figure 7.1 shows  $\mu_{RR}$  with load at speeds of 1.7 m/s and 5.1 m/s for 11 repeated NBR-Steel measurements over four months. The data points show the mean of the measured  $\mu_{RR}$  for each measurement run, with the error bars indicating the standard deviation. From the data points its clear that the test rig is not completely able to reproduce measurements over a longer period of time, and that there is no clear tendency between the experiments. Nonetheless, the measurements seem to have a spread around a common mean value

**Table 7.1:** Overview of produced 3D surface textures and their parameters. \*T7 is a repeating ramp texture representing asymmetric textures. The notation of f (forward) and b (backward) is used. \*\*Ramp dimensions: Length 5 mm, height 2 mm.

Ref. name	H [mm]	W [mm]	D [mm]	MPD [mm]	$P_f$
T0				0	1
T2	1	2	2	0.25	0.25
T4	4	2	2	1	0.25
T5	2.5	1.5	3	0.48	0.129
T6	2.5	1.5	4	0.4959	0.0744
T7*	2	**	**	1	
T8	12	3	3	3	0.25
T9	2.5	4	4	0.625	0.25
T10	2.5	5.19	5.19	0.625	0.25
T11	2.5	7.2	7.2	0.625	0.25
T14	1.5	1	5.15	0.2042	0.0264

**Table 7.2:** Overview of performed experiments on test rig version 2.

Wheel	Focus	Temp. [°C]	Surface	Wheel	Focus	Temp. [°C]	Surface
NBR	Load	16	Steel	CON	Load	16	Steel
			Steel				Steel
		23	T0			23	T2
			T2				T4
			T4				T5
			T5				T6
			T6				T8
			T7f				T9
			T7b				T10
			T8				T11
			T9				T14
			T10				
			T11				
			T14				
	39	Steel	39	Steel			
Speed	23	23	Steel				
PUR	Load	23	Steel	POW	Load	23	Steel
			T2				T2
			T5				T5
			T6				T6
			T9				T7f
			T10				T7b
			T11				T9
			T14				T10
Speed	23	23	Steel				

at different loads and are assumed to have a normal distribution. Even though it is hard to notice due to the amount of data points, no systematic changes are observed over the period of measuring, indicating that wear and tear, as the distribution is independent of the time of measuring.

As the load increases the variation in  $\mu_{RR}$  decreases between each performed experiment. This is more visible in Fig. 7.2(a) where the mean of the repeated experiments at the different loads is calculated and two times the standard error of the mean (SEM) is shown in the error bars in Fig. 7.2(a) and as a separate plot in Fig. 7.2(b). From Fig. 7.2(b) it is also clear that, with the exception of the lowest load, SEM of  $\mu_{RR}$  is similar for the two speeds. From the error bars in Fig. 7.2(a), there is strong evidence that there is a difference in the measurements, indicating a good interval in the range of loads.

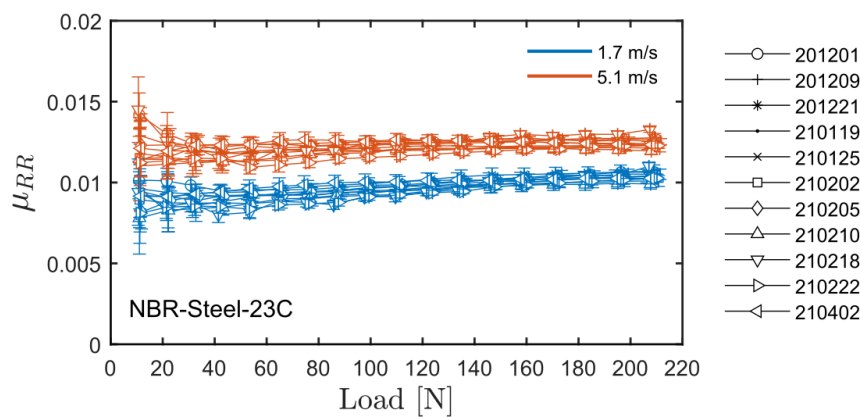


**Figure 7.1:** rolling resistance coefficient as a function of load for the NBR test wheel at the two speeds. Results are presented for eleven experiments repeated over a period of four months, with error bars showing the standard deviation for a single data point of each experiment. Dates in the have the format YYMMDD.

## 7.2 Load, Speed and Temperature

Load, speed and ambient temperatures all influence RR is of interest (Ejsmont et al., 2016, 2018). Using Ver2, these parameters can be controlled and studied. In this section load, speed and ambient temperature are regulated on a flat steel surface.

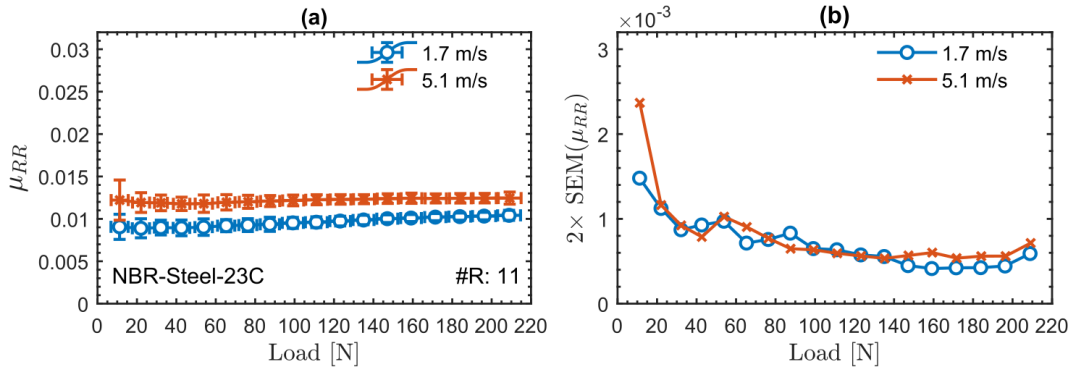


**Figure 7.2:** Data for 11 repeated NBR-Steel-23C experiments. (a) Mean of the rolling resistance coefficient,  $\mu_{RR}$ , with load at speeds 1.7 and 5.1 m/s. Errorbars show two time the standard error of the mean, SEM. (b) Plotted is SEM( $\mu_{RR}$ ) of the  $\mu_{RR}$  shown in (a).

## Load

In Fig. 7.3  $\mu_{RR}$  is shown as a function of load, at speeds 1.7 and 5.1 m/s for each test wheel. The loads shown are the full load range of the test rig. The data points represent the mean of measurement runs ( $\#R$ ) with the same parameters. From the shown data multiple observations can be made from the influence of Load. 1) For all test wheels  $\mu_{RR}$  increases with loads between 40 N and 220 N, and a higher  $\mu_{RR}$  at higher speeds. 2) The solid test wheels (NBR, PUR and CON)  $\mu_{RR}$  increases slowly at a constant rate at loads between 40 N and 220 N, compared to the POW test wheel at 1 bar. NBR and PUR may even be considered constant. 3) The POW wheel increases in  $\mu_{RR}$  with load while approaching a plateau, and have a much higher  $\mu_{RR}$  compared to the solid test wheels. 4) In the load range 10 N to 40 N, for NBR and CON,  $\mu_{RR}$  decreases with the load. 5) If we only were to observe  $\mu_{RR}$  in the range 40 N to 220 N for the POW wheel, the increase in  $\mu_{RR}$  can be considered constant. When considering the repeatability of the measurements (see Fig. 7.1), it is unclear whether or not the test wheel is increasing or decreasing, due to the high uncertainty in the loads up to 40 N.

The assumption of  $\mu_{RR}$  being near-constant, due to a near-linear relation between RR and load is not clearly reflected from these results.

In a collaborative work, a contact model has been used for calculating RR while implementing the specific dimensions for the experiential setup and tested sandpaper (Larsen et al., 2021). The contact model is based on a 3D time-dependent approach developed by Yin et al. (2015) for the rolling of a rigid body on a viscoelastic half-space and is solved using the prediction/correction algorithm developed by Cesbron and Yin (2010). The results

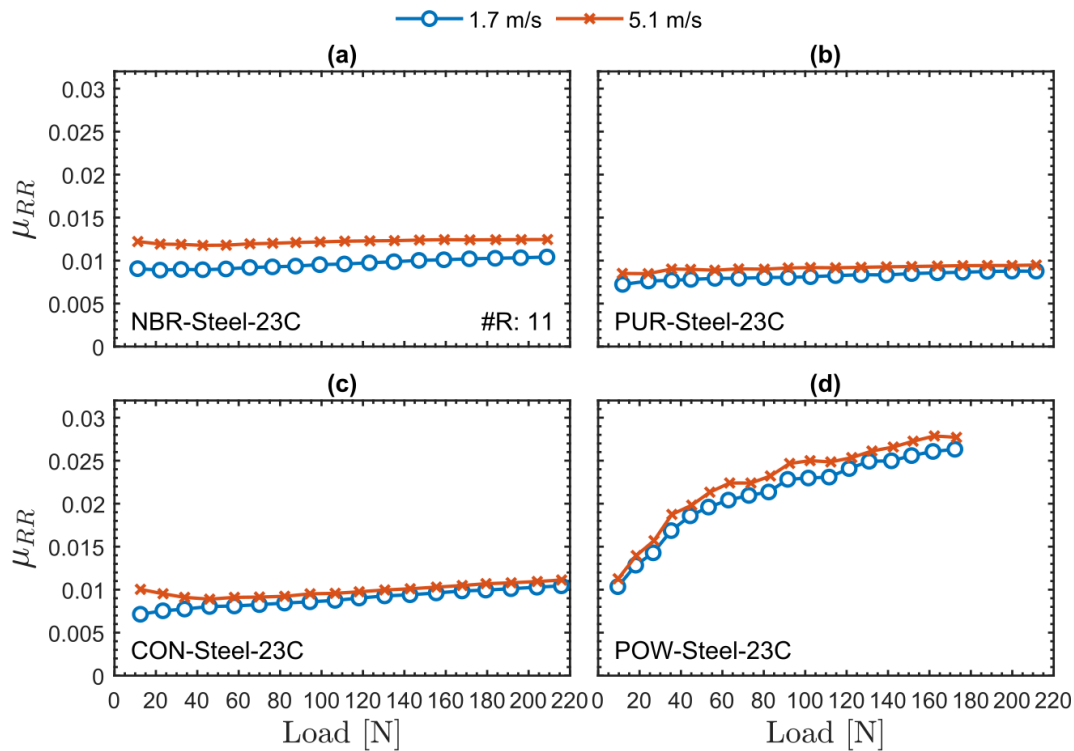


**Figure 7.3:** Rolling resistance coefficient,  $\mu_{RR}$ , as a function of load on the test wheels (NBR, CON, PUR and POW) at speeds 1.7 and 5.1 m/s. NBR wheel results is a mean of 11 repeated measurement runs (#R). Measurements are made using test rig version 2.

from the model as seen in Fig. 7.4, shows a constantly decreasing rate for  $\mu_{RR}$ , for a solid NBR wheel. For the measurements, this tendency is not noticeable for the solid test wheel, but only for the POW wheel.

Comparing the different test wheels, it is clear that the POW wheel stands out, as the  $\mu_{RR}$  is much higher for POW than for the solid test wheels while approaching a plateau. A similar conclusion has been seen made by Grappe et al. (1999), where RR on a bicycle wheel was being measured. This might be due to the pneumatic tyre being susceptible to deformation, compared to the other solid wheels.

### Temperature

Plotted in Fig. 7.5 is  $\mu_{RR}$  at different loads for NBR, CON and POW, at ambient temperatures of 16°C, 23°C and 39°C. From the data, it is clear that as the ambient temperature increases  $\mu_{RR}$  decreases across the whole load range. This is consistent with previous, where a similar relation was observed

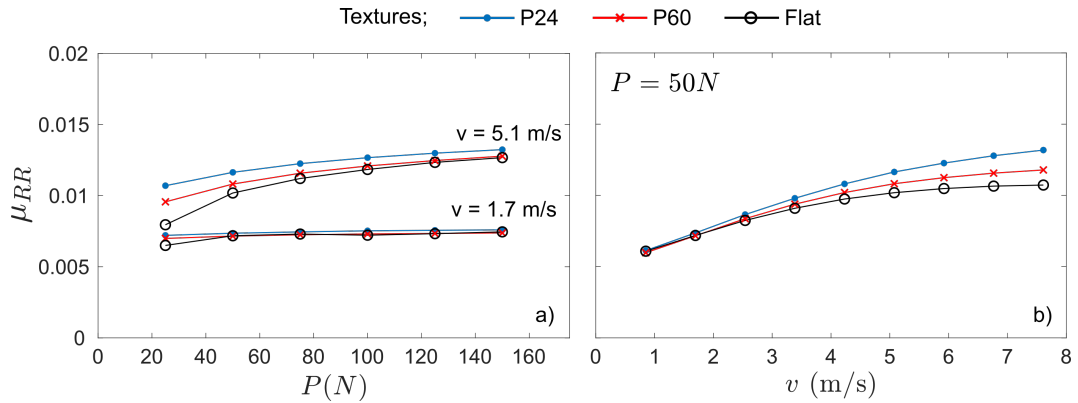


**Figure 7.4:** Averaged coefficient of rolling resistance  $\mu_{RR}$  for sandpapers P24 and P60 compared to the final rolling resistance coefficient  $\mu_{RR}(T)$  on the smooth surface as a function of the total normal load  $P$  for two different rolling velocities: 5.07 m/s and 1.69 m/s (a) and as a function of rolling speed,  $v$ , for  $P = 50$  N (b). Figure taken from Larsen et al. (2021).

for passenger car and truck tyres (Ejsmont et al., 2018).

Considering the viscoelastic properties, the decrease in RR for increasing temperatures, indicate the temperature and load ranges, at which we are measuring, correspond to frequencies below the peak frequency in energy loss.

## Speed

When changing the rotational velocity of a wheel, the frequency at which the wheel material is being deformed is changing proportionally, i.e. higher rotational velocity equals higher deformation frequency. Because of this, we expect a change in RR as the loss modulus is changed. However, depending on the material and frequency, the RR may increase or decrease.

In Fig. 7.6  $\mu_{RR}$  is plotted as a function of speed, for NBR, CON and POW, at three different loads. For the solid CON wheel  $\mu_{RR}$  increases with speed almost at a constant rate at each load, with the NBR wheel having a small decrease in the rate at higher speeds. The POW wheel  $\mu_{RR}$  is increasing for the lower speeds but is stabilising for speeds above 2.5 m/s. Because this tendency is only valid for the pneumatic wheel, the flattening of  $\mu_{RR}$  compared to the solid wheels, may be due to an increase in temperature in the wheel. As seen in Fig. 7.5, an increase in temperature reduces  $\mu_{RR}$ , but for a pneumatic wheel, the pressure will also increase because of the gas expansion due to the dissipated energy, making the contact patch between the wheel and the surface smaller, see Sec. 7.6.

If excluding the POW measurements, the increase in RR for increasing

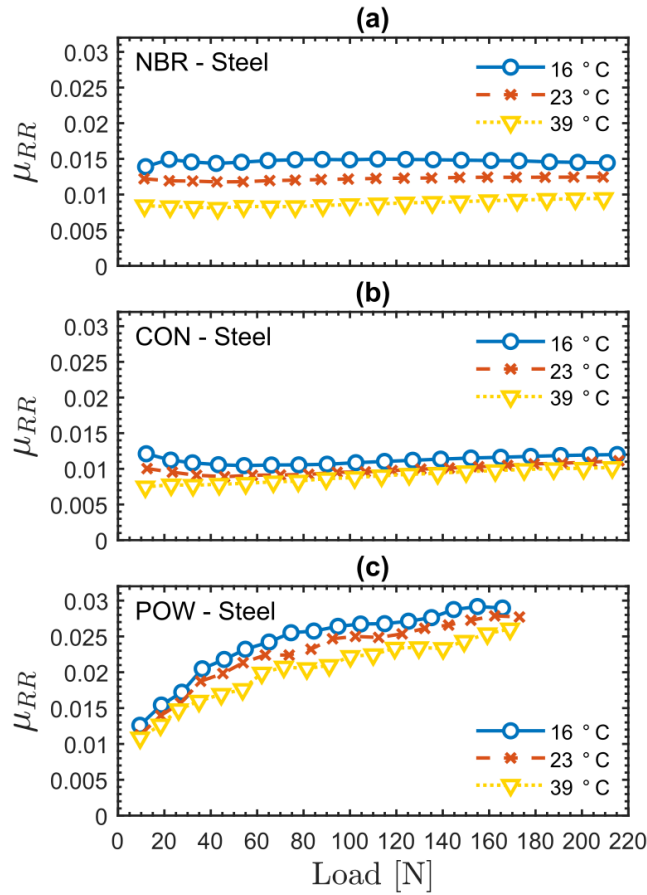


**Figure 7.5:** RR coefficient plotted as a function of the load at different temperatures for the NBR and CON wheels, on the steel surface at 5.1 m/s. The NBR wheel results at 23 °C represent a mean of eleven repeated experiments, compare Fig. 7.1.

speeds, indicates furthermore that our settings at which we are measuring corresponds to frequencies below the peak frequency in energy loss.

The contact model (see Fig. 7.4) shows results where  $\mu_{RR}$  increases from 0.06 to 0.11 with a decreasing rate for the NBR test wheel from 1 m/s to 7.5 m/s. The experimental results are similar for NBR, showing the same tendency, while having a slightly higher absolute  $\mu_{RR}$ . For POW the same tendency is more visible, while CON is only showing a small increase making a possible decrease in rate invisible.

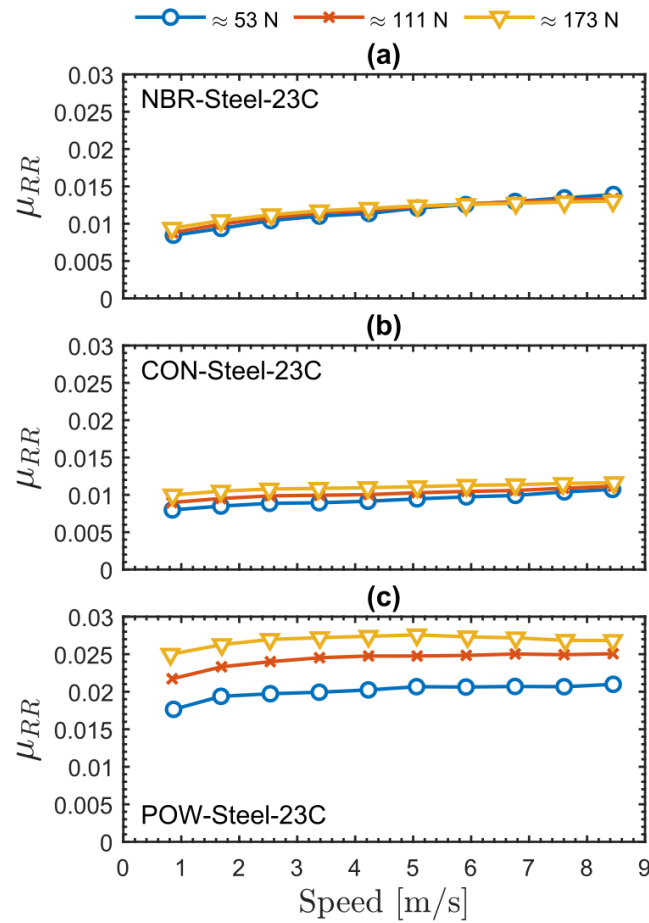


**Figure 7.6:** Rolling resistance coefficient,  $\mu_{RR}$ , as a function of speed on the flat steel surface, using the test wheels POW and NBR.

### 7.3 Surface Texture

Most studies investigate the influence of surface texture on RR by measuring specific road samples/segments. This approach can for instance be seen in the study by Anfosso-Lédée et al. (2016), where coast-down and trailer methods are measured on large stretches of road.

The process of making a large stretch of road is cumbersome, and even more so if several have to be made, for the purpose of having different textures to test on. The method used by Riahi et al. (2020) comes past this by using a comparably small circular road sample with a 10 cm diameter in a laboratory setup. However, up until now the most used laboratory method have been the drum method, where the usage of road segments requires the laboratory set to be fairly large, as seen by the 5.5 m inner diameter internal BAST drum

(Sandberg et al., 2011b, pp. 51).

A common practice to avoid the usage of big road samples is to use sheets with texture and attach it to a drum. The study by Ejsmont et al. (2017) investigated the relationship between surface texture and RR. In this study trailer measurements were done on different road segments with different surface textures, together with drum measurements using a replica of the surface texture from the road segments, both indicating texture has a significant impact on tyre RR. Also used in the study, is a Safety Walk anti-slip self-adhesive surfacing, which is similar to sandpaper.

Sandpaper is often used as a surface texture in RR measurement, due to it being a standardised texture, which is very common and easy to use.

In the following we will use sandpaper of different grit sizes as a surface texture. This is the same approach as Hansen and Larsen (2017) which the following sandpaper measurements is an extension to.

### 7.3.1 Sandpaper

Using Ver1 RR measurements where performed on a steel surface and sandpapers: P400, P120, P60, P36 and P24 (see Sec. 5.6.1). The results and conclusions in this section is from the study by Larsen et al. (2021).

Figure 7.7 show repeated measurements using Ver1 when measuring on sandpapers. RR coefficients,  $\mu_{RR}$ , for the NBR wheel on the smooth steel, P60, and P24 textures, are shown as a function of load for the two measured speeds. The measurements for the two textured surfaces shows a higher repeatability than for the smooth steel surface.

In Fig. 7.8  $\mu_{RR}$  is plotted as a function of load for speeds at 1.7 and 5.1 m/s for each type of sandpaper. Each data points represent the mean of three (in a few cases more) measurements with identical parameters. The error bars show the standard deviations for each mean. For the results, several observations can be made. 1) The NBR RR coefficients lie consistently above the PUR results for identical target settings. This reflects the different viscoelastic properties of the two different materials. 2) There is a clear speed dependence of  $\mu_{RR}$  for the NBR wheel, while the PUR results are much less dependent on speed. Again, this reflects the different viscoelastic properties of the rubbers. 3) For both wheels there is an increase in RR coefficient with load for all studied surface textures. This could be because we measure at quite small loads and that the curves saturate at higher loads. 4) There is a clear increase in the RR coefficient with greater surface textures for both wheels and both studied speeds (Larsen et al., 2021). This is consistent with other studies (Willis et al., 2015). Note that the P36 sandpaper results lie consistently above P24, which should have a coarser texture.

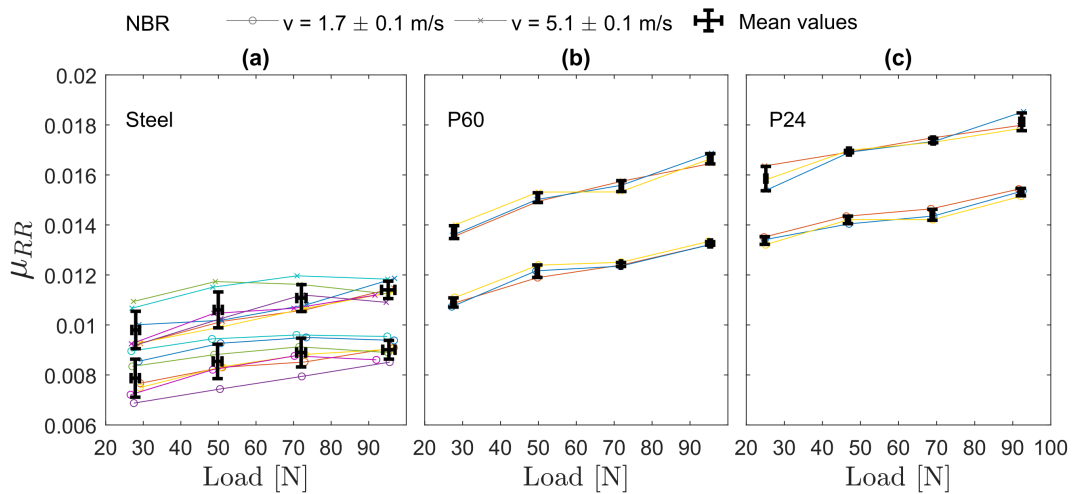


**Figure 7.7:** Repeated measurements of the rolling resistance coefficient as a function of load for NBR wheel (Larsen et al., 2021).

In Fig. 7.9  $\mu_{RR}$  is plotted against the MPD value for a fixed load and speed. The trend is an increase in the RR coefficient. The data points are not monotonously increasing, though, which indicates, especially given the accuracy of the results, that the MPD measured values do not capture the essential properties of the surface texture for RR. Note that the two wheels show nearly identical behaviour in this plot, only shifted slightly in the absolute level of the RR coefficient, emphasising that the ordering of the textures is not coincidental (Larsen et al., 2021).

The results indicate that MPD does not correlate well with the  $\mu_{RR}$  for all surface textures. This is consistent with the works of Sandberg et al. (2018); Ejsmont and Sommer (2021), which lead to them suggesting improved methods like the use of enveloping. The same conclusion is made later for surfaces with geometric patterns.

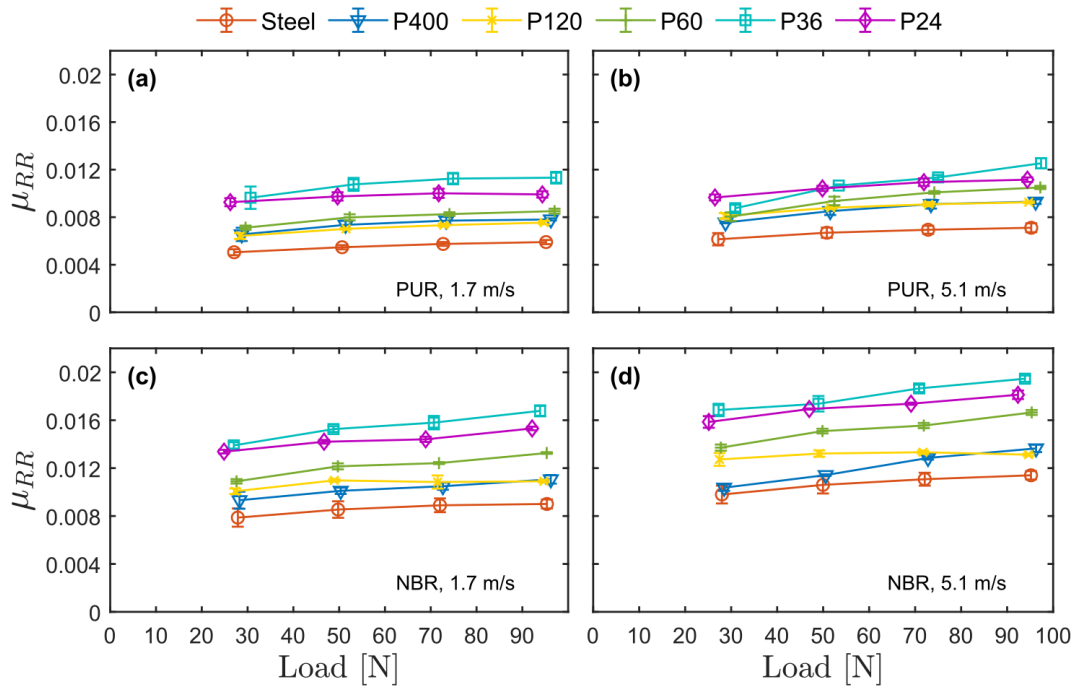


**Figure 7.8:** Rolling resistance coefficients. (a-d) As a function of load and surface texture for PUR and NBR wheels at a speed of 1.7 m/s and 5.1 m/s. (Larsen et al., 2021).

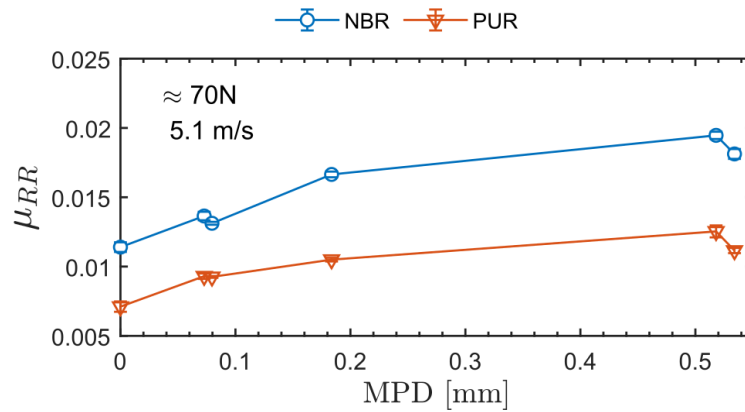


**Figure 7.9:** Rolling resistance coefficient measurements as a function of the MPD-values. NBR and PUR wheel at a load of 70 N (Larsen et al., 2021).

### 7.3.2 Geometric Pattern - 3D Print

As mentioned earlier, the use of sandpaper as surface texture makes it easy to control and change between different surface textures. However, sandpaper introduces complex and randomised surface textures, as seen for the specific grit sizes in Fig. 5.13(b), which conflicts with the goal of this study, since we need to control the surface texture to a high degree.

The study by Parry (1998) investigates the relationship between various functional properties of road surfaces and texture. This includes RR measurements using an indoor drum method at the Dynamics Laboratory at Dunlop Tyres Ltd in Birmingham. Different textures were added to the drum: Sandpaper, various epoxy replicas of real road surfaces and four special surfaces with simple geometric patterns as seen in Fig. 7.10.

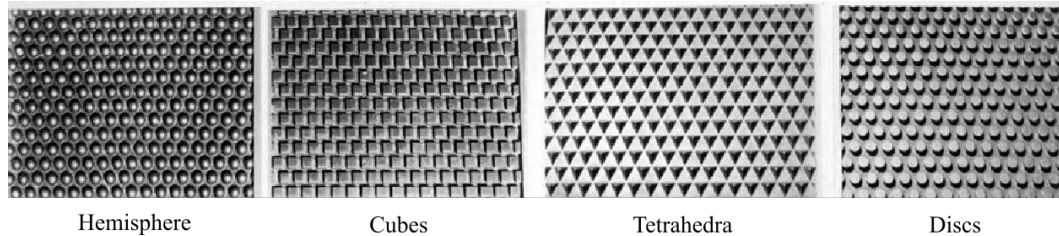


**Figure 7.10:** Pictures of the geometrical polymer resin cast surface textures used by Parry (1998).

Parry (1998) concludes that RR can be predicted by the contact area and the surface roughness and that the shape and size of the texture peaks influence RR. Larger and sharper surface textures have a higher RR.

We measured  $\mu_{RR}$  on surface textures similar to those used in Parry (1998). These surface textures were 3D printed in stiff plastic materials (see Sec. 5.6.2). All measurements in the following sections were done on Ver2 (see Appendix A).

#### MPD

In Fig. 7.11,  $\mu_{RR}$  is plotted as a function of MPD for the different 3D printed textures, at 5.1 m/s and two different loads. Visually we can conclude that there is no clear correlation between  $\mu_{RR}$  and MPD (this is further supported by the fact that measurements with similar MPD show clear differences in  $\mu_{RR}$ ).

#### Peak Fraction - Toy Model

Inspired by the toy model presented in Chap. 4, we investigate the peak fraction,  $P_f$ , as a predictor of RR. Before looking at the measured relationship

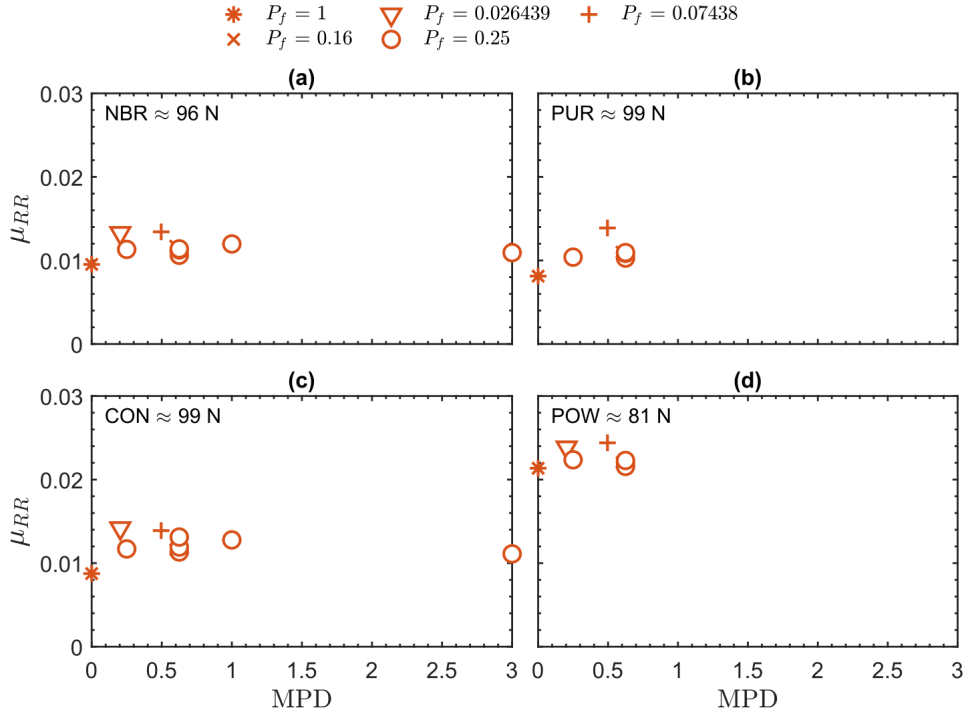


**Figure 7.11:** Rolling resistance coefficient,  $\mu_{RR}$ , plotted against MPD for all four test wheels at 5.1 m/s at a single load. The symbols indicate the peak fraction (unit peak fraction corresponds to the steel surface which has zero MPD).

between RR and  $P_f$ , it should be noted that depending on the placement of the test wheel on the geometric patterned surface and the width of the test wheel, the actual  $P_f$  values may differ slightly from the  $P_f$  values presented in Sec. 5.6.2. For the data presented, test measuring of the wheel placement shows a variance of up to 8 % between the calculated and the actual  $P_f$  values. This does not influence our conclusions. For simplicity in presenting the data, only the calculated  $P_f$  values are used.

In Fig. 7.12,  $\mu_{RR}$  is plotted as a function of peak fraction for the different 3D printed textures, at a single load and speed 5.1 m/s. From the data, there is no clear tendency for all wheels besides a small decrease over the entire  $P_f$  range.

As shown,  $\mu_{RR}$  has only a weak dependence on  $P_f$ , similar to MPD. However, there is a tendency that a lower  $P_f$  implies a higher  $\mu_{RR}$ . From the model fits, the two constants  $C_0$  and  $C_1$  are extracted for each combination of wheel, load and speed, to calculate the predicted model values  $\mu_{RR}^{\text{global}}$  (Eq. (4.3)) and  $\mu_{RR}^{\text{local}}$  (Eq. (4.4)).

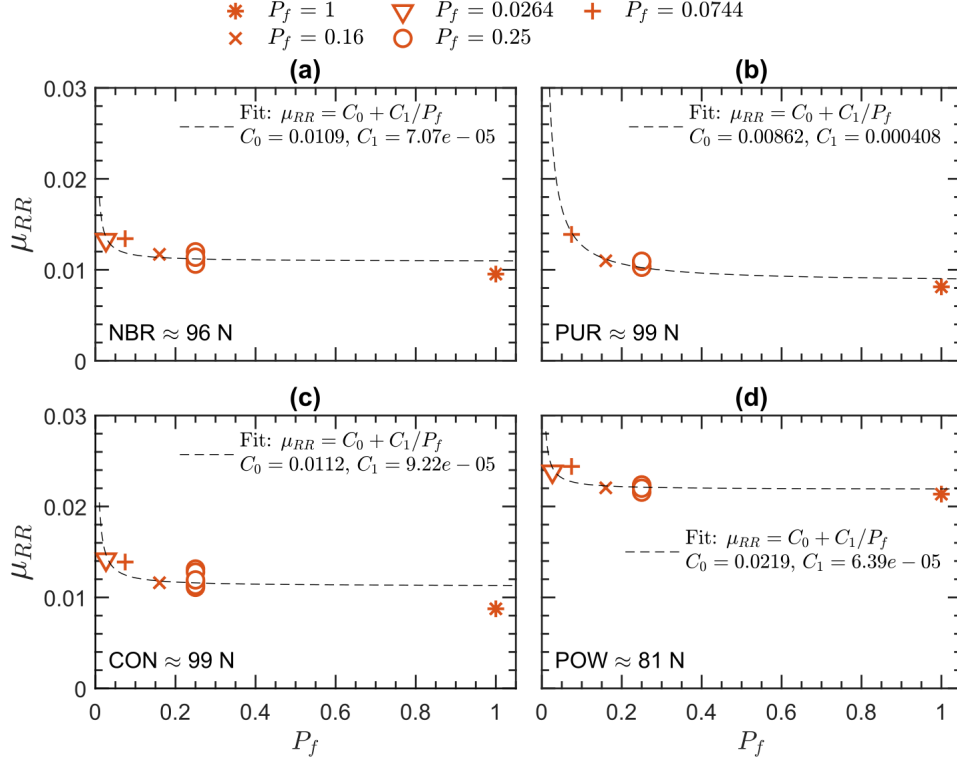


**Figure 7.12:** Rolling resistance coefficient,  $\mu_{RR}$ , as a function of peak fraction,  $P_f$ , on the test wheels (NBR, CON, PUR and POW) measured at a speed of 5.1 m/s. Tyre pressure for the POW was regulated to 1 bar before starting the experiment. The fit to data is from the toy model presented in Chap. 4.

To obtain a reliable fit of Eq. (4.2), a certain variation in  $\mu_{RR}$  is necessary. From Fig. 7.13 plotting the variance,  $\sigma^2 = \frac{1}{N-1} \sum_{i=1}^N (\mu_{RR,i} - \langle \mu_{RR} \rangle)^2$ , of our  $\mu_{RR}$  measurements we observe PUR and CON to have the largest variations. Thus, we expect the fit for PUR and CON to be most reliable, predominantly at higher loads.

As long as the mechanical properties of the wheel behave as described in Sec. 2.1, the RR force is proportional to the load. However, for an increasing load at some point, the linearity begins to break down. Since  $\mu_{RR}^{\text{global}}$  reflects the contribution from the global wheel deformation, while  $\mu_{RR}^{\text{local}}$  from the local deformation from indentation, the strain deformations related to  $\mu_{RR}^{\text{global}}$  are much smaller than those to  $\mu_{RR}^{\text{local}}$  deformation. Hence, we expect  $\mu_{RR}^{\text{local}}$  to become non-linear and thus load-dependent at significantly lower loads than  $\mu_{RR}^{\text{global}}$ .

With the exception of the POW wheel, which is less reliable due to a low

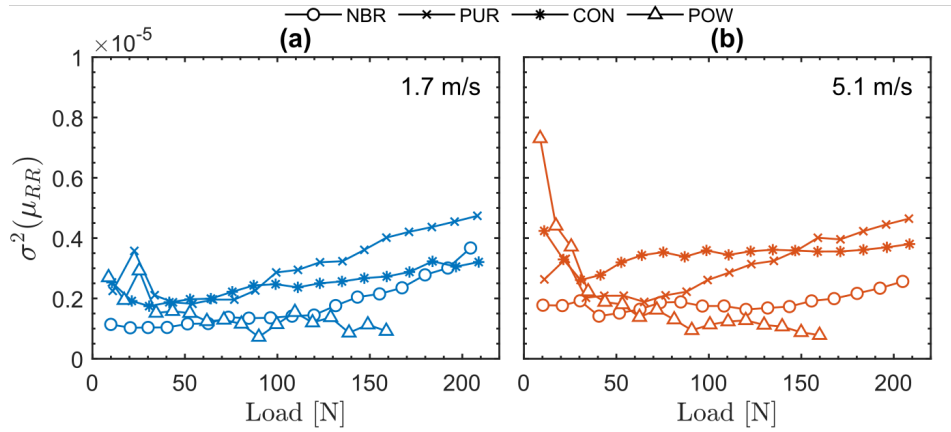


**Figure 7.13:** Variance of the RR coefficient,  $\sigma^2(\mu_{RR})$ , for the different surface textures (excluding T7), plotted as a function of load. A large variance implies a better determination of the constants  $C_0$  and  $C_1$ .

variance, in Fig. 7.14 we see that  $\mu_{RR}^{\text{global}}$  is near-constant as a function of load, while in Fig. 7.15  $\mu_{RR}^{\text{local}}$  is observed to increase consistently with load. This validates our expectations of load dependency.

In regards to speed, Fig. 7.14 shows that a higher speed leads to a higher  $\mu_{RR}^{\text{global}}$ . Looking at Fig. 7.15, the same speed dependency in  $\mu_{RR}^{\text{local}}$  is not observed.

We expect both  $\mu_{RR}^{\text{local}}$  and  $\mu_{RR}^{\text{global}}$  to have a speed dependency due to the frequency-dependent loss modulus. For measurements on a flat surface, as seen in Fig. 7.6, a small frequency-dependent loss is observed, which is consistent with the  $\mu_{RR}^{\text{global}}$  data. A possible reason why the local deformations do not show this dependence is that the frequencies related to the local deformations are considerably higher than that of the global deformation. If the frequencies related to the local deformations are much closer to the peak frequency than that of the global deformation, a considerably smaller speed dependency is expected.

### Predicting RR - $P_f$ vs MPD

Based on the measurements in Fig. 7.9, which was limited to a single load, we concluded that there is no clear correlation between  $\mu_{RR}$  and MPD, hence MPD appears to have little predictive power in determining  $\mu_{RR}$ .

In a statistical analysis involving all data taken at 23 °C, we attempt to determine which of the two quantities, MPD or  $P_f$ , is best at predicting  $\mu_{RR}$ . For simplicity a linear fit is used to determine the dependence of  $\mu_{RR}$  on MPD and  $P_f$ , to determine the quality of MPD respectively  $P_f$  as a predictor.

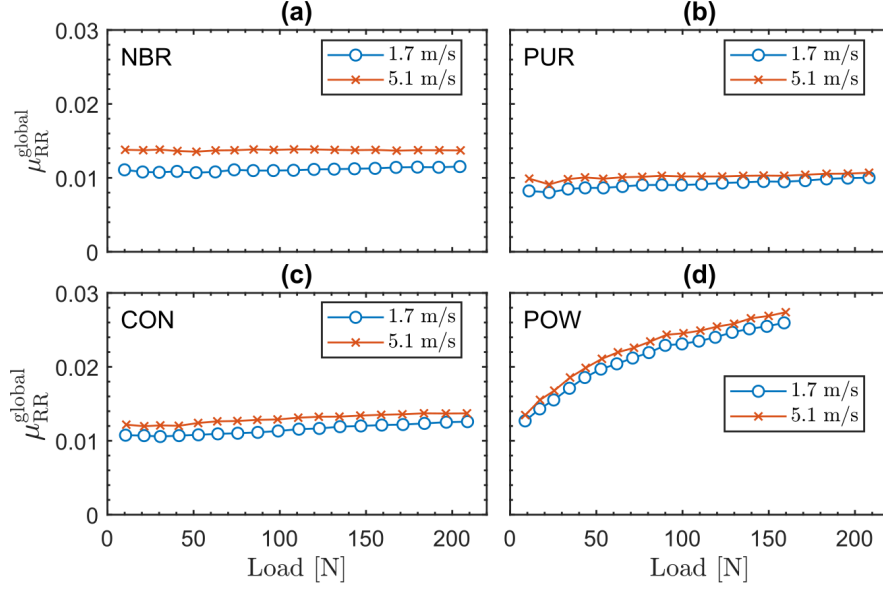


**Figure 7.14:** The constant  $\mu_{RR}^{\text{global}} = C_0 + C_1$  for the fit of  $\mu_{RR}(P_f)$  plotted as a function of load.

Admittedly, this ignores the non-linear dependence of  $\mu_{RR}$  on  $P_f$  predicted by the toy model but is still sufficient to reach a firm conclusion. Because of the load dependence of RR, which is not under investigation here, we subtract from each data point the average RR coefficients of all surfaces with the same wheel, speed and load. This average is denoted  $\langle \mu_{RR} \rangle$ .

Figure 7.16(a) shows  $\mu_{RR} - \langle \mu_{RR} \rangle$  as a function of MPD for the CON wheel data at 1.7 m/s, while Fig. 7.16(b) shows the same quantity as a function of  $P_f$ . We fit a line to each data set using least-squares, which results in a slope which is denoted by  $\hat{\beta}_1$ . Similar plots for the remaining wheel and speed targets are shown in Appendix B.

Although Fig. 7.16(a) and (b) indicate a more systematic dependence in  $\mu_{RR} - \langle \mu_{RR} \rangle$  on  $P_f$  compared to MPD, due to the noise, it is necessary to evaluate the slope uncertainty to determine whether this is statistically significant. By using the standard theory of linear least-squares fits, we calculate the variance of  $\hat{\beta}_1$  for a given data set. Figure 7.16(c) and (d) show the slopes with error bars indicating plus/minus the square root of the slope variance. For MPD, the slope is zero within the uncertainty, indicating no correlation between MPD and  $\mu_{RR}$ . On the other hand,  $\mu_{RR} - \langle \mu_{RR} \rangle$  shows a systematic  $P_f$  dependence, for PUR and CON wheels, for which we showed earlier had a considerably larger variance in the  $\mu_{RR}$  than for the NBR and POW wheels (see Fig. 7.13).

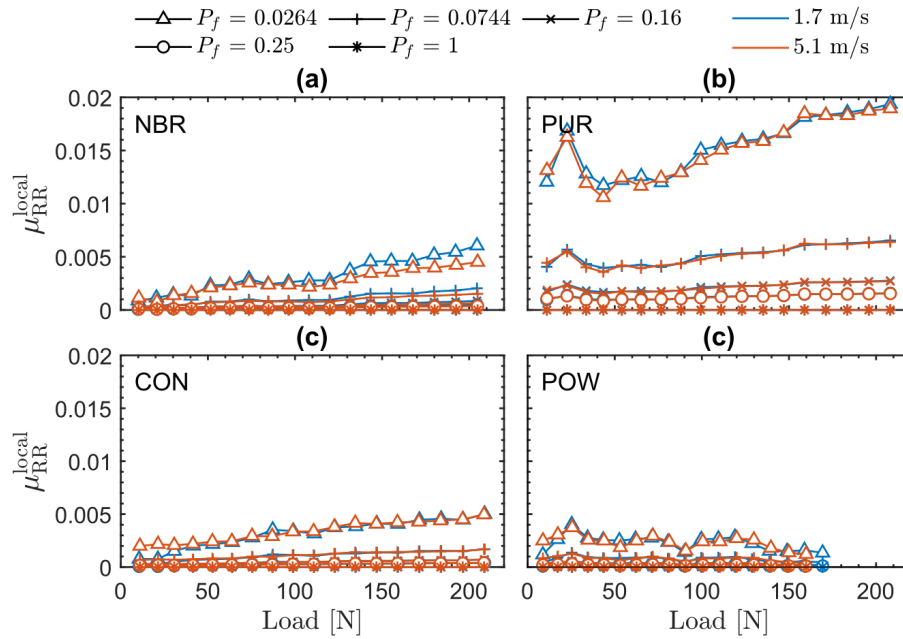


**Figure 7.15:** The constant  $\mu_{RR}^{\text{local}} = C_1(1/P_f - 1)$  for the fit of  $\mu_{RR}(P_f)$  plotted as a function of load.

The simple linear analysis reveals that for a given load  $P_f$  is a better predictor than MPD. Even for the NBR wheel,  $P_f$  is more convincing. Only for the pneumatic POW wheel do we find no clear difference in the ability of the two quantities to predict  $\mu_{RR}$ .

## 7.4 Asymmetry

When planning the different surface textures, a question accrued. Does asymmetric surfaces texture have a different RR if the travelling direction is reversed? This relates to the surface measures SKEW mentioned in Sec. 3.

To test this possibility, a two dimensional surface texture (Tex7) with a asymmetric texture best described as a ramp signal was made (see Sec. 5.6.2 and Tab. 7.1). For this surface texture, one could argue that the direction against the ramp would introduce a faster compression of the wheel material compared to the other direction. From this argument the two directions would give rise to different energy losses in the material, thus having different RR.

From measurements on Ver2 Fig. 7.18 plot  $\mu_{RR}$  as a function of load at the speeds 1.7 and 5.1 m/s, for travelling directions with (forward) and against (backward) the ramp. In the plot, a simple illustration shows the travelling direction of the wheel as an arrow. This is done for the NBR wheel and the

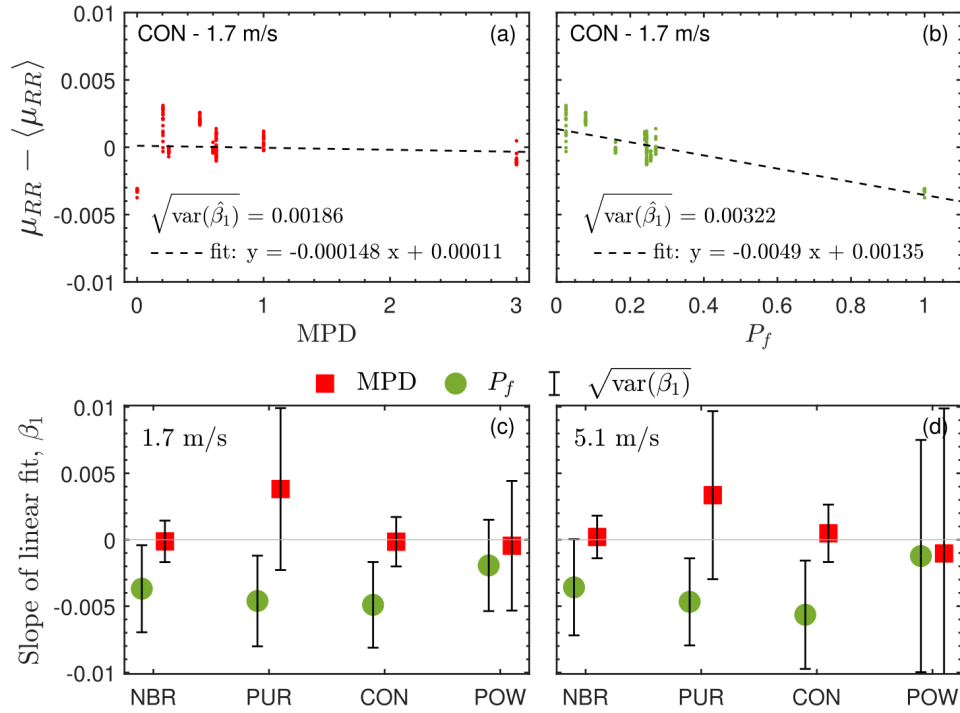


**Figure 7.16:** Slope analysis of the data sets for all loads at 23 °C. (a) and (b) show linear least-squares fits to  $\mu_{RR} - \langle \mu_{RR} \rangle$ , plotted as a function of MPD and  $P_f$  for the CON wheel. (c) and (d) show the slopes obtained plotted with error bars.  $\text{var}(\hat{\beta}_1)$  is the variance of the fitted slope.

POW wheel. For both wheels,  $\mu_{RR}$  is the same for both directions in both directions, and concluding that for this texture there is no change in RR when the travelling direction is reversed.

It is possible that texture with different ramp sizes could introduce a different RR for a reversed travelling direction. Because an attempt with a bigger ramp introduced a lot of shaking and issues with the test rig, while also not being a primary goal, no further test was made on asymmetric textures. However, this test still illustrates how the test rig and 3D printed surfaces may be used to systematically investigate various aspects of RR.

## 7.5 Contribution from Tape and Print - Tex0

By measuring on flat 3D printed surfaces without texture (Tex0), we try to measure the contribution of the double-sided tape. Although the surface was produced to be flat, due to the FDM system, Tex0 has a small textured surface from the 0.1 mm layer. However, as the rest of the textures have more

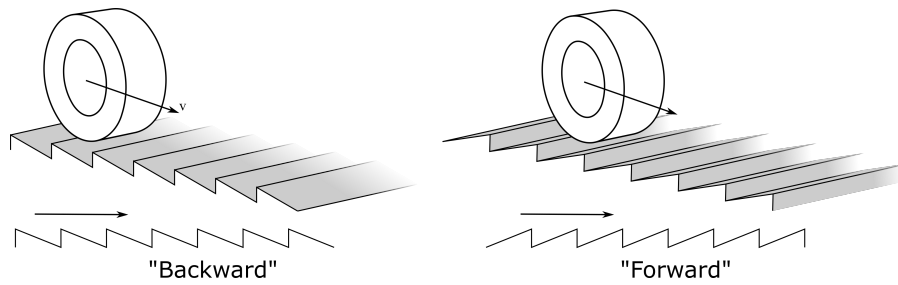


**Figure 7.17:** Illustration of the asymmetric surface texture design and the definition of forward and backward motion.

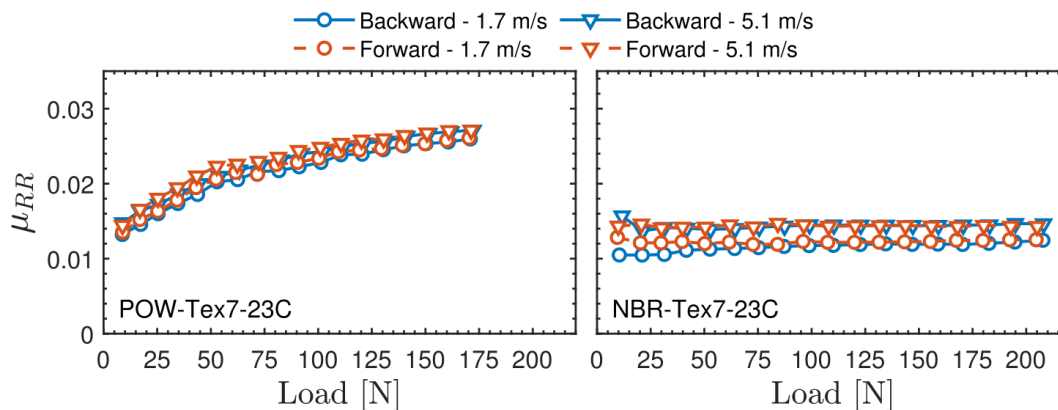


**Figure 7.18:** Rolling resistance coefficient,  $\mu_{RR}$ , as a function of load for the asymmetric surface (Tex7), using test wheel POW and NBR.

prominent textures, Tex0 is more or less flat.

Figure 7.19 shows  $\mu_{RR}$  as a function of load for Ver2 at two speeds using the NBR wheel on four surface textures: Steel, Tex0, Tex6 and Tex9. For both speeds, the result indicates a clear contribution from the tape, at loads below 100 N, especially for speeds at 1.7 m/s, where it completely makes up the difference between steel and Tex9 measurements. As the load increases the contribution from the tape seems to decrease, to the point where Tex0 measurements are identical with at of steel. Purposefully, only measurements for Tex6 and Tex9 are shown, as the rest of the textures measurements are in between Tex6 and Tex9.

From these results, we can conclude that the double-sided tape has an effect on the RR measurements, but is of lesser importance at higher loads and speed. For reliable measurements using double-sided tape and 3D printed parts only measurements above 100 N and at higher speeds should be considered. This also promotes the difficulty of RR measurements at low loads, in addition to the repeatability measurements (see Fig. 7.1).

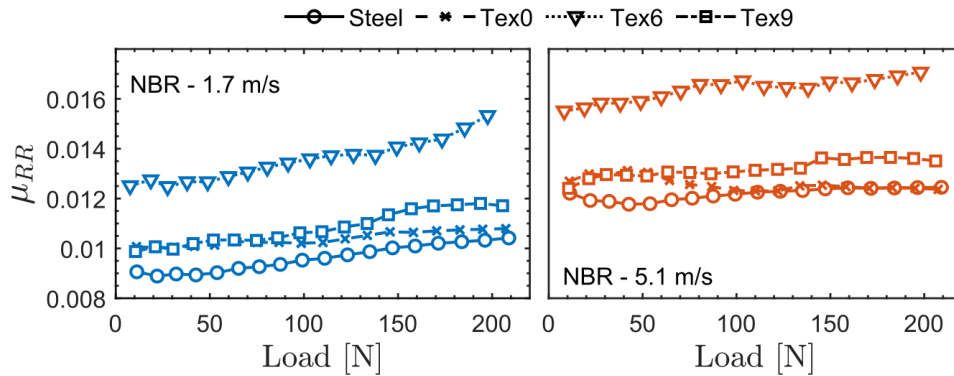


**Figure 7.19:** Rolling resistance Coefficient,  $\mu_{RR}$ , as a function of load using NBR wheel on textures Steel, Tex0, Tex6 and Tex9. Difference from Tex0 showcases the contribution from the double-sided tape.

## 7.6 Contact Patch Experiment

In Fig. 7.20-7.21 measurements of the contact patch using pressure-sensitive sheets is shown for POW wheel at different tyre pressures and loads, on a flat surface and a curved surface. All the performed contact patch measurements are shown in Fig. 7.22(a) as a function of load.

To evaluate at what existence the curved surface, i.e test rig steel drum surface, influences RR compared to a usually flat rolling surface, a parametric plot for contact patch sizes (CP) for measurements on curved and flat surfaces is shown in Fig. 7.22(b). The dashed line in the plot indicates where the two parameters are equally sized. The plots show that contact patches for most cases are larger at the curved surface, indicated by the plots being above the dashed line, but still being fairly equal, shown by the overall tendencies of the lines. From the amount of data, it is not possible to conclude if only a constant or proportional dependency is present between the two contact patches. This result indicates that measurements on curved surfaces are a good approximation to measurements on flat surfaces.

In an attempt to observe a direct relation is between RR coefficient and CP, a linear interpolation was done on the experimental data in Fig. 7.22(a) and data from Veldt (2020) shown in Fig. 6.1.

By using linear interpolation on the experimental data tyre pressure is plotted as a function of load in Fig. 7.3. For RR measurements by Veldt (2020) the data point corresponds to  $\mu_{RR}$  measurements at 0.008, 0.01 and 0.012 for speeds at 2.1 m/s. For better comparison with the static contact patch measurements, data from Veldt (2020) with the lowest speeds were chosen. For patch measurements on curved surfaces data points is plotted for sizes of

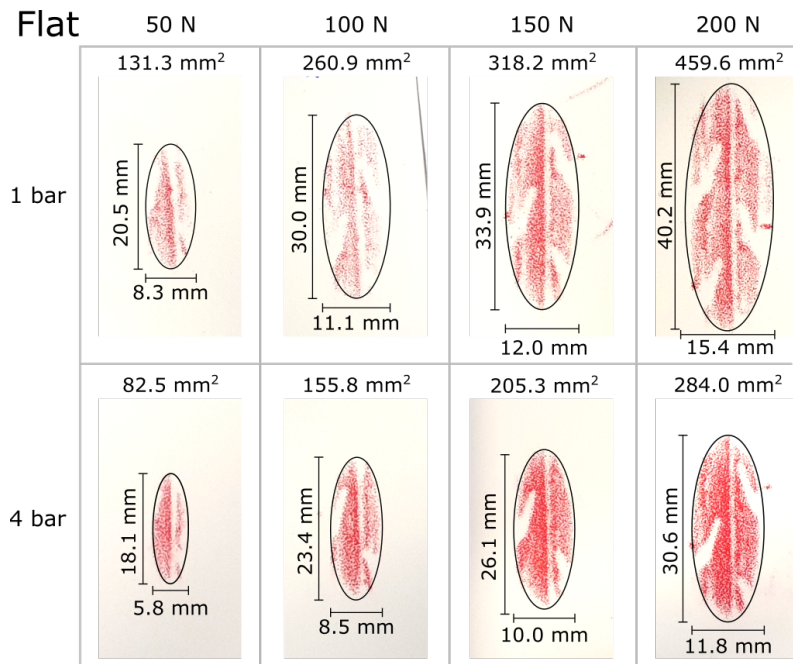


**Figure 7.20:** Contact patch between pneumatic tyre (POW) and a flat steel surfaces at different tyre pressures and loads.

150mm<sup>2</sup>, 200mm<sup>2</sup> and 250mm<sup>2</sup>. Results are questionable due to the uncertainties from the pressure-sensitive paper, and the evaluating by eye.

From the plot, no direct relation between the RR coefficient and the contact patch is observed. However, as  $\mu_{RR}$  or the contact patch size is increased, the lines moves towards a higher load for a specific tyres pressure. This may indicate a increasing  $\mu_{RR}$  for larger contact patches. Interestingly, from the toy model (Chap. 4) we would expect the opposite relation between  $\mu_{RR}$  and contact patch size. The results suggests that more thorough investigation and tests is needed, as the observed relation may be due to some unidentified connection between the load, pressure and POW wheel. No further conclusion is made in this thesis.

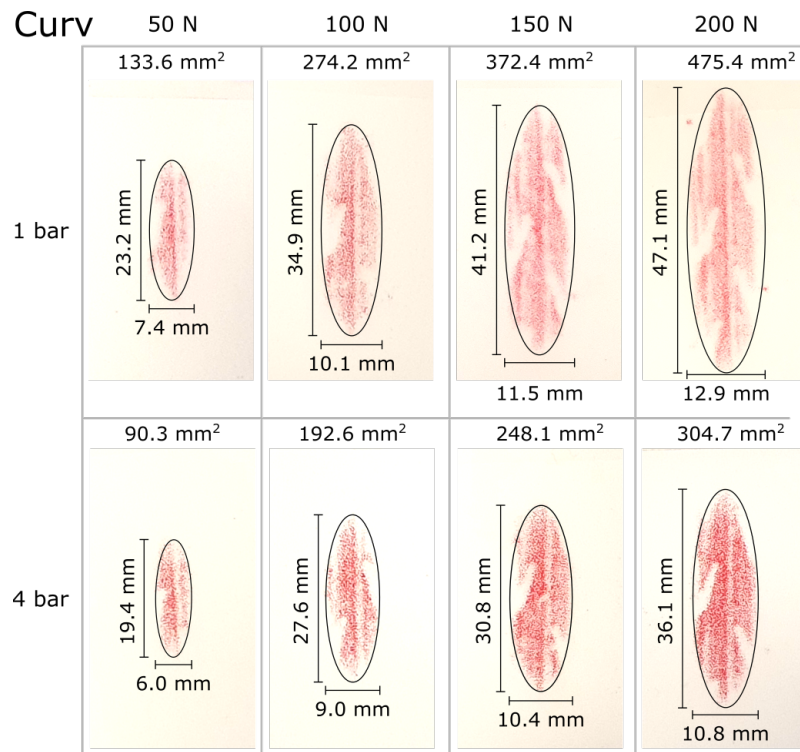


**Figure 7.21:** Contact patch between pneumatic tyre (POW) and the curved drum surfaces at different tyre pressures and loads.

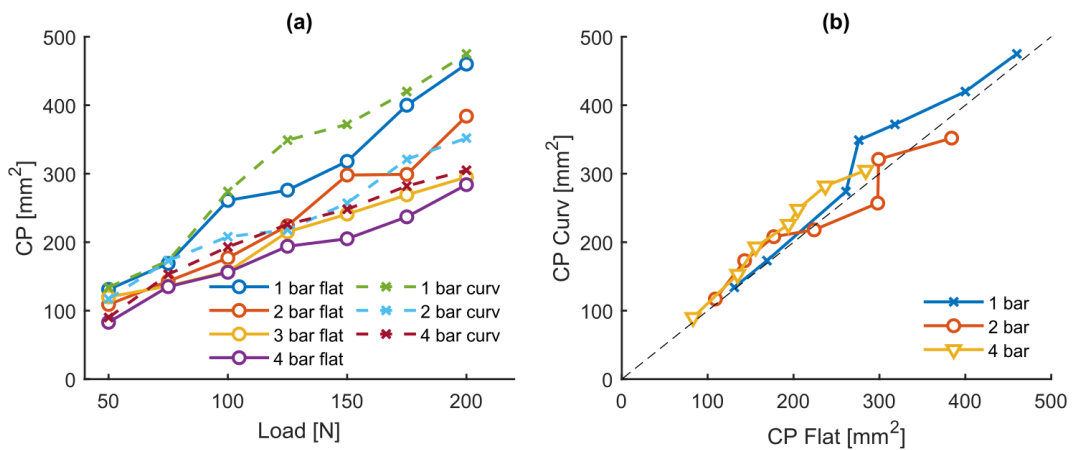


**Figure 7.22:** (a) Contact patch, CP, on the drum surface and a flat surface, plotted as a function of load for different tyre pressures. (b) Parametric plot showing the relation between CP for flat and curved surface, at different tyre pressures.

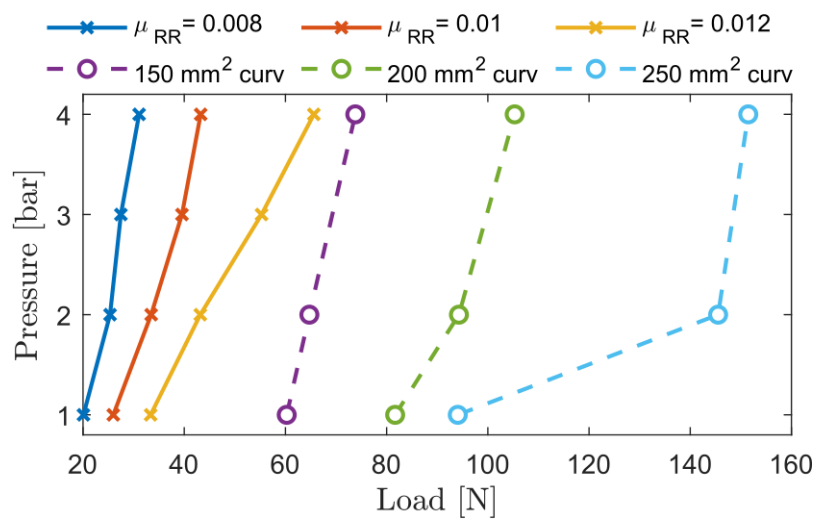


**Figure 7.23:** Pressure as a function of load and speeds, given a rolling resistance coefficient and size of contact patch.

## 8 Summary

As the primary goal in this thesis, we have developed a new small idealised drum test rig capable of measuring rolling resistance (RR). The new test rig is an improved version of the test rig presented in Hansen and Larsen (2017), and consist of a 538 mm internal drum. Noteworthy improvements for the new test rig consist of: Temperature control of the entire test rig, lower drum deviation, reduced wear and tear, and an improved measuring protocol to reduce measuring time. Tests of the new test rig indicate good repeatability for loads above 100 N.

Both test rigs have been used throughout the thesis, denoted “Version 1” (Ver1) and “Version 2” (Ver2), to measure RR at a range of different loads and speeds, using four different wheels. The wheels consist of three solid wheels and a single pneumatic wheel, with sizes from 114 mm to 150 mm in diameter. The measurements showed that an increase in speed corresponds to an increase in the RR coefficient, while, depending on the wheel used, there is either no change or an increase in the RR coefficient for increasing loads. This is consistent with measurements from previous studies.

By using different surface textures on the two test rigs, we were able to investigate the influence of surface texture on RR. The surface textures consist of sandpapers with five different grit sizes (P400, P160, P60, P32 and P24) and 10 different textures with geometric patterns, made by an FDM 3D printer using Polylactic Acid (PLA) material. To securely attach the textures to the drum, we used double-sided tape. Later tests for a flat 3D printed surface revealed that the tape contributes to the measured RR, but is of lesser importance at higher speeds and loads above 100 N.

The use of 3D printed surfaces shows great potential, as we can measure RR on highly controllable textures. A good example is the asymmetric (ramp) texture, which indicates that skewness does not have an effect on RR. However, as this was only tested for a single surface texture, further research might be needed. In this thesis, we have focused mainly on the size and distribution of peaks. Here we conclude that larger surface textures give rise to a higher RR for both sandpaper and 3D printed surface textures. This is consistent with previous studies.

In this thesis, we have presented a new toy model, based on the proportionality between stored energy and lost energy. The model is calculated from the behaviour of springs and predicts that energy loss, i.e. RR, is inversely

proportional to the number of springs, which is proportional to the peak fraction.

Based on the measured RR coefficients of different surfaces and wheels, at a range of loads and speeds, we tested MPD and peak fraction as a predictor for RR. For the sandpaper measurements, only MPD was tested, showing no clear correlation with the RR coefficient. For the 3D printed surfaces, a more detailed analysis was made to evaluate MPD and peak fraction as predictors. This analysis reveals no correlation between the RR coefficient and MPD, while peak fraction, to some extent, can predict the RR coefficient.

Contact patch measurements were made with the hope of a possible relation between the RR coefficient and the contact patch. The results only hint at a relation, but are not enough for a proper conclusion.

## Suggestions for Future Research

In this thesis, we have made a lot of measurements using the new test rig and 3D printed surface textures. However, by using 3D printed surface textures, the test rig is capable of much more. Listed below are a few suggestions for future research using the new test rig, as well as some improvements if similar measurements are to be done:

**Texture attachment** For attaching texture to the drum, the double-sided tape contributed to the RR. Instead of using tape, we suggest using a mechanical solution to fix the textures inside of the drum, so no compressible material is under the texture where the wheel is rolling.

**Staggered texture design** Vibration when the wheel is rolling on the textures, contributes to the RR. By redesigning the textures from an array design (see Fig. 8.1(a)) to a staggered design (see Fig. 8.1(b)), the amount of global vibration can be reduced.

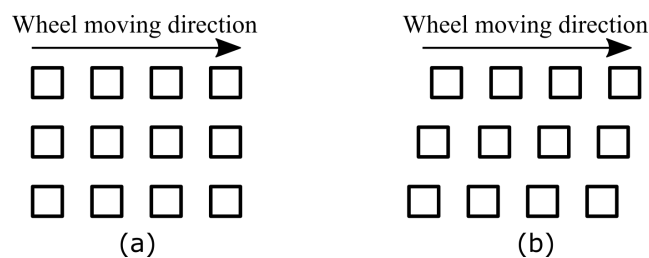


**Figure 8.1:** Illustration of (a) Texture in a regular square array and (b) staggered texture design.

**Other geometric patterns** The texture designs presented in this thesis were chosen to be simple textures while also being textures for which it is easy to calculate the MPD and peak fraction. However, because of 3D printing, it is possible to test almost every imaginable surface texture. This could for instance be the geometrical patterns presented by Parry (1998), or scans of real pavement textures.

# Bibliography

- Andersen, L. G. (2015). *Rolling Resistance Modelling: From Functional Data Analysis to Asset Management System*. phdthesis, Roskilde University, Roskilde, Denmark.
- Anfosso-Lédée, F., Cerezo, V., Karlsson, R., Bergiers, A., Dauvergne, S., Ejsmont, J., Goubert, L., Lesdos, H., Maeck, J., Sandberg, U., Sjogren, L., and Zöller, M. (2016). Experimental validation of the rolling resistance measurement method including updated draft standard. resreport, IFSTTAR. ROSANNE Deliverable D3.6.
- Araújo, J. P. C., Palha, C. A., Martins, F. F., Silva, H. M., and Oliveira, J. R. (2019). Estimation of energy consumption on the tire-pavement interaction for asphalt mixtures with different surface properties using data mining techniques. *Transportation Research Part D: Transport and Environment*, 67:421–432.
- ASTM E1845 - 09 (2009). Standard practice for calculating pavement macrotexture meanprofile depth. Standard, American Society for Testing and Materials (ASTM).
- Bazi, G., Hajj, E. Y., Ulloa-Calderon, A., and Ullidtz, P. (2018). Finite element modelling of the rolling resistance due to pavement deformation. *International Journal of Pavement Engineering*, 21(3):365–375.
- Bergiers, A., Goubert, L., Anfosso-Lédée, F., Dujardin, N., Ejsmont, J. A., Sandberg, U., and Zöller, M. (2011). Comparison of rolling resistance measuring equipment - pilot study. resreport, VTI. MIRIAM, SP1 Deliverable No. 3.
- Brinson, H. F. and Brinson, L. C. (2015). *Polymer Engineering Science and Viscoelasticity*. Springer-Verlag GmbH.
- Cesbron, J. and Yin, H.-P. (2010). Contact analysis of road aggregate with friction using a direct numerical method. *Wear*, 268(5):686–692.
- Clapp, T. G., Eberhardt, A. C., and Kelley, C. T. (1988). Development and validation of a method for approximating road surface texture-induced contact pressure in tire-pavement interaction. *Tire Science and Technology*, 16(1):2–17.
- Clark, S. (1976). Rolling resistance forces in pneumatic tires. techreport DOT-TSC76-1, U.S. Department of Transportation.

- Clark, S. K. and Dodge, R. N. (1979). *A handbook for the rolling resistance of pneumatic tires*. Industrial Development Division, Institute of Science and Technology.
- Dressel, A. and Sadauckas, J. (2020). Characterization and modelling of various sized mountain bike tires and the effects of tire tread knobs and inflation pressure. *Applied Sciences*, 10(9):3156.
- Dressel, A. E. (2013). *Measuring and Modeling the Mechanical Properties of Bicycle Tires*. phdthesis, University of Wisconsin-Milwaukee.
- EEA (2021). Annual european union greenhouse gas inventory 1990–2019 and inventory report 2021. techreport, European Environment Agency.
- Ejsmont, J. and Owczarzak, W. (2019). Engineering method of tire rolling resistance evaluation. *Measurement*, 145:144–149.
- Ejsmont, J. and Sommer, S. (2021). Selected aspects of pavement texture influence on tire rolling resistance. *Coatings*, 11(7):776.
- Ejsmont, J., Taryma, S., Ronowski, G., and Swieczko-Zurek, B. (2016). Influence of load and inflation pressure on the tyre rolling resistance. *International Journal of Automotive Technology*, 17(2):237–244.
- Ejsmont, J., Taryma, S., Ronowski, G., and Swieczko-Zurek, B. (2018). Influence of temperature on the tyre rolling resistance. *International Journal of Automotive Technology*, 19(1):45–54.
- Ejsmont, J. A., Ronowski, G., Świczko Żurek, B., and Sommer, S. (2017). Road texture influence on tyre rolling resistance. *Road Materials and Pavement Design*, 18(1):181–198.
- El-Zomor, H. M. (2019). Real-time estimation of pneumatic tyre hysteresis loss. *International Journal of Heavy Vehicle Systems*, 26(2):175–187.
- EPA (2021). U.s. greenhouse gas emission and sinks 1990-2019. techreport, United States Environmental Protection Agency.
- Ferry, J. D. (1980). *Viscoelastic Properties*. John Wiley & Sons, 3 edition.
- Flügge, W. (1975). *Viscoelasticity*. Springer-Verlag, Berlin New York.
- Fong, S. (1998). Tyre noise predictions from computed road surface texture induced contact pressure. In *Proceedings of INTER-NOISE 1998*, Christchurch, New Zealand.
- Gottaut, C. and Goubert, L. (2016). Texture-based descriptors for road surface properties and how they can be used in the appropriate standards. resreport, Austrian Institute of Technology. ROSANNE Deliverable D4.2.
- Goubert, L., Do, M. T., Bergiers, A., Karlsson, R., and Sandberg, U. (2014).

- State-of-the-art concerning texture influence on skid resistance, noise emission and rolling resistance. resreport, Austrian Institute of Technology. ROS-ANNE Deliverable D4.1.
- Goubert, L. and Sandberg, U. (2018). Enveloping texture profiles for better modelling of the rolling resistance and acoustic qualities of road pavements. In *8th Symposium on Pavement Surface Characteristics: SURF 2018 – Vehicle to Road Connectivity*, pages 1–12, Brisbane, Queensland, Australia. Australian Road Research Board (ARRB).
- Gould, P. L. and Feng, Y. (2018). *Introduction to Linear Elasticity*. Springer International Publishing.
- Grappe, F., Candau, R., Barbier, B., Hoffman, M. D., Belli, A., and Rouillon, J.-D. (1999). Influence of tyre pressure and vertical load on coefficient of rolling resistance and simulated cycling performance. *Ergonomics*, 42(10):1361–1371.
- Hall, J., Smith, K., Titus-Glover, L., Wambold, J., Yager, T., and Rado, Z. (2009). *Guide for Pavement Friction*. Number 108 in NCHRP WebDocuments. The National Academies Press, Washington, DC.
- Hansen, L. S. and Larsen, M. L. (2017). *An experimental investigation of rolling resistance*. mathesis, Roskilde University, Roskilde, Denmark.
- Heinz, M. and Grosch, K. A. (2007). A laboratory method to comprehensively evaluate abrasion, traction and rolling resistance of tire tread compounds. *Rubber Chemistry and Technology*, 80(4):580–607.
- Holt, W. L. and Wormeley, P. L. (1922). Power losses in automobile tires. In *Technologic Papers of the Bureau of Standards*, volume 213. National Bureau of Standards.
- ISO (1997). Characterization of pavement texture by use of surface profiles - part 1: Determination of mean profile depth. Standard 13473-1:1997, International Organization for Standardization.
- ISO (2005). Passenger car, truck, bus and motorcycle tyres — methods of measuring rolling resistance. Standard 18164:2005, International Organization for Standardization.
- ISO (2018). Passenger car, truck and bus tyre rolling resistance measurement method — single point test and correlation of measurement results. Standard 28580:2018, International Organization for Standardization.
- ISO (2019). Characterization of pavement texture by use of surface profiles - part 1: Determination of mean profile depth. Standard 13473-1:2019, International Organization for Standardization.

- Karlsson, R., Hammarström, U., Sörensen, H., and Eriksson, O. (2011). Road surface influence on rolling resistance. coastdown measurements for a car and an hgv. Technical Report VTI notat 24A-2011, Swedish National Road and Transport Research Institute (VTI).
- Klein, P. and Hamet, J.-F. (2004). Road texture and rolling noise: an envelopment procedure for tire-road contact. Rapport de recherche.
- Lakes, R. (2009). *Viscoelastic Materials*. Cambridge University Press.
- Larsen, M. L., Cesbron, J. J., Lédée, F. A., Ropert, C., Dyre, J. C., and Hecksher, T. (2021). Laboratory for the validation of rolling-resistance models. *International Journal of Applied Mechanics*, 13(10):2150116.
- Luchini, J. R. (1982). Test surface curvature reduction factor for truck tire rolling resistance. In *SAE Technical Paper Series*. SAE International.
- Mashadi, B., Ebrahimi-Nejad, S., and Abbaspour, M. (2019). A rolling resistance estimate using nonlinear finite element numerical analysis of a full three-dimensional tyre model. *Proceedings of the Institution of Mechanical Engineers Part D-journal of Automobile Engineering*, 233(1):147–160.
- Michelin (2003). The tyre: Rolling resistance and fuel savings. Société de Technologie Michelin.
- Nakajima, Y. (2019). Rolling resistance of tires. In *Advanced Tire Mechanics*, pages 931–1017. Springer Singapore.
- Nielsen, N. R., Chatti, K., Nielsen, C. P., Zaabar, I., Hjorth, P. G., and Hecksher, T. (2020). Method for direct measurement of structural rolling resistance for heavy vehicles. *Transportation Research Record*, 2674(5):371–380.
- Parry, A. R. (1998). Macrottexture and road safety: Final report. resreport 1, TRL, Crowthorne, U.K. Project Report PR/CE/56/98 CO67L/94.
- Pettinari, M., Nielsen, E., and Schmidt, B. (2017). Alternative laboratory characterization of low rolling resistance asphalt mixtures. In *Airfield and Highway Pavements*. American Society of Civil Engineers.
- Pexa, M., Mader, D., Cedik, J., Peterka, B., Mueller, M., Valasek, P., and Hloch, S. (2020). Experimental verification of small diameter rollers utilization in construction of roller test stand in evaluation of energy loss due to rolling resistance. *Measurement*, 152.
- Riahi, E., Ropert, C., and Do, M.-T. (2020). Developing a laboratory test method for rolling resistance characterisation of road surface texture. *Surface Topography: Metrology and Properties*, 8(2):024006.
- Sandberg, U. (1990). Road macro- and megatexture influence on fuel consump-

- tion. In Meyer, W. E. and Reichert, J., editors, *Surface Characteristics of Roadways: International Research and Technologies STP 1031*, pages 460–479. American Society for Testing and Materials.
- Sandberg, U., Bergiers, A., Ejsmont, J. A., Goubert, L., Karlsson, R., and Zöller, M. (2011a). Road surface influence on tyre/road rolling resistance. resreport, VTI. MIRIAM, SP1 Deliverable No. 4.
- Sandberg, U., Goubert, L., and Vieira, T. (2018). New measures for characterization of negative surface textures. In *8th Symposium on Pavement Surface Characteristics: SURF 2018 – Vehicle to Road Connectivity*, Brisbane, Queensland. Symposium on Pavement Surface Characteristics (SURF)., Australian Road Research Board (ARRB).
- Sandberg, U., Haider, M., Conter, M., Goubert, L., Bergiers, A., Glaeser, K.-P., Schwalbe, G., Zöller, M., Boujard, O., Hammarström, U., Karlsson, R., Ejsmont, J. A., Wang, T., and Harvey, J. (2011b). Rolling resistance – basic information and state-of-the-art on measurement methods. resreport, VTI. MIRIAM, SP1 Deliverable No. 1.
- Sayers, M. W. (1989). Two quarter-car models for defining road roughness: Iri and hri. *Transportation Research Record*, (1215):165–172.
- Sina, N., Nasiri, S., and Karkhaneh, V. (2015). Effects of resistive loads and tire inflation pressure on tire power losses and CO<sub>2</sub> emissions in real-world conditions. *Applied Energy*, 157:974–983.
- Sohaney, R. C. and Rasmussen, R. O. (2013). Pavement texture evaluation and relationships to rolling resistance at mnroad. resreport MN/RC 2013-16, Minnesota Department of Transportation, Saint Paul, MN, USA.
- Synak, F. and Kalasova, A. (2020). Assessing the Impact of the Change in the Tire Pressure on the Rolling Resistance and Fuel Consumption. *Advances in Science and Technology-research Journal*, 14(3):100–106.
- Veldt, H. M. (2020). Experimental investigation on rolling resistance of pneumatic tires. resreport, Roskilde University, Roskilde, Denmark.
- Vieira, T., Sandberg, U., and Erlingsson, S. (2019). Negative texture, positive for the environment: effects of horizontal grinding of asphalt pavements. *Road Materials and Pavement Design*, 22(1):1–22.
- Vincent, J. F. V. (1982). *Structural Biomaterials*. Palgrave Macmillan.
- von Meier, A., von Blokland, G. J., and Descornet, G. (1992). The influence of texture and sound absorption on the noise of porous road surfaces. In *Proceedings of the PIARC Second International Symposium on Road Surface Characteristics*, pages p. 7–19.

- Willis, J. R., Robbins, M. M., and Thompson, M. (2015). Effects of pavement properties on vehicular rolling resistance: a literature review. Technical report, National Center for Asphalt Technology, Auburn, AL, USA.
- Yin, H. P., Cesbron, J., and Bui, Q. H. (2015). A new formulation for solving 3-D time dependent rolling contact problems of a rigid body on a viscoelastic half-space. *Mechanics Research Communications*, 64:8–14.
- Zöller, M. (2014). State of the art on rolling resistance measurement devices. techreport, AIT. ROSANNE, Deliverable D3.1.

## A Appendix: Ver2 measurements

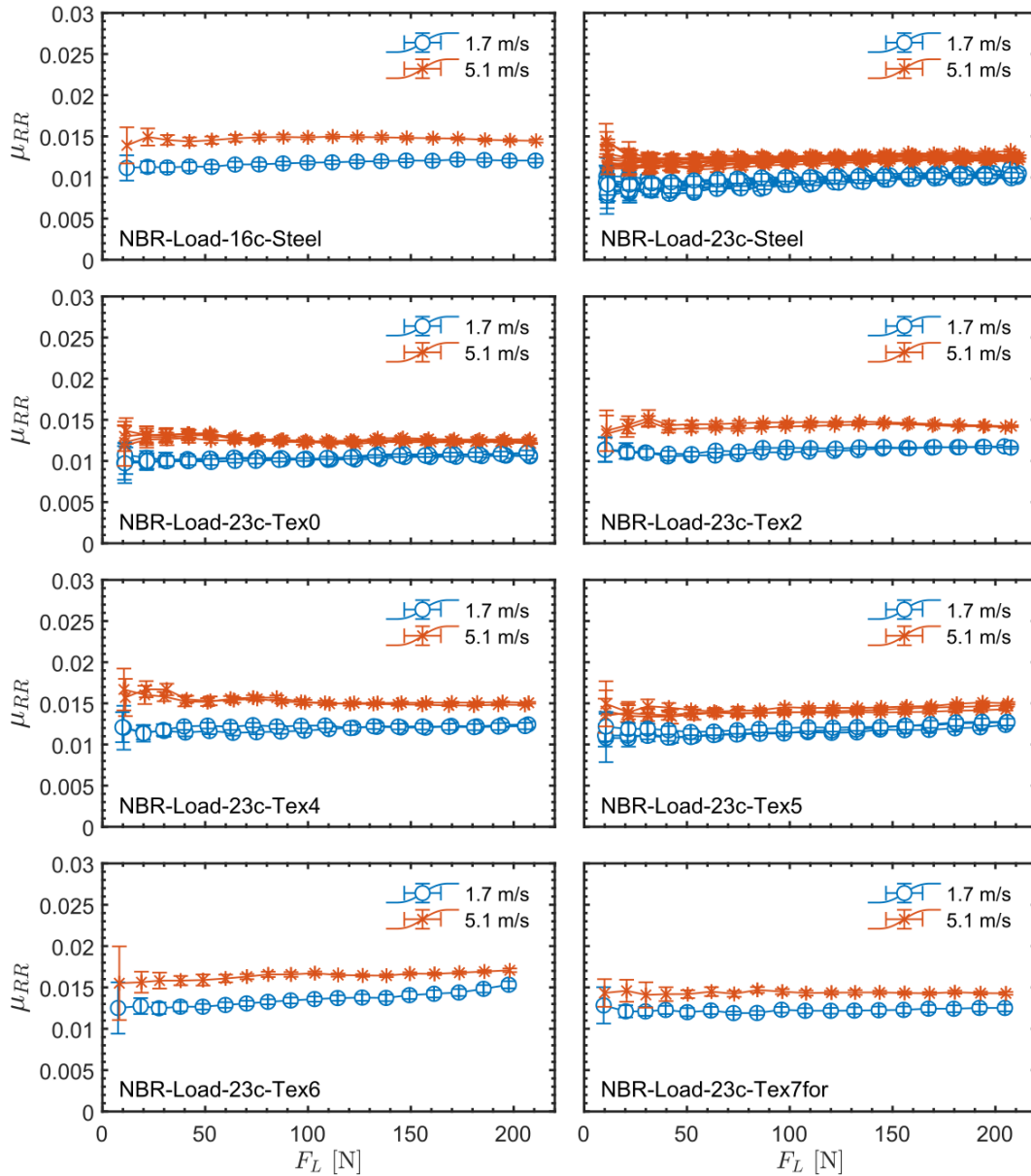


**Figure A.1:** Rolling resistance coefficients  $\mu_{RR}$  as a function of load for test wheels on different surfaces. Error bars indicate standard deviation. Measurements performed using Test Rig Version 2

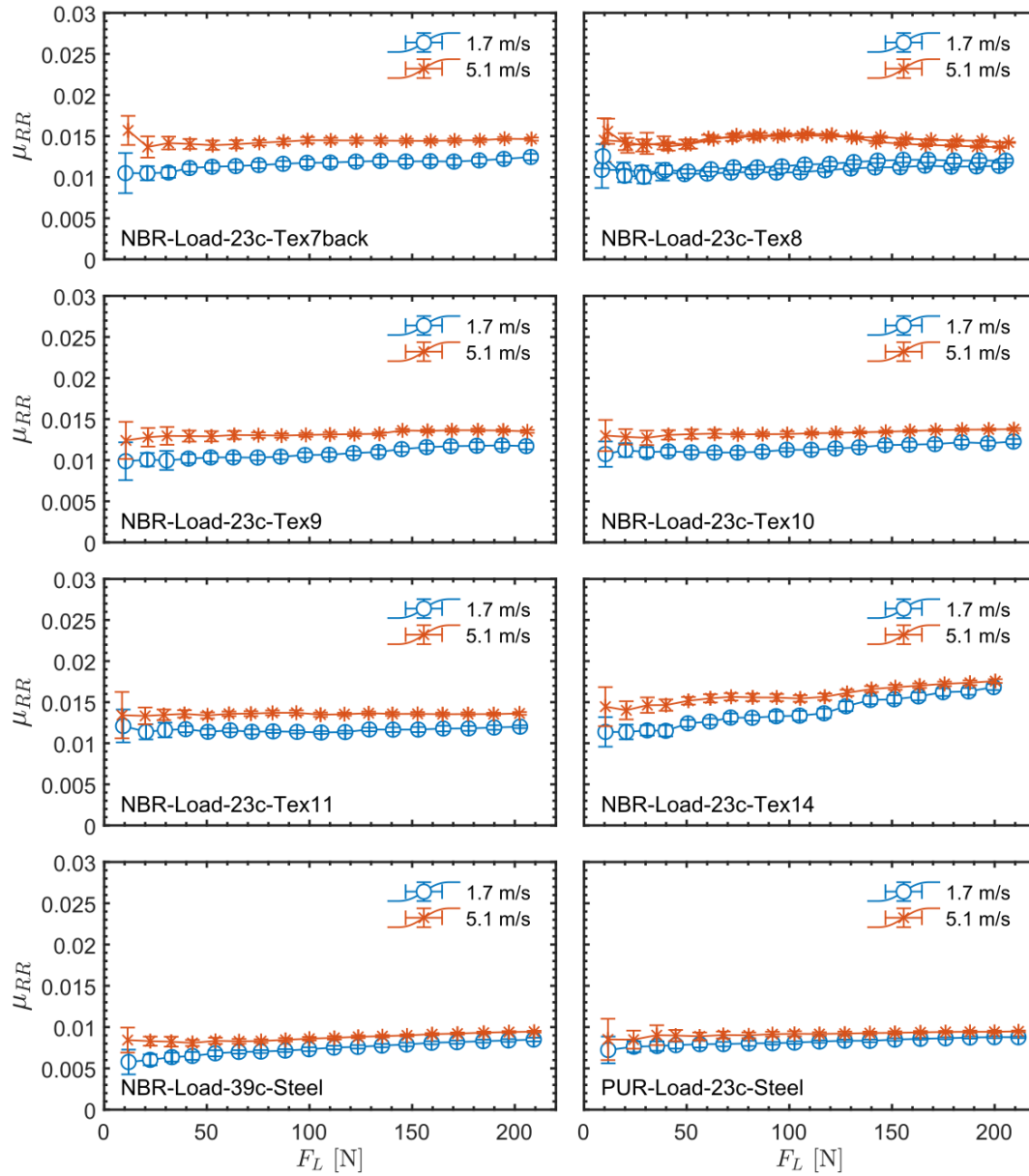


**Figure A.2:** Rolling resistance coefficients  $\mu_{RR}$  as a function of load for test wheels on different surfaces. Error bars indicate standard deviation. Measurements performed using Test Rig Version 2

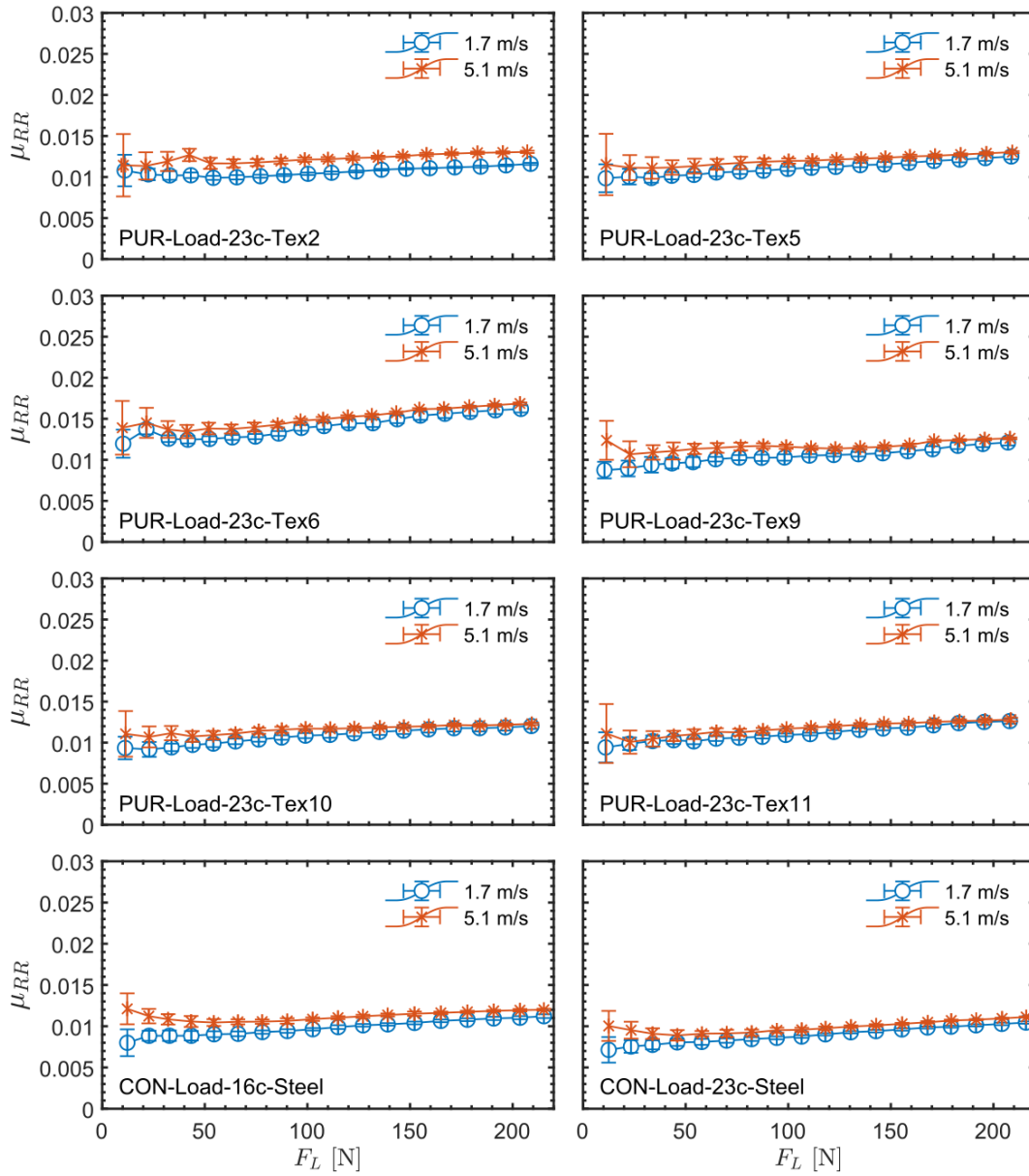


**Figure A.3:** Rolling resistance coefficients  $\mu_{RR}$  as a function of load for test wheels on different surfaces. Error bars indicate standard deviation. Measurements performed using Test Rig Version 2

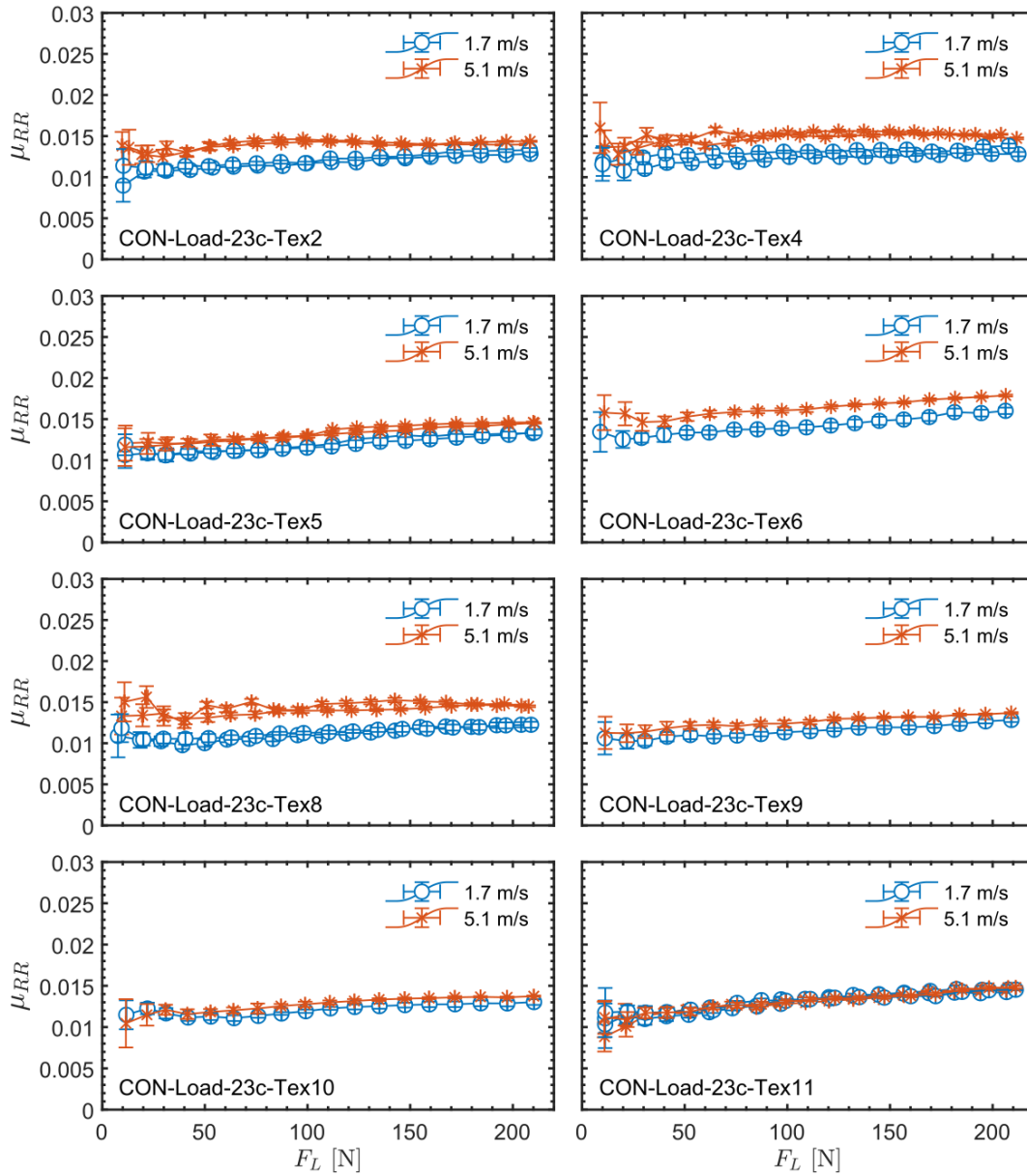


**Figure A.4:** Rolling resistance coefficients  $\mu_{RRR}$  as a function of load for test wheels on different surfaces. Error bars indicate standard deviation. Measurements performed using Test Rig Version 2

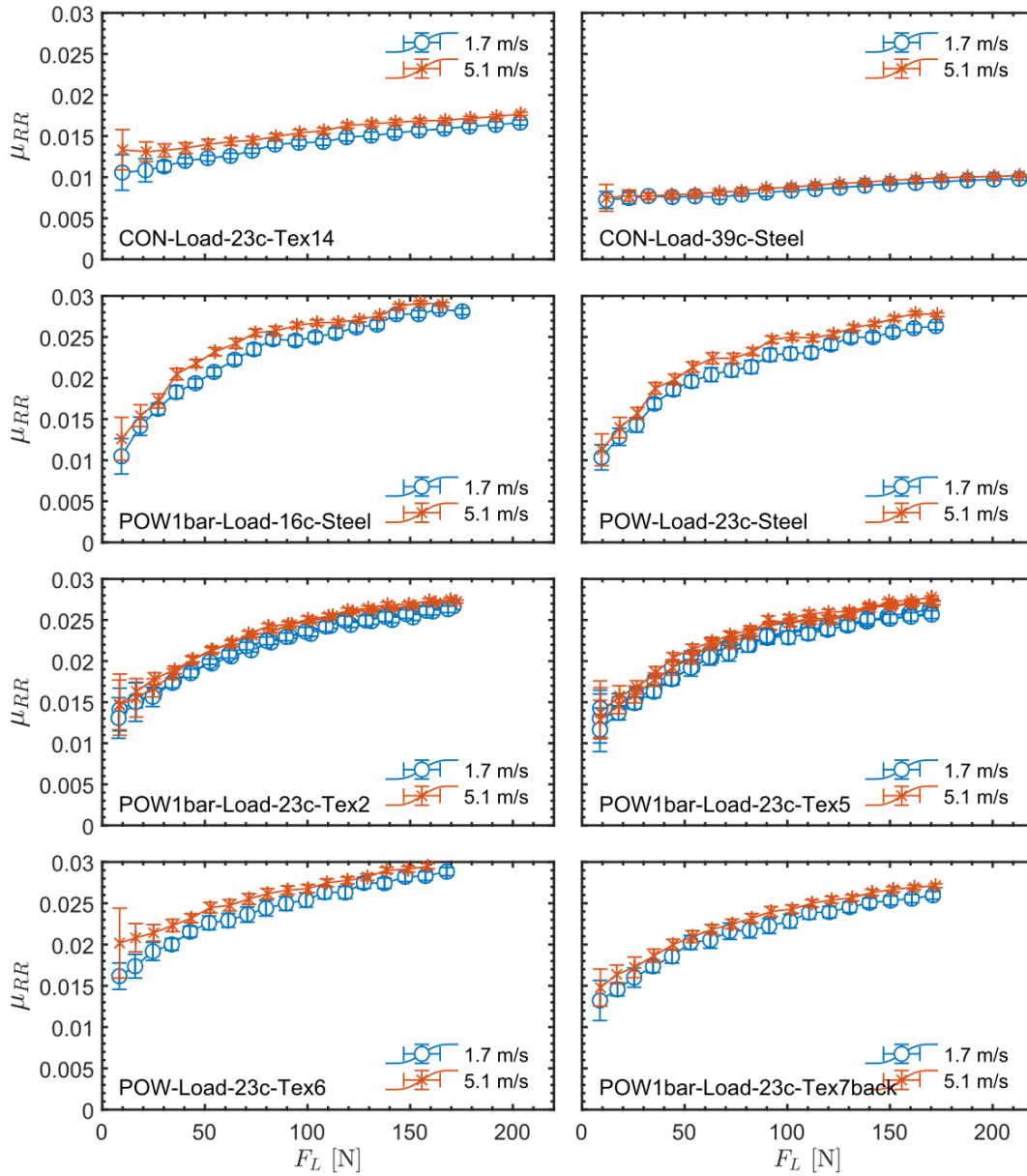


**Figure A.5:** Rolling resistance coefficients  $\mu_{RR}$  as a function of load for test wheels on different surfaces. Error bars indicate standard deviation. Measurements performed using Test Rig Version 2

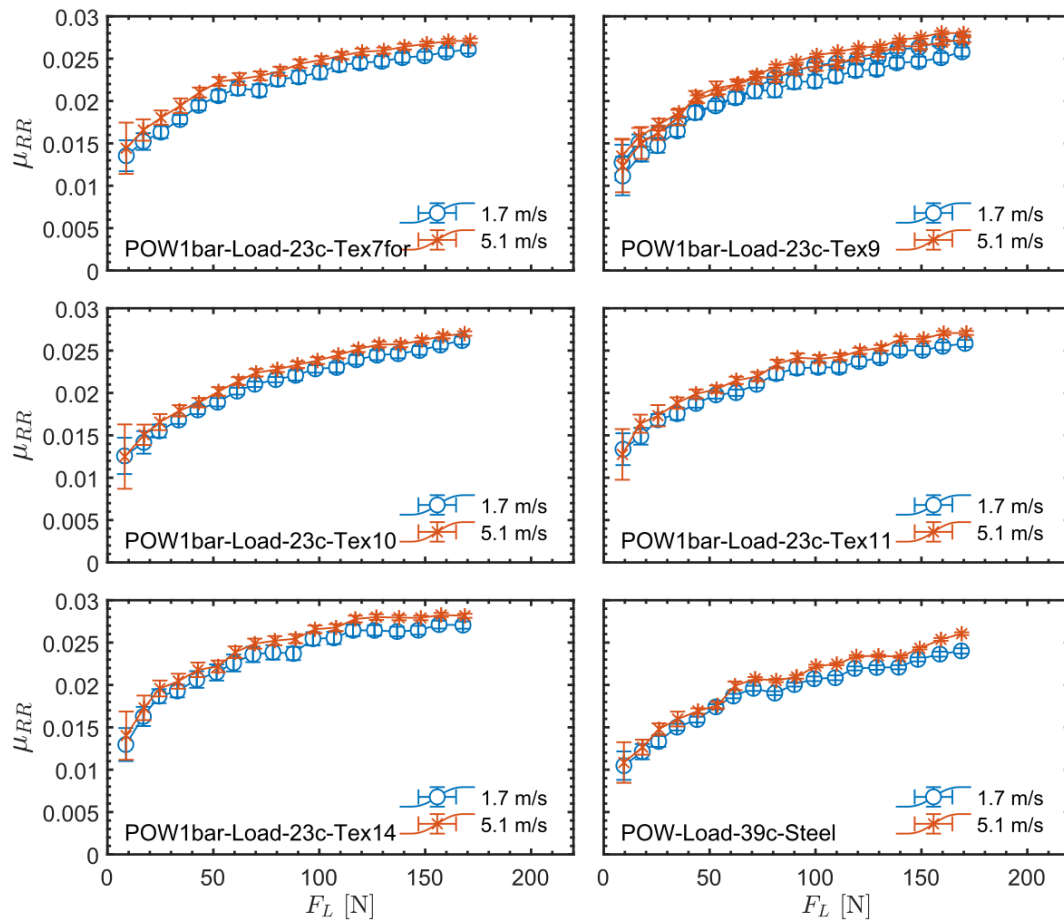


**Figure A.6:** Rolling resistance coefficients  $\mu_{RR}$  as a function of load for test wheels on different surfaces. Error bars indicate standard deviation. Measurements performed using Test Rig Version 2

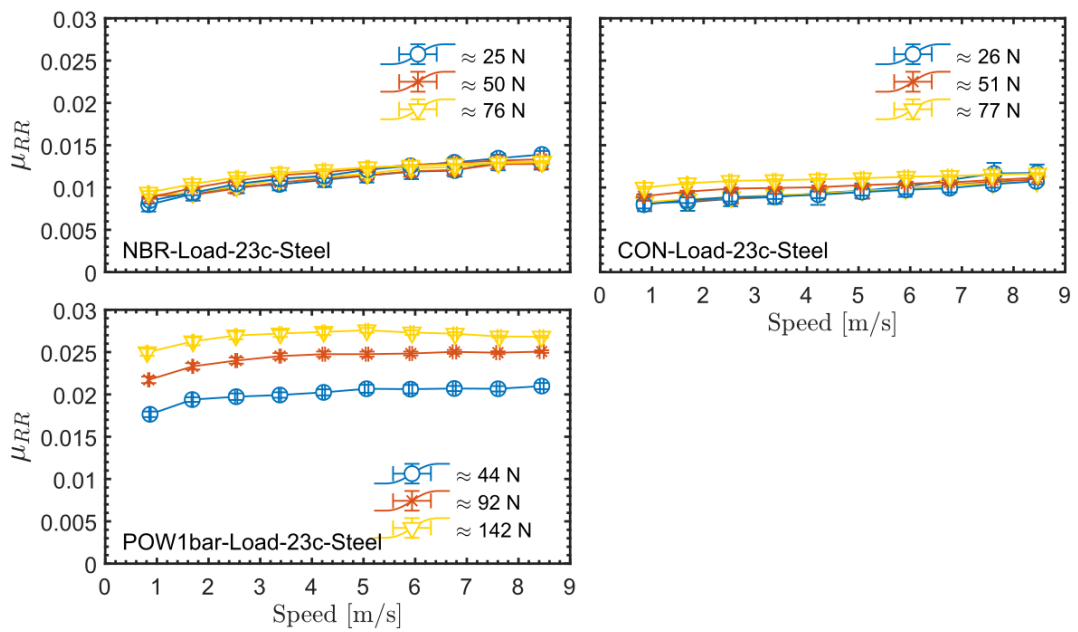


**Figure A.7:** Rolling resistance coefficients  $\mu_{RR}$  as a function of Speed for test wheels on different surfaces. Error bars indicate standard deviation. Measurements performed using Test Rig Version 2

## B Appendix: Slope Analysis

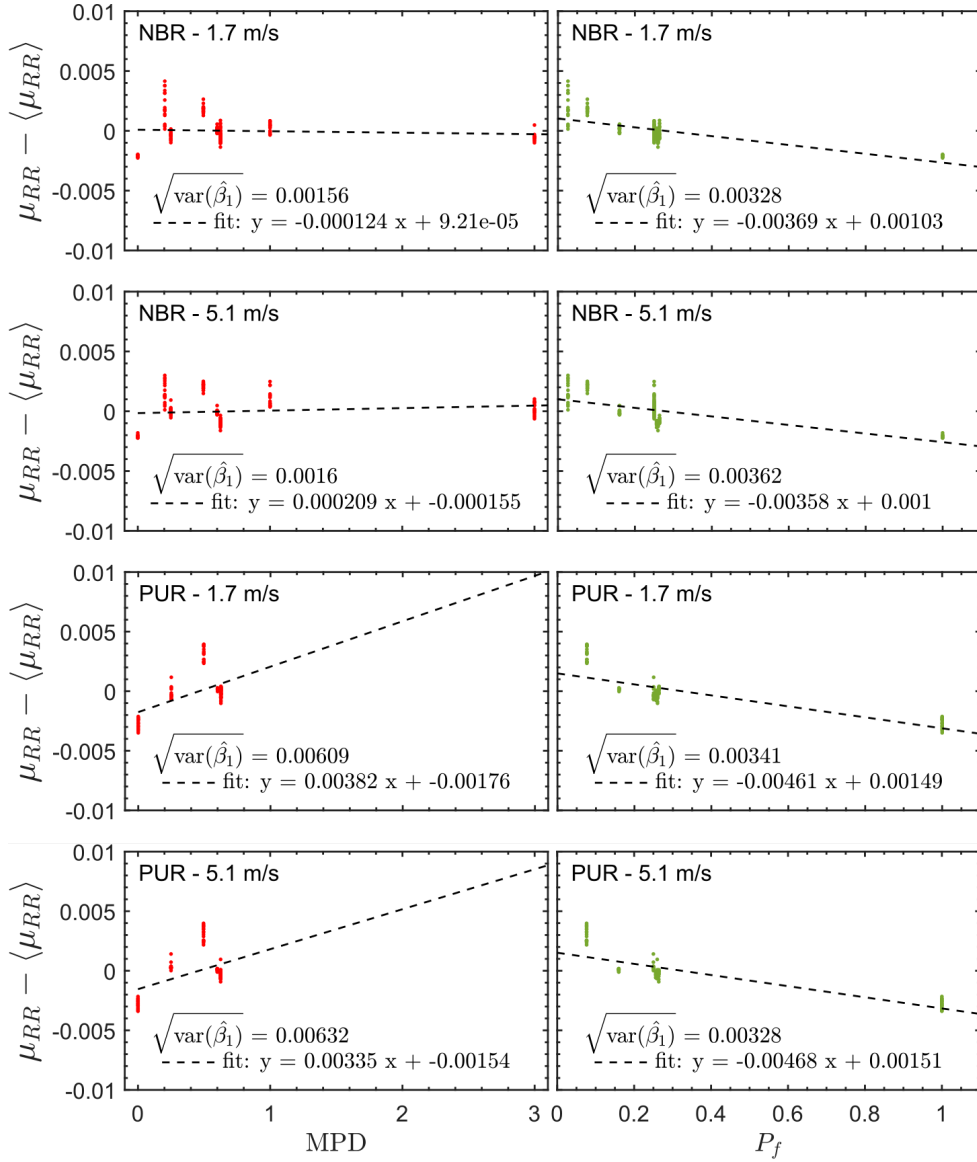


**Figure B.1:** Slope analysis of the data sets for all loads at 23°C. (a) and (b) show for the CON wheel linear least-squares fit to the RR coefficient subtracted its average over the same load over all surfaces studied, plotted as a function of  $P_f$  and MPD.

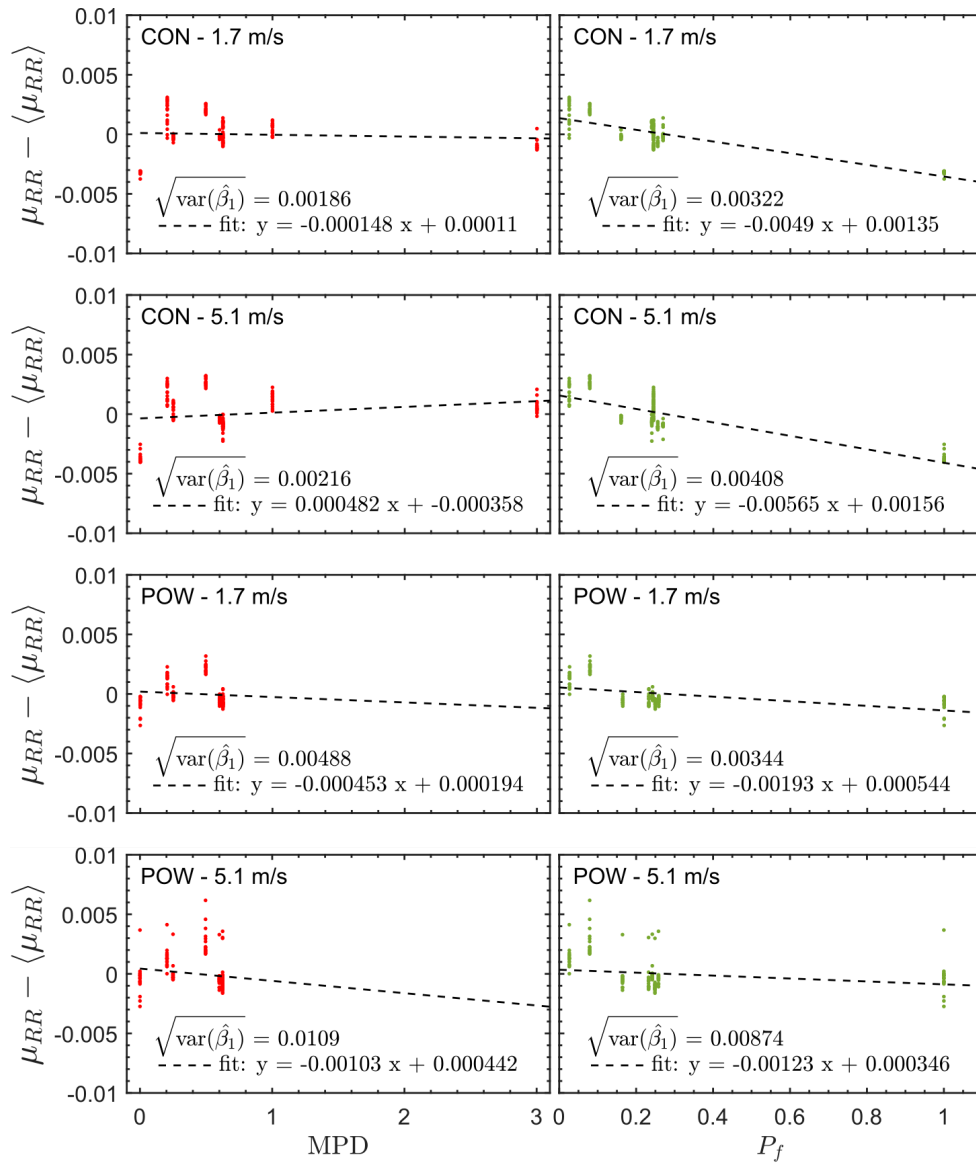


**Figure B.2:** Slope analysis of the data sets for all loads at 23°C. (a) and (b) show for the CON wheel linear least-squares fit to the RR coefficient subtracted its average over the same load over all surfaces studied, plotted as a function of  $P_f$  and MPD.

## **C Appendix: Articles**

### **C.1 Laboratory for Validation of Rolling-Resistance Models**

Published in International Journal of Applied Mechanics, Vol. 13, No. 10 (2021), 2150116 (26 pages), DOI: 10.1142/S1758825121501167

Attached is the unedited version accepted by the journal.

**Laboratory for Validation of Rolling-Resistance Models**M. L. Larsen<sup>†</sup>, J. Cesbron<sup>‡</sup>, F. Anfosso-Lédée<sup>§</sup>, C. Ropert<sup>¶</sup>, J. C. Dyre<sup>†</sup> and T. Hecksher<sup>†,\*</sup><sup>†</sup>IMFUFA, Roskilde University, Roskilde, Denmark<sup>‡</sup>UMRAE, Univ Gustave Eiffel, IFSTTAR, CEREMA, F-44344 Bouguenais, France<sup>§</sup>MAST, Univ Gustave Eiffel, IFSTTAR, F-44344 Bouguenais, France<sup>¶</sup>AME-EASE, Univ Gustave Eiffel, IFSTTAR, F-44344 Bouguenais, France

\*tthe@ruc.dk

Received date

Accepted date

A versatile drum setup for measuring rolling resistance of small wheels is presented. The purpose is to provide a flexible setup for testing of models for rolling resistance under controlled circumstances. To demonstrate this, measurements of rolling resistance with a series of sandpapers of different grit sizes representing surface textures were carried out. The measurements show a clear increase in the rolling-resistance coefficient with increasing surface roughness, rolling speed and load. Numerical calculations in the time domain for a visco-elastic contact model run on equivalent surfaces agree with the trends found experimentally. We conclude that this approach to simplifying the experiment in order to obtain a high degree of control, accuracy and repeatability is useful for validating and testing models for calculating the rolling resistance for a given surface texture.

*Keywords:* rolling resistance; contact mechanics; surface analysis; visco-elasticity.

**1. Introduction**

Any driving vehicle needs a continuous input of energy – in most cases in the form of fossil fuels – to overcome driving resistance. Driving resistance comes from many different sources, the more prominent being aerodynamic drag, friction in mechanical parts and rolling resistance Andersen *et al.* [2015]. In order to decrease the fuel consumption, these losses need to be minimized. Much has been done from manufacturers side on improving the fuel economy of cars, to reduce the rolling resistance of tires, etc. From an infrastructural perspective, only the road is readily available for optimization. Since the 1970's it has become increasingly clear that surface texture and unevenness (macro and mega texture) of roads is a source of driving resistance Willis *et al.* [2015]. In recent years, the focus on reduction of the rolling resistance of roads has intensified due to climate changes demanding an investigation of all possibilities for reducing the man-made CO<sub>2</sub> emission Andersen *et al.* [2015].

\*Corresponding author

Rolling resistance is caused by visco-elastic effects in the rolling object and in the surface on which it rolls. The rolling object (tire) and surface (pavement) deform by the load exerted: the surface deflects and the rolling object flattens out slightly in the contact patch. Deformation of visco-elastic materials is not entirely reversible and thus causes dissipation of energy in the form of heat. Consequently, losses occur both in the tire and in the pavement. The latter is often referred to as “structural rolling resistance” to distinguish it from the tire rolling resistance, that is limited to the losses in the tire only. Few direct measurements exist that determine the magnitude of structural rolling resistance, but this is believed to be negligible for passenger cars Chupin *et al.* [2013], while model studies estimate it to be a factor of 10-100 smaller than tire rolling resistance even for heavy traffic Pouget *et al.* [2012]; Bazi *et al.* [2018]; Nielsen *et al.* [2020].

The ISO standard (ISO25280 [2018]) for labelling tire rolling resistance consider tires running on a smooth steel surface. However, tire rolling resistance is increased when the surface is textured, because the texture causes localized indentations in the rubber in addition to the overall deformation. Most work on the texture dependence of rolling resistance either takes the form of empirical correlations between texture and measured rolling resistance Willis *et al.* [2015]; Andersen *et al.* [2015] focusing on full-scale studies (actual car tires on real roads) Sandberg *et al.* [2011]; Bergiers *et al.* [2011]; Sandberg *et al.* [2015]; Zöller [2014]; Anfosso-Lédée *et al.* [2016]; Haider *et al.* [2016]; Ejsmont *et al.* [2017]; Vieira *et al.* [2019] or pure model studies Sharma *et al.* [2020].

While this experimental approach is the most common, some studies have used different methods: Araújo *et al.* [2019] uses a small indoor test rig where a pneumatic tire is driven in a circular motion on the floor; Ejsmont and Owczarzak [2019] where the bouncing motion of a dropped tire is used for evaluating energy loss from different surface textures; Mansura *et al.* [2018] where a Packed Indenters Loading test is used to measure energy loss for different surface textures; and Riahi *et al.* [2020] used a Wehner/Schulze polishing machine with three rubber cones mounted on the rotary head to measure rolling resistance of road specimens. Lundberg *et al.* constructed a test rig for accurate measurements of contact forces and Kawakami *et al.* [2017] correlated contact pressure distribution between tire and pavement surfaces to evaluate the rolling resistance indirectly.

The crucial question in all of these studies is how to characterize a given surface texture in a way that gives a good prediction of rolling resistance. The standardized texture measure is Mean Profil Depth (MPD) ISO13473 [2019], which is also used in most studies. However, some studies suggest that MPD is not sufficient for this purpose Pinnington [2012]; Goubert and Sandberg [2018]; Ejsmont and Sommer [2021].

Early model studies of rolling resistance were based on simplified tire models in two dimensions and focusing on steady-state rolling on a flat surface Stutts and Soedel [1992]; Kim and Savkoor [1997]; Miège and Popov [2005]. More sophisti-

cated modeling of pneumatic tires consider tire structure and compounds in 3D, as well as thermo-mechanical considerations in the calculation of energy dissipation due to heat generation Park *et al.* [1997]; Lin and Hwang [2004]; Narasimha Rao *et al.* [2006].

Only little has been done to test model predictions against experimental results. Lopez [2010] and Boere *et al.* [2014] assessed rolling resistance as the sum of energy dissipation due to large steady-state tire deformations on a flat surface and energy dissipation originating from tire vibrations induced by road texture in a two-step Finite Element Model. They found a correlation between the predicted rolling resistance and the Root Mean Square (RMS) texture depth when comparing to an experimental database. Similar results have been found by Hoever and Kropp [2015] for 19 conventional road surfaces from the same data base. Likewise, Mansura *et al.* [2018] found their numerical calculations of a multi-scale tire model on surface texture to be in qualitative agreement with measurements on different road structures.

It is difficult to critically test rolling resistance models with real-life measurements beyond such correlation findings. Mainly because many variables are not experimentally controlled, e.g., temperature, surface texture, weather, etc. The parameters of any model would have to be adjusted to fit a given measurement. The validation of a parameterization should include a comparison of model predictions for a different set of conditions to real-life measurements. In most cases, such data sets do not exist.

Here we take the approach of simplifying the experimental setup as much as possible, focusing on isolating the key variables of interest. Instead of attempting to arrive at a complete model of the real-life rolling resistance, we argue as follows: Any future model must be based on robust input in the form of a reliable underlying mathematical model for the rolling resistance between a rubber and a surface with a given texture. How can one ensure that this mathematical model is reliable? The only way is to be able to test it in the laboratory, i.e., under controlled circumstances. The aim is the assessment of the part of tire rolling resistance originating from hysteretic energy dissipation at the contact interface reflecting visco-elastic properties of the tire material. The laboratory prototype developed in this work consists of a simplified drum rig with a small solid rubber wheel inside the drum. Using this setup, rolling resistance can be investigated under controlled circumstances for visco-elastic wheels, allowing for investigations and possible validation of any mathematical rolling-resistance model. The setup is designed specifically for testing the capability of models to predict the rolling resistance for a given surface texture. As a proof of concept, we present here a series of measurements of small solid rubber wheels rolling on sandpapers of varying grit size. The surface texture of the sandpapers are characterized to enable a numerical study on equivalent surfaces. It is important to emphasize that these are merely tests of the fundamental idea, not an attempt to realistically model the resistance between a pneumatic tire

and a real asphalt or concrete road.

## 2. Rolling-resistance experiment

This section describes the custom-built experimental setup, measurement principle, protocol, and results.

### 2.1. Construction and working principle of the test rig

Figure 1 shows a photo and a schematic drawing of the setup. It consists of a drum with the test wheel running on its inside. The test wheel is rotated by the drum, which in turn is driven by a motor. The conventional configuration ISO18164 [2005]; ISO25280 [2018] runs the wheel (or tire) on the outside of the drum. However, for adding texture to the drum it is more convenient to have the wheel and texture on the inside because the centrifugal forces arising when the drum rotates help keeping the texture in place on the drum. The drum has an inner diameter of 0.538 m and the test wheels diameters of 0.125 m. The moderate physical size of the setup allows for easy control of load between surface and wheel, speed/rotation velocity, wheel type and surface textures.

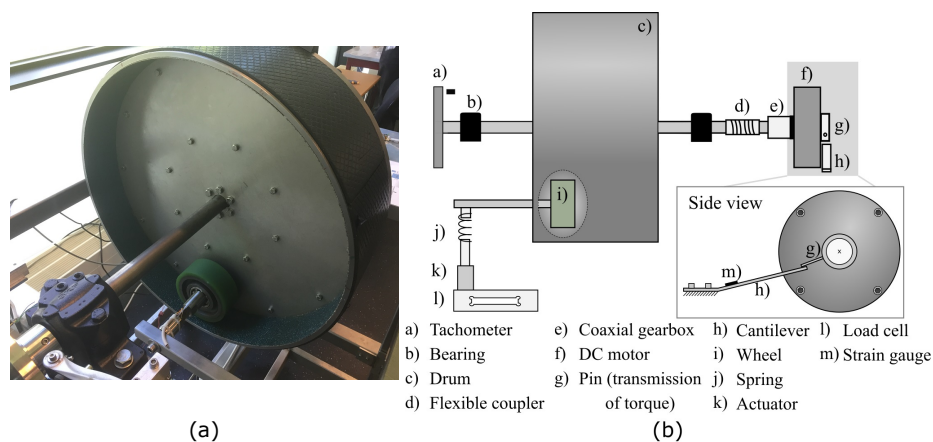


Fig. 1. The drum setup. (a) Photo of the setup showing the inside of the drum with surface texture attached. (b) Schematic illustration of the drum setup showing how the different mechanical components are connected.

The motor (component f on Fig. 1(b)) is mounted on a freely rotating drum shaft. The torque delivered by the motor to maintain a constant angular velocity of the drum is measured by the bending of a cantilever spring that supports the motor (components h on Fig. 1(b)), hindering its own opposite rotation. The torque needed to keep the drum at constant angular velocity balances the total resistance opposing the rotation, including friction in the bearings, air drag, and rolling resistance. The bending of the cantilever spring is thus a direct measure of the resisting

forces. The bending is measured by strain gauges and calibrated by weights. For more details, see Hansen and Larsen Hansen and Larsen [2017].

The load on the wheel is controlled by an actuator connected via a spring to the wheel shaft. The actuator is mounted on a load cell that monitors the load continuously during the measurement (components j,k, and l on Fig. 1(b)).

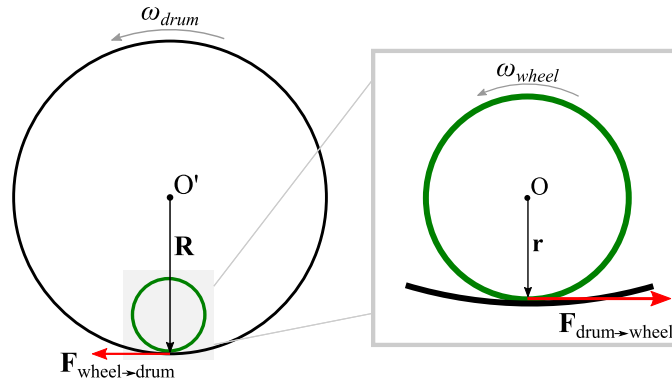


Fig. 2. Diagram showing the drum and wheel. The torque relative to the center of the drum and wheel, respectively, sum to zero at constant angular velocity.

The measurement principle makes use of the balance of the torque for both the wheel and the drum. At constant angular velocity there is no angular acceleration and thus  $\sum \tau = \mathbf{0}$ , where  $\tau$  is torque (notice that this is a vector sum). The sum of torques around the center of wheel is given by:

$$\tau_{\text{wheel}}^{\text{O}} = \tau_{RR} + \mathbf{r} \times \mathbf{F}_{\text{drum} \rightarrow \text{wheel}} + \tau_{\text{loss}}^{\text{wheel}} = \mathbf{0} \quad (1)$$

where  $\tau_{RR}$  is the rolling resistance torque,  $\mathbf{r} \times \mathbf{F}_{\text{drum} \rightarrow \text{wheel}}$  (see Fig. 2) is the torque deriving from the drum driving the rotation of the wheel, and  $\tau_{\text{loss}}^{\text{wheel}}$  is the torque coming from friction in the wheel bearing and air resistance.

The sum of torques around the center of the drum is likewise zero:

$$\tau_{\text{drum}}^{\text{O}'} = \tau_{\text{motor}} + \mathbf{R} \times \mathbf{F}_{\text{wheel} \rightarrow \text{drum}} + \tau_{\text{loss}}^{\text{drum}} = \mathbf{0}, \quad (2)$$

where  $\tau_{\text{motor}}$  is the torque delivered by the motor, i.e., what we measure,  $\mathbf{R} \times \mathbf{F}_{\text{wheel} \rightarrow \text{drum}}$  is the torque opposing the rotation coming from the wheel, and  $\tau_{\text{loss}}^{\text{drum}}$  signifies the total torque due to friction, drag, etc., on the drum. The z-components of Eqs. (1) and (2) become

$$0 = -\tau_{RR} + rF_{\text{drum} \rightarrow \text{wheel}} - \tau_{\text{loss}}^{\text{wheel}} \quad (3)$$

$$0 = \tau_{\text{motor}} - RF_{\text{wheel} \rightarrow \text{drum}} - \tau_{\text{loss}}^{\text{drum}} \quad (4)$$

Due to the principle of action and reaction (Newton's third law),  $\mathbf{F}_{\text{wheel} \rightarrow \text{drum}} = -\mathbf{F}_{\text{drum} \rightarrow \text{wheel}}$  (or equivalently for the magnitude  $F_{\text{wheel} \rightarrow \text{drum}} = F_{\text{drum} \rightarrow \text{wheel}}$ ) we

6 *Larsen, M. L. et al.*

thus obtain

$$F_{\text{wheel} \rightarrow \text{drum}} = \frac{1}{r} (\tau_{RR} + \tau_{\text{loss}}^{\text{wheel}}) = \frac{1}{R} (\tau_{\text{motor}} - \tau_{\text{loss}}^{\text{drum}}) \quad (5)$$

which gives the following

$$\tau_{\text{motor}} = \tau_{\text{loss}}^{\text{drum}} + \frac{R}{r} (\tau_{RR} + \tau_{\text{loss}}^{\text{wheel}}). \quad (6)$$

From “skim test reading” ISO18164 [2005] we can determine the loss terms, i.e., the “parasitic losses”. Skim test reading is a measurement where the wheel is positioned such that it just touches the drum surface and rotates without skidding and without deforming. In this position one should have  $\tau_{RR} = 0$ , and thus  $\tau_{\text{motor}}^{\text{skim test}} = \tau_{\text{loss}}^{\text{drum}} + \frac{R}{r} \tau_{\text{loss}}^{\text{wheel}}$ . Consequently, the rolling-resistance force,  $F_{RR}$ , can be found by subtracting the skim test reading from the measurement with load as follows

$$F_{RR} = \frac{\tau_{RR}}{r} = \frac{1}{R} (\tau_{\text{motor}} - \tau_{\text{motor}}^{\text{skim test}}), \quad (7)$$

where  $\tau_{\text{motor}}$  is the measured quantity, both in the skim test reading and with load applied to the wheel. This procedure assumes, that the loss in the various bearings in the setup is load-independent to a good approximation.

For the experiments presented in this paper two solid rubber wheels (“PUR” and “NBR”) were used. Both wheels have a metal rim with the rubber attached and ball bearings in the center (see figure 3). The PUR wheel is a commercial pallet jack wheel that has an iron rim of 53 mm in radius with a polyurethane rubber layer of 9 mm. The NBR wheel has an aluminium rim of radius 47 mm with a moulded layer of nitrile butadiene rubber of thickness 16 mm. Both wheels are 50 mm wide. Each wheel has its own set of bearings and can be easily exchanged by using the same spindle.



Fig. 3. Photos of the two test wheels used in this study. (a) Commercial polyurethane rubber (PUR) pallet truck wheel. (b) Custom made nitrile butadiene rubber (NBR) wheel.

## 2.2. Sandpapers and surface characterization

The surface texture is varied by using sandpapers of different grit size. The sandpaper is cut to fit inside the drum and attached by thin double sided tape to the

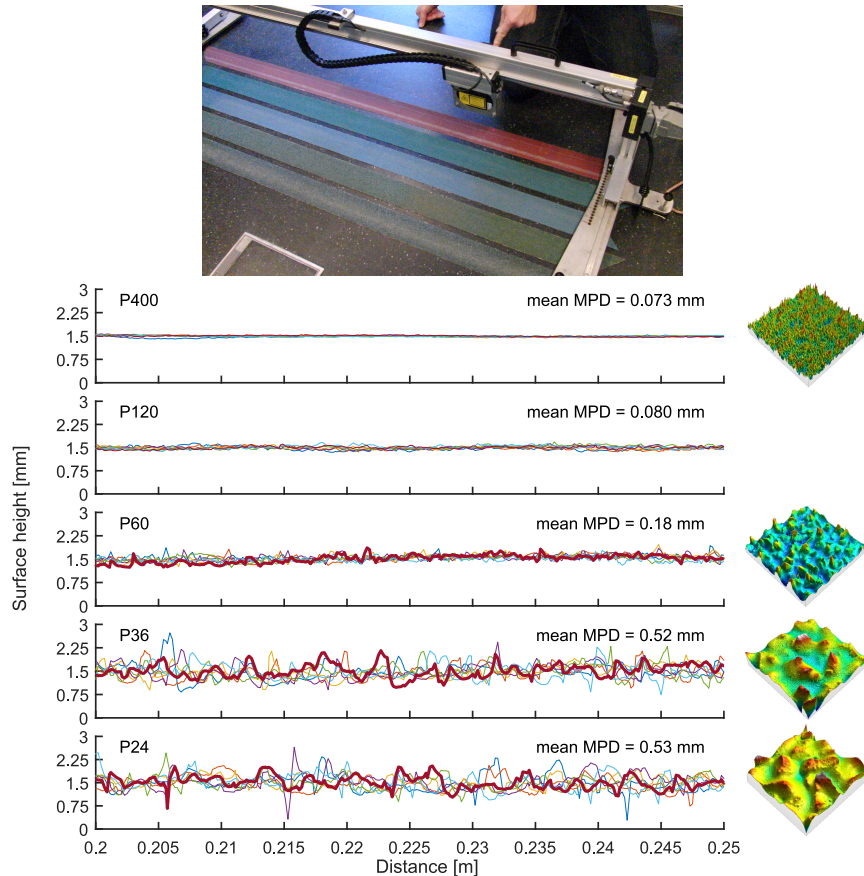


Fig. 4. Profile characterization of sandpapers used in the experiment. (a) Profilometer used to measure the surface profile of the five types of sandpaper. (b) Texture measurements for the following sandpapers: P400, P120, P60, P36 and P24. Each plot shows a section of the seven contour measurements over a length of 1.5 m. The MPD is calculated from the entire length of the seven contours. To the right of each contour plot (except for the P120 sandpaper) a high resolution 3D height scan of a  $4\text{ mm} \times 4\text{ mm}$  area is shown.

drum surface. Five different grit size sandpapers were used in addition to no sandpaper. Grit sizes of P400, P160, P60, P32 and P24 (according to the grit size standard FEPA) were used.

The profiles heights of the different sandpapers were measured by a profilometer shown in Fig. 4(a). The sandpaper is placed below the profilometer on a flat floor. A laser sensor in the profilometer measures the distance from the sensor to the surface of the sandpaper. The position of the sensor is measured with an accuracy of 0.1 mm and the distance from the sensor to the surface is measured with an accuracy of 0.1  $\mu\text{m}$ . A total of seven different paths was scanned for 1.5 m of each sandpaper type. Examples of the resulting curves are shown in Fig. 4(b). The Mean Profile Depth (MPD) value, a traditional indicator for road texture defined

in ISO13473 [2019], was calculated on the basis of these profiles. Notice that the MPD of the coarsest sandpaper (P24) is lower than that of the less coarse P36.

For P400, P60, P36, and P24 sandpapers a detailed 3D height scan of  $4\text{mm} \times 4\text{mm}$  area is added in Fig. 4(b) to illustrate the difference in surface texture. These 3D scans of the surfaces were performed by the InfiniteFocus system from Alicona. The sensor is based on the technology of focus variation. It combines the shallow depth of field of an optical system with vertical scanning. The sample is placed on a motorized platform and illuminated by a white light which can be modulated. Coaxial light is provided by a semi-transparent mirror to a series of interchangeable lenses mounted on a six-position lens holder. The reflected light is returned through the semi-transparent mirror to a digital color sensor. The vertical and lateral resolutions can go up to 10 nm and  $0.4 \mu\text{m}$  respectively and are defined by the choice of the lens. In this study, a X5 magnitude was used, which led to a vertical resolution of 870 nm and lateral resolution of  $7 \mu\text{m}$ . The image was similar to that of a microscope in the sense that it was limited by the depth of field. Images were acquired continuously while the sample to objective distance was changing. Each image varies with the distance and topography of the sample. It is critical to couple lighting, distance and image capture in this process. The focus quality is calculated for each position and its variation is used to determine the topography information.

For the contact model calculations detailed in Sec. 3, the 3D surface texture of sandpapers P24 and P60 were also measured by means of the same device. The spatial step of the measurement was  $\Delta x = \Delta y = 0.007 \text{ mm}$  and  $\Delta z = 1 \text{ nm}$ , respectively in the  $x$ ,  $y$  and  $z$  directions. The dimensions of the texture scan, namely 32.7 mm in the  $x$  direction (rolling direction) and 83.6 mm in the  $y$  direction, were limited by the capacity of the apparatus. Figure 5 shows the resulting 3D surface textures for sandpapers P24 and P60.

### 2.3. Measurement protocol

A measurement run is made for each combination of surface texture and wheel, giving a total of  $2 \times 6$  measurement runs. Each run consists of a series of different target velocities and loads. Most of the runs for this work included two different velocities and five different loads, including a zero load measurement (the skim test reading), leading to a total of 10 different setting combinations. In addition, the last three measurement runs for each texture/wheel combination were conducted in order to ensure reproducibility.

The load is controlled by the position of the actuator and a measurement run starts by setting the actuator to the first position from the target values. Then the measurement program loops through the target velocities. The power to the motor is adjusted by a PID algorithm to reach the target rotational velocity of the drum. When the drum has maintained a stable rotational velocity for 30 minutes, the power to the motor is kept constant and the logging starts. After logging a fixed

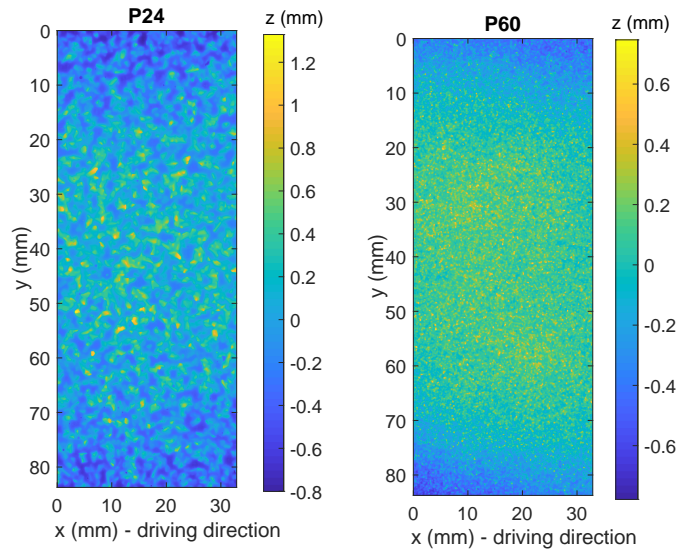


Fig. 5. Measured 3D surface textures used for contact calculation for sandpapers P24 (left) and P60 (right). The spatial resolution is  $\Delta x = \Delta y = 0.007$  mm.

number of data points for averaging (taking usually roughly 30 minutes), the actuator is moved to the next target position in an increasing manner going from small to higher loads, iterating through the target velocities, until all target combinations have been measured. Each measurement run for this study took around 24 hours.

Three quantities are monitored continuously during each measurement run: rotational velocity of the drum, the load on the wheel, and the torque exerted by the motor. An example of the output from one measurement run is shown in Fig. 6, illustrating the protocol. The gaps between each target setting is the stabilisation time.

### 2.3.1. Calculating the rolling-resistance coefficient $\mu_{RR}$

The rolling-resistance coefficient is defined as the rolling-resistance force magnitude,  $F_{RR}$ , divided by the normal force magnitude,  $F_N$

$$\mu_{RR} = \frac{F_{RR}}{F_N} \quad (8)$$

in analogy with the friction coefficient. The normal force balances the load and thus we can replace  $F_N$  by  $F_{load}$  when calculating the rolling-resistance coefficient from the measurements.

In order to ensure a stabilized value, the load and resistance force are determined by averaging the last quarter of the data points for each setting. This procedure is illustrated for the resistance force in Fig. 7(a). The first actuator position of

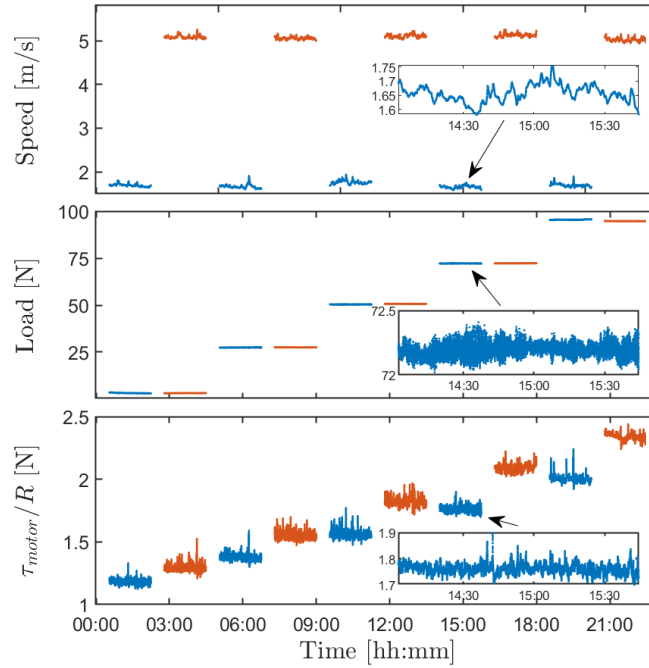


Fig. 6. Raw data from one measurement run with NBR wheel on steel surface illustrating the protocol. Each run starts at “zero” load, providing the skim test reading for determining the parasitic losses, then loops through the target velocities (here two), before changing to slightly higher load and repeating. Colors indicate measurements at different target velocities.

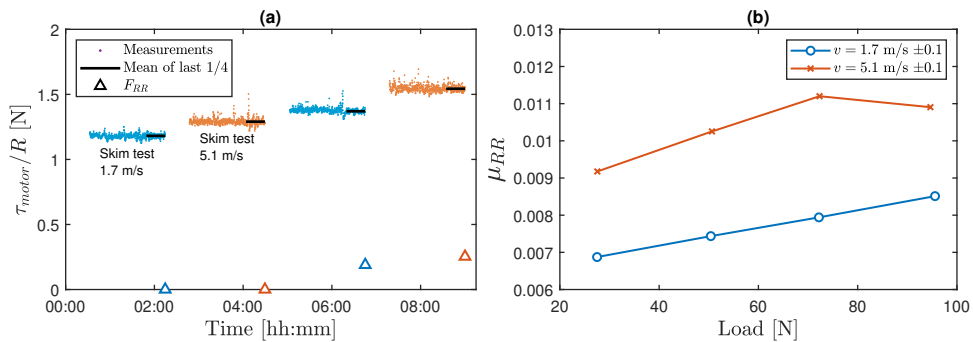


Fig. 7. Determining the rolling-resistance coefficient. (a) Plot of the measured torque, showing how parasitic losses from skim test reading are subtracted. (b) Rolling-resistance coefficient as a function of load for the NBR wheel on a steel surface obtained from the data in (a).

each measurement run is for the skim test reading. At this position only the parasitic losses, e.g., aerodynamic losses and losses from drum and wheel bearings, contribute to the total torque the motor must overcome. To obtain the rolling resistance deriving from a given surface, the skim test reading is subtracted from

the measurements with non-zero load (Eq. (7)). Figure 7 shows how the average values for resistance for different speed and loads change with and without parasitic losses. Figure 7(b) shows the  $\mu_{RR}$  average values plotted as a function of the average load for the target position.

#### 2.4. Experimental results

Figure 8 investigates the repeatability of the measurements. Rolling-resistance coefficients,  $\mu_{RR}$ , for the NBR wheel run on the smooth steel, P60, and P24 textures, are shown as a function of load for the two measured velocities. The measurement runs are generally nicely repeatable, however slightly less so for the smooth steel surface than for the two textured surfaces. Despite the somewhat larger scatter in these results, the variations with load and speed are still clearly systematic.

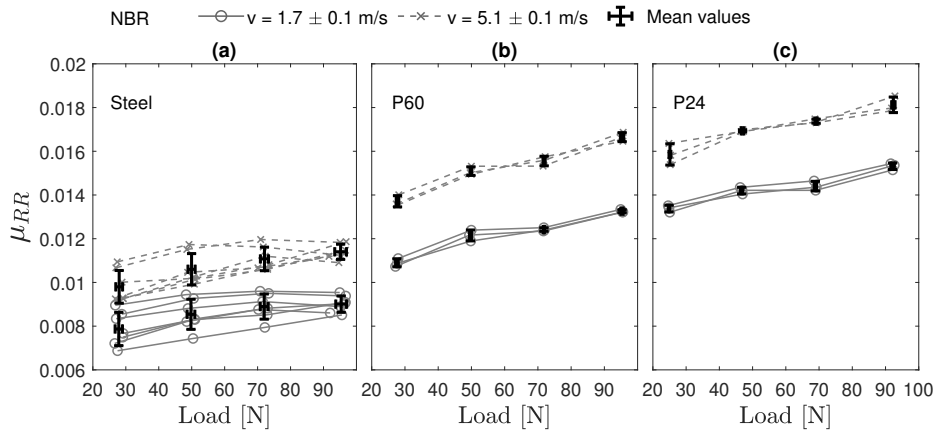


Fig. 8. Repeated measurements of the rolling-resistance coefficient as a function of load for NBR wheel.

In Fig. 9 (a-d)  $\mu_{RR}$  is plotted as a function of load for all the different textures investigated and the two velocities. Data points represent the mean of three (in a few cases more) measurement runs and error bars give the standard deviations. Several trends can be observed in the data: 1) The NBR rolling resistance coefficients lie consistently above the PUR results for identical target settings. This reflects the different visco-elastic properties of the two different materials. 2) There is a clear velocity dependence of  $\mu_{RR}$  for the NBR wheel, while the PUR results are much less dependent of velocity. Again, this reflects different visco-elastic properties of the rubbers. Only two velocities were used for the main study, so a single measurement run was added for the NBR wheel looping through more velocities (shown in Fig. 9(e)), confirming the trend. 3) For both wheels there is an increase in rolling resistance coefficient with load for all studied surface textures. This could be due to the fact that we measure at quite small loads and that the curves saturate at

12 *Larsen, M. L. et al.*

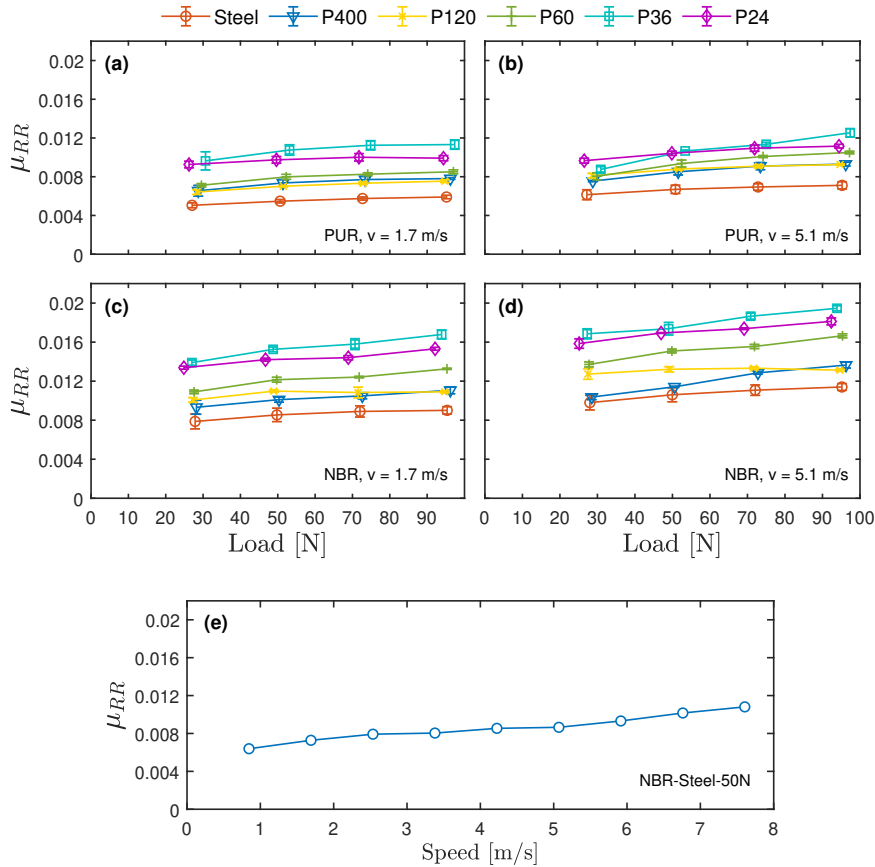


Fig. 9. Rolling resistance coefficients. (a-d) As a function of load and surface texture for PUR and NBR wheels at a speed of 1.7 m/s and 5.1 m/s. (e) As a function of speed. Data are from a separate measurement run for a single load and several speeds. The trend is a weak increase with speed.

higher loads. 4) There is a clear increase in the rolling-resistance coefficient with increasing roughness for both wheels and both studied velocities. Note that the P36 sandpaper results lie consistently above P24, which should have a coarser texture. However, the MPD value found for the P36 was higher than the that of P24, so in Fig. 10  $\mu_{RR}$  is plotted against the MPD value for a fixed load and velocity. The trend is an increase of the rolling-resistance coefficient. The data points are not monotonously increasing, though, which indicates – especially given the accuracy of the results – that the MPD measured values do not capture the essential properties of the surface texture for rolling resistance. Note that the two wheels show nearly identical behavior in this plot, only shifted slightly in the absolute level of the rolling-resistance coefficient, emphasizing that the ordering of the textures is not coincidental.

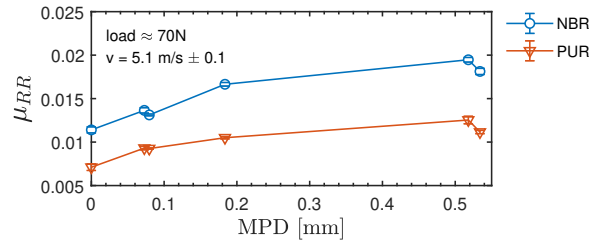


Fig. 10. Rolling resistance coefficient measurements as a function of the MPD-values. NBR and PUR wheel at a load of 70 N.

### 3. Rolling-resistance modeling

For the sake of illustrating the purpose of the experimental approach, rolling-resistance calculations based on a contact model implemented with the specific dimensions and surface textures used in the experiment were performed. The contact model is based on a 3D time-dependent approach developed by Yin *et al.* [2015] for the rolling of a rigid body on a visco-elastic half-space. This configuration can be considered equivalent to the rolling of a visco-elastic solid on a rigid surface, as mentioned by Koumi *et al.* [2015] using a similar modeling approach. Only vertical stresses are considered in this study and the effect of friction on the rolling resistance is neglected. This is reasonable since it was shown by Zéhil and Gavin [2013] that the contribution of friction to rolling resistance does not exceed a few percent, which suggests that it could be neglected in many engineering applications.

Other rolling resistance models would have been equally relevant to study, e.g., a Finite Element Method (FEM) approach. All approaches have advantages and drawbacks; The FEM approach can model the real configuration of the setup, including complex materials and the energy dissipation due to the vibration of the wheel, but will be limited for modeling the visco-elastic contact with the surface texture, especially at smaller texture wavelengths. This may be conceivable with a more sophisticated approach based on a waveguide finite element method (e.g. Hoever and Kropp [2015]). Numerical models based on the half-space assumption have found to be relevant to predict tire/road contact in rolling conditions (e.g. Wullens and Kropp [2004]; Dubois *et al.* [2013]), taking into account surface texture at small wavelengths. In Zhang [2016], the visco-elasticity of the half-space was introduced using the approach of Yin *et al.* [2015] and this model was in good agreement with experimental results of Zhang *et al.* [2017] in the case of a pneumatic tire rolling on a single asperity. Therefore the approach of Yin *et al.* [2015] was used in this study as it already proved to be relevant for modeling rolling contact of rubber like material, including the visco-elasticity and the road surface texture.

### 3.1. Calculations for test rig configurations

The configuration introduced Yin *et al.* led to an asymmetric final pressure distribution in the rolling direction ( $x$ -axis) when steady state rolling is reached. This is due to energy dissipation originating from visco-elasticity, which is maximal when  $v\tau_\varphi/a_0 = 1$ , with  $a_0 = \sqrt{r\delta}$  the radius of the contact area in the elastic case,  $v$  the rolling speed and  $\tau_\varphi$  the characteristic creep time of the the tire material. For the purpose of the present study, the rolling resistance coefficient  $\mu_{RR}$  is defined as:

$$\mu_{RR}(t) = -\frac{M_y(t)}{P(t)r} \quad (9)$$

where  $r$  is the radius of the rolling solid,  $P(t)$  is the total charge imposed, and  $M_y(t)$  is the resulting moment of contact stresses

$$M_y(t) = -\int_{\Sigma_c(t)} xp(x, y, t)dx dy. \quad (10)$$

Note, that since  $M_y$  is equal to  $-\tau_{RR}$  (Eq. (1)) and the time average of  $P(t)$  is equivalent to  $F_N$  in the experimental section, Eq. (9) is equivalent to Eq. (8).

The contact model was run considering the NBR solid wheel configuration of the test rig. The NBR layer was assumed to be an incompressible material, leading to  $\nu = 0.5$ . The problem was first studied in statics for an elastic material with  $E = 2.76$  MPa, i.e.  $G = 0.92$  MPa. Then rolling conditions were considered and the visco-elastic behaviour of the solid wheel was approached by a standard linear visco-elastic Kelvin-Voigt model

$$\varphi(t) = \frac{1}{B_\infty} + \left( \frac{1}{B_0} - \frac{1}{B_\infty} \right) e^{-\frac{t}{\tau_\varphi}} \quad (11)$$

with  $B_\infty = 1.84$  MPa,  $B_0/B_\infty = 1.6$  and  $\tau_\varphi = 4.56 \cdot 10^{-4}$  s. The value of  $B_\infty$  was derived through the rubber shore type A hardness value given by the supplier data sheet using empirical results from Gent [1958], while in the absence of material data the values of  $B_0/B_\infty$  and  $\tau_\varphi$  were adjusted to best match the experimental results from Hansen and Larsen [2017] in the case of the NBR wheel rolling on a flat surface over normal load ranging between 25 N and 150 N and rolling speeds of 1.7 m/s and 5.1 m/s.

#### 3.1.1. Contact analysis in static loading conditions

For contact analysis in static loading conditions, a potential contact area of dimensions  $L_x = 25$  mm in the longitudinal direction and  $L_y = 50$  mm in the transverse direction was considered. The spatial resolution of the mesh was  $h_x = h_y = 0.5$  mm.

Figure 11 gives the contact pressure distribution obtained for a total load of 150 N for the elastic wheel in contact with the curved drum (left) and with a perfectly flat surface (right). While the contact prints are similar (maxima at the edges of the

wheel, symmetry with respect to both axis), it is observed that the dimension of the contact area in the rolling direction is higher by about 12% in the case of the wheel in contact with the curved drum. This is purely due to geometrical conditions but can be interpreted as a higher contact stiffness in the case of the solid wheel in contact with the perfectly flat surface. However, it is assumed that this difference will have a small effect on the asymmetry of the contact pressure distribution along the longitudinal direction, which is at the origin of energy dissipation during rolling. Therefore the drum curvature will be neglected in the following for rolling contact calculation.

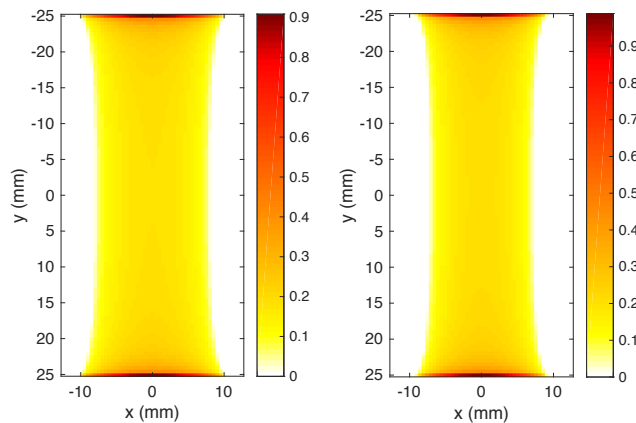


Fig. 11. Static contact pressure distribution  $p$  (in MPa) for the solid wheel in contact with the curved drum (left) and with an ideal perfectly flat surface (right) for a total load  $P$  of 150 N.

In the case of rough contact, the measured 3D texture in Fig. 5 was interpolated on the mesh grid defining the surface of the solid wheel (i.e.,  $h_x = h_y = 0.5$  mm). Figure 12 gives the contact pressure distribution obtained in statics for a total load of 150 N, in the case of the solid wheel loaded on sandpapers P24 (left) and P60 (right). Contact pressure is distributed over surface asperities and is no longer continuous, leading to a significant decrease of the total contact area in comparison with the perfectly flat case (Fig. 11). Contact pressure peaks at the edges of the cylinders are almost removed in the presence of surface roughness, while symmetry of the contact patch disappears. Due to contact concentration on local asperities, the rougher the surface, the higher is the maximum contact pressure.

### 3.1.2. Contact analysis in rolling conditions

For rolling contact calculation, the surface of the wheel was meshed with  $h_x = 0.5$  mm and  $h_y = 2.5$  mm. Preliminary calculations with a finer mesh along the transverse direction  $y$  have shown to have a small influence on the rolling resistance coefficient, while increasing drastically calculation time. In the case of rough sur-

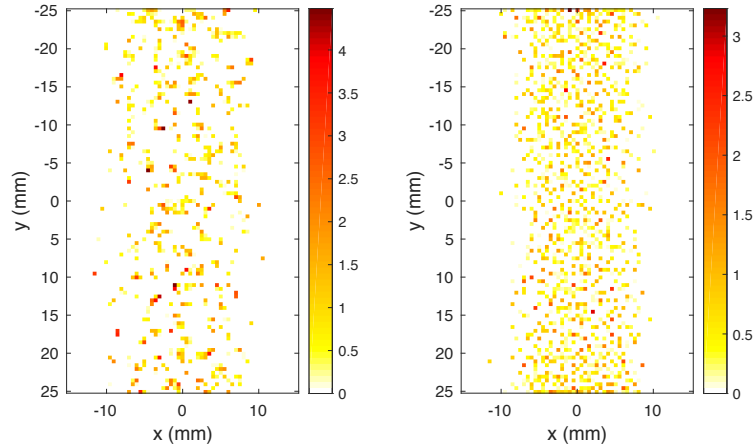


Fig. 12. Static contact pressure distribution  $p$  (in MPa) for the solid wheel in contact with sandpapers P24 (left) and P60 (right) for a total load  $P$  of 150 N.

faces, the measured texture in Fig. 5 was downsampled by a factor of 20 and periodised to get a longer surface in the rolling direction. This is illustrated in Fig. 13 for sandpaper P24, together with the mesh of the solid wheel. During rolling the periodised rough surface was interpolated on the mesh grid of the solid wheel at each time step.

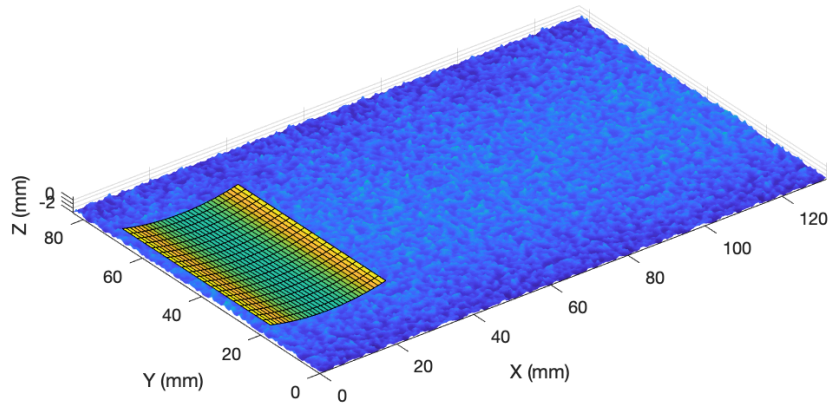


Fig. 13. Periodisation of the measured rough surface P24 for contact calculation with the solid wheel in rolling conditions.

A parametric study has been performed for several values of the normal load  $P$  and the rolling speed  $v$ , which were kept constant during time.  $P$  ranged between 25 N and 150 N, while  $v$  was linearly spaced between 0.85 m/s and 7.61 m/s. In the case of the solid wheel rolling on a flat surface, Fig. 14 gives the contact pressure

distribution obtained at the final time step  $T$  for  $P = 50$  N and different rolling speeds. The asymmetry of the contact pressure distribution with respect to the transverse axis  $y = 0$  increases with rolling speed. The higher the rolling speed, the higher is the contact pressure distribution shift to the front of the contact area. The pressure values also increase with rolling speed.

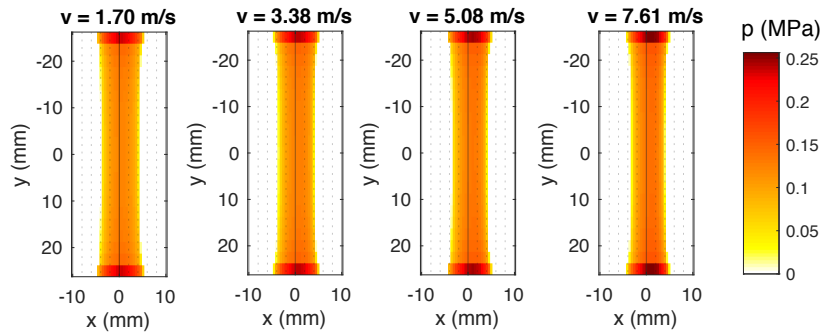


Fig. 14. Final contact pressure distribution at  $t = T$  for different rolling speeds  $v$  and a total load  $P$  of 50 N in the case of the solid wheel rolling on a flat surface.

The rolling-resistance coefficient  $\mu_{RR}$  as a function of time  $t$  is depicted in Fig. 15 (a) for each rolling speed and a fixed total load of 50 N. The shape of the time signals is similar, but the slope at the origin increases with rolling speed. Figure 15 (b) gives  $\mu_{RR}(t)$ , and for different total load and a fixed rolling speed  $v = 5.07$  m/s. In all cases, steady state is reached and  $\mu_{RR}$  maintains a constant value.

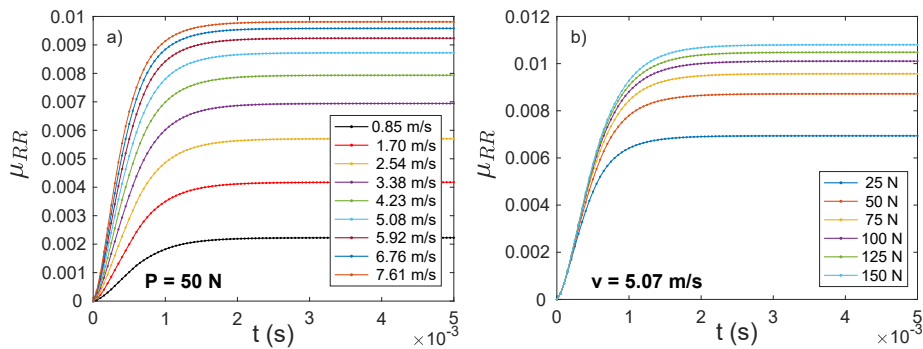


Fig. 15. Rolling-resistance coefficient  $\mu_{RR}$  as a function of time  $t$  for different rolling speeds  $v$  and a fixed total load  $P = 50$  N (a) and for different total loads  $P$  and a fixed rolling speed  $v = 5.07$  m/s (b) for a solid wheel rolling on a flat surface.

In the case of rolling on sandpapers P24 and P60, Fig. 16 gives  $\mu_{RR}(t)$  for each total load and a constant rolling speed  $v = 5.07$  m/s. Contrary to the rolling on

a smooth surface (Fig. 15), the rolling-resistance coefficient does not reach a stationary state, but fluctuates somewhat even during steady-state rolling conditions. While the shape of the time signals looks similar, the extreme values of the signals are slightly shifted in time, depending on the value of the vertical load.

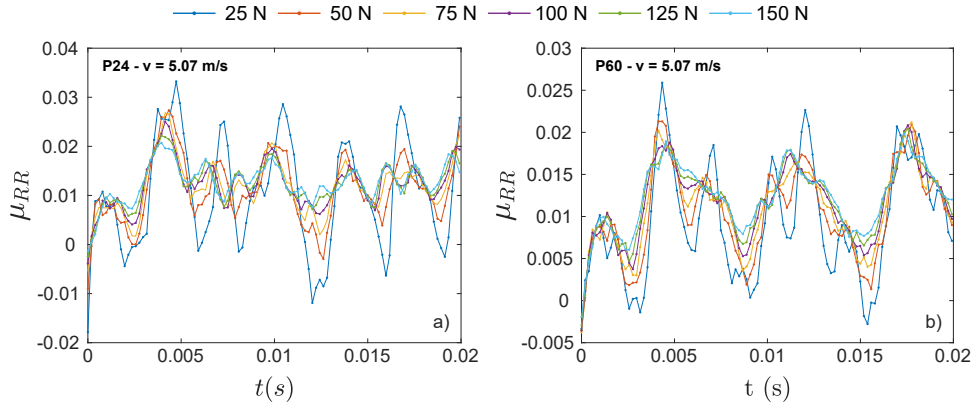


Fig. 16. Rolling resistance coefficient  $\mu_{RR}$  as a function of time  $t$  when the solid wheel is rolling on sandpapers P24 (a) and P60 (b). The vertical load  $P$  is constant during rolling and is ranging between 25 N and 150 N. The rolling speed is  $v = 5.07$  m/s.

The averaged coefficient of rolling resistance  $\bar{\mu}_{RR}$  as a function of the total load  $P$  is given in Fig. 17(a) for sandpapers P24 and P60. The final value of the rolling resistance coefficient  $\mu_{RR}(T)$  on the smooth surface is also given for comparison. Two rolling speeds of 5.07 m/s and 1.69 m/s are considered. The effect of the load and surface roughness on rolling resistance is minor for a rolling speed of 1.69 m/s. On the contrary, at the rolling speed 5.07 m/s, the averaged coefficient of rolling resistance increases with vertical load and with surface roughness.

Similarly, Fig. 17(b) gives  $\bar{\mu}_{RR}$  on sandpapers P24 and P60 and  $\mu_{RR}(T)$  on the smooth surface as a function of the rolling speed  $v$ . The total load  $P$  is fixed to 50 N. It is observed that the coefficient of rolling resistance increases with rolling speed following a non-linear relationship for all three surfaces. At low rolling speeds the three curves are nearly identical, while they separate out at higher rolling speeds with the P24 giving the highest rolling resistance coefficient and the flat surface the lowest.

## 4. Discussion and concluding remarks

### 4.1. Model vs. experiment

Numerical model calculations were carried out for a solid rubber wheel on a subset of surfaces used in the experiment (smooth steel, P60 and P24), for the same rolling speeds and the same range of vertical loads, allowing for not only a qualitative

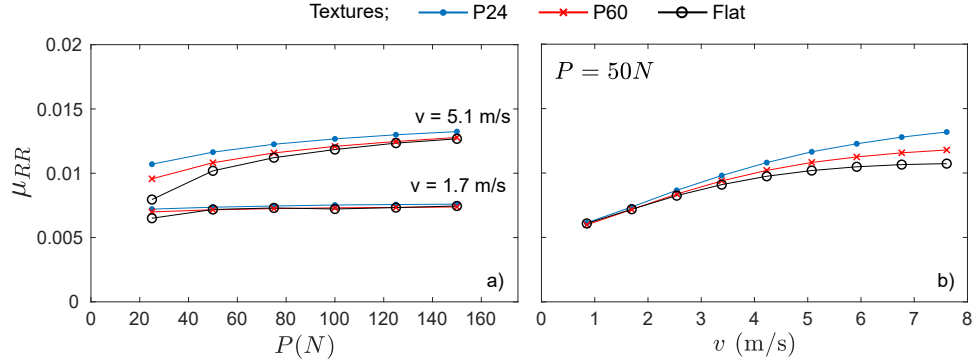


Fig. 17. Averaged coefficient of rolling resistance  $\bar{\mu}_{RRR}$  for sandpapers P24 and P60 compared to the final rolling resistance coefficient  $\mu_{RRR}(T)$  on the smooth surface as a function of the total normal load  $P$  for two different rolling speeds: 5.07 m/s and 1.69 m/s (a) and as a function of rolling speed,  $v$ , for  $P = 50$  N (b).

comparison but also a quantitative comparison. The visco-elastic behavior of the nitril butadiene rubber used in the experiment was modeled by a Kelvin-Voigt model with three parameters: the short-time and long-time constants (respectively  $B_0$  and  $B_\infty$ ) and the characteristic time,  $\tau_\phi$ .

Table 1 shows numerical and experimental values for the rolling-resistance coefficient of the NBR wheel at a load of 50 N. The values are similar in magnitude and nearly identical for the flat (smooth steel) surface the values, which is not surprising since the visco-elastic parameters for the rubber model were adjusted to these conditions. The experimental values are consistently higher for the textured surfaces. The increase in the rolling resistance coefficient with surface roughness is larger in the experimental data, while the relative increase with speed for a given surface is larger for the numerical results. The numerical results are nearly independent of surface texture studied here at the low speed.

Table 1. Comparison of measured and predicted rolling resistance coefficient at  $P = 50$  N for two rolling speeds  $v = 1.7$  m/s and  $v = 5.1$  m/s in the case of the NBR solid wheel.

$v$	1.7 m/s		5.1 m/s	
	Experimental	Numerical	Experimental	Numerical
Flat	0.0085	0.0072	0.0106	0.0102
P60	0.0122	0.0072	0.0132	0.0108
P24	0.0142	0.0074	0.0169	0.0116

Generally, a higher value for experimental measurements compared to numerical values is not unexpected, given that not all effects (e.g., vibrational losses) are considered in the model. The difference for textured surfaces is, on the other hand, dramatic and might indicate unknown sources of error, either in the model or the experiment. In the experiment, one additional source of loss could be the layer of

double sided tape that fixates the sandpaper in the drum. This is, however, a very thin layer so this would most likely be a minor contribution.

Another, perhaps more likely, possibility for the deviations is the model for the visco-elastic properties of the rubber not being accurate enough. An obvious improvement would be to measure the complex frequency-dependent shear modulus of the rubber by a different technique and to fit a generalized Kelvin model to the measured creep function instead of using a the Kelvin-Voigt model with a single creep characteristic time. It is likely that some characteristic times missing in the present model will dissipate energy at smaller length scale than the contact patch length in the rolling direction, e.g., at the scale of characteristic asperity sizes present for rough surfaces. This could partly explain underestimation of rolling resistance observed in this study with the model in the case of rough surface by comparison with experimental results.

#### 4.2. *Our experiment vs. other experiments*

As discussed in the introduction, the approach of scaling down the experimental setup and working with solid wheels – instead of pneumatic tires in full scale measurements – is not very common, especially combined with the primary purpose being the test and validation of models for rolling resistance. A study by Lundberg *et al.* [2017] has a similar idea of constructing a test rig for controlled measurements of contact forces. Their focus, however, is complementary to ours, namely delivering reliable empirical input for tire construction in the absence of a theoretical understanding where we aim for a reliable model-validation setup.

Riahi *et al.* [2020] report another similar idea of a simplified setup to measure texture dependent rolling resistance. They use a Wehner/Schulze polishing machine containing three rubber cones mounted on the rotary head and rolling on a given road specimen. The focus here was how to relate (or translate) these faster and simpler measurements to trailer measurements on the same road surfaces.

Pneumatic tires are complicated structures with many layers of different materials, tread patterns, etc. This makes direct comparisons with full scale measurements of rolling-resistance coefficient – either on drums or on actual roads – less obvious. Yet, the values obtained in the present work (both for model and experiment) are in the same range as those typically obtained in full scale measurements,  $\mu_{RR} = 0.005-0.02$  Anfosso-Lédée *et al.* [2016]; Bergiers *et al.* [2011]; Ejsmont *et al.* [2016], indicating that the main contribution to the rolling resistance loss is really the rubber, also in the pneumatic tires. Comparing trends in our experiment with full scale measurements might therefore still be relevant.

We found the rolling-resistance coefficient to depend on all the controlled parameters: load, speed, surface texture, and wheel material type. To start with the latter, it is hardly surprising that the material influences the loss. The frequency-dependent visco-elastic properties of different types of elastomers are known to be different and also to vary with molecular weight, filler content, etc., within the

same type Ferry [1980]. Thus the overall magnitude of the rolling-resistance coefficient as well as rolling speed dependence should be different, especially in the simplified case of solid rubber wheel used in our experiment. We found that the rolling-resistance coefficient for the PUR wheel was consistently lower than that of the NBR wheel for a given combination of speed, load and texture. Similarly, Benninger [2008] showed that in a full-scale tire design based on polyurethane instead of natural rubber, the rolling resistance in the lab under identical conditions was significantly (about a factor of 2) lowered. Also, the rolling-resistance coefficient for the PUR wheel showed only a weak speed dependence, which indicates that at ambient conditions, the typical time scale for visco-elastic response of the polyurethane rubber is higher, leading to a more elastic, yet slightly increasing speed dependent, behavior. The loss could also be generally lower in polyurethane compared to the nitrile butadiene rubber.

Various publications report the rolling resistance be independent of, or even decreasing with the speed. The speeds in these studies are normal driving speeds, i.e., between 50 km/h and 80 km/h corresponding to 13.9 m/s and 22.2 m/s and thus – if the rolling resistance in car tires is mostly due to visco-elastic effects in the tire rubber – they could be due to the “deformation frequency” being on the high-frequency side of the mechanical loss peak.

The mere definition of the rolling-resistance coefficient given in Eq. (8) assumes the rolling-resistance force to depend linearly on the load, i.e., the rolling-resistance coefficient to be *independent* of the load. We found it be weakly, but consistently, increasing with load for both wheels on all tested surfaces and tested rolling speeds. The rate of increase is for some measurements decreasing, and thus the curves may approach a plateau where  $\mu_{RR}$  is constant. Some full scale studies showing rolling-resistance coefficient to be independent of load within the error of the measurement (see, e.g., Bergiers *et al.* [2011]) might therefore be due to a somewhat higher load being used in those experiments. On the other hand, Ejsmont *et al.* found both increasing, decreasing and constant rolling resistance coefficients as a function of load, so the specific load dependence may depend on the exact details of the test tire.

### 4.3. Texture measures

A road surface is complicated with structure on many length scales Sandberg *et al.* [2011]; Quan *et al.* [2013]; Andersen *et al.* [2015], so one of the important questions is what parameters are essential for characterizing the roughness to predict the resulting rolling resistance. Some works claim that the MPD measure Delanne [1994]; Sandberg *et al.* [2011] or the RMS texture depth Lopez [2010] is a good predictor of rolling resistance. Others point in the direction that enveloping effects need to be taken into account Pinnington [2012]; Andersen [2015]; Ejsmont *et al.* [2016]; Goubert and Sandberg [2018]; Vieira *et al.* [2019]. This makes sense, since the tire does not necessarily “see” the bottom of the texture, but definitely the top. This is also

supported by Kawakami *et al.* [2017] who found that the distribution of contact pressure between tire and pavement surface provide a better correlation with the rolling-resistance coefficient.

In the present study, six surface textures were investigated: P24, P36, P60, P120, P400 and steel. The steel surfaces is assumed to have a MPD value of practically zero. Categorising the sandpaper using a profilometer to calculate MPD values gave nearly the same ordering as suggested by the gritsize, except for P36 that turned out to have a higher MPD value than P24. At first this may seem surprising, since P24 should be coarser than the P36, but the grit size only gives the number of grits per area which does not necessarily imply anything about the depth of the texture. Normally, these quantities perhaps scale with each other, which could explain why in some studies a good correlation with MPD is found. In Figs. 9 and 10 the general tendency is an increasing  $\mu_{RR}$  with increasing MPD value, though not monotonically within the accuracy of the measurement, suggesting that the MPD is a too simple measure and that a measure including more details of the texture (as the self-affine measure suggested by Torbruegge and Wies [2015]) or including only the part of the texture that the tire sees (as the MPD combined with some enveloping function suggested by Goubert and Sandberg [2018] and Ejsmont and Sommer [2021]) is more appropriate.

In continuation of the present work, we aim to use 3D printed surfaces for absolute control over the texture. In this way one can critically test possible correlations of texture measures with the measured rolling resistance.

## 5. Summary

This paper described a novel setup for the validation of rolling-resistance models under controlled circumstances. The fundamental idea is that, if one has valid quantitative model for the rolling resistance between tire and road, this model must also work for solid wheels rolling on sandpaper.

To validate the setup, we carried out a systematic parametric study of the rolling-resistance coefficient with a custom-built, scaled-down drum setup that accurately measures the rolling resistance of solid rubber wheels. The rolling-resistance coefficient increases with increasing rolling speed and increasing load, and depends on the rubber type and surface roughness. These results were compared to numerical calculations adjusted to replicate the experimental setup in dimensions, materials and surfaces. The numerical results agree qualitatively with the experimental results, but lack a complete quantitative agreement, in general predicting a lower rolling-resistance coefficient than what is found experimentally. This shows that the model could be improved, e.g., by a proper characterization of the visco-elastic properties of the rubber. We conclude that the approach demonstrates the usefulness of having a rolling-resistance model validation laboratory that simplifies the experiment to obtain a high degree of control.

### Acknowledgements

A special thanks goes the Danish Road Directorate for helping with profilometer measurements of textures.

This work was supported by the VILLUM Foundation's Matter (Grant No. 16515), Innovation Fund Denmark as a part of the ROSE Project (No. 5160-00009B), and the Danish Road Directorate.

### References

- Andersen, L. G. [2015] *Rolling Resistance Modelling: From Functional Data Analysis to Asset Management System*, phdthesis, Roskilde University, Roskilde, Denmark.
- Andersen, L. G., Larsen, J. K., Fraser, E. S., Schmidt, B. and Dyre, J. C. [2015] "Rolling resistance measurement and model development," *Journal of Transportation Engineering* **141**(2), doi:10.1061/(ASCE)TE.1943-5436.0000673.
- Anfosso-Lédée, F., Cerezo, V., Karlsson, R., Bergiers, A., Dauvergne, S., Ejsmont, J., Goubert, L., Lesdos, H., Maeck, J., Sandberg, U., Sjogren, L. and Zöller, M. [2016] "Experimental validation of the rolling resistance measurement method including updated draft standard," resreport, IFSTTAR, ROSANNE Deliverable D3.6.
- Araújo, J. P. C., Palha, C. A., Martins, F. F., Silva, H. M. and Oliveira, J. R. [2019] "Estimation of energy consumption on the tire-pavement interaction for asphalt mixtures with different surface properties using data mining techniques," *Transportation Research Part D: Transport and Environment* **67**, 421, doi:10.1016/j.trd.2018.12.022.
- Bazi, G., Hajj, E. Y., Ulloa-Calderon, A. and Ullidtz, P. [2018] "Finite element modelling of the rolling resistance due to pavement deformation," *International Journal of Pavement Engineering* **21**(3), 365–375, doi:10.1080/10298436.2018.1480778, URL <https://doi.org/10.1080/10298436.2018.1480778>.
- Benninger, G. N. [2008] "A status report on the amerityre pneumatic polyurethane passenger car tire," techreport, Amerityre Corporation Inc., <https://www.rubbernews.com/assets/PDF/RN86184218.pdf>.
- Bergiers, A., Goubert, L., Anfosso-Lédée, F., Dujardin, N., Ejsmont, J. A., Sandberg, U. and Zöller, M. [2011] "Comparison of rolling resistance measuring equipment - pilot study," resreport, VTI, MIRIAM, SP1 Deliverable No. 3.
- Boere, S., Arteaga, I. L., Kuijpers, A. and Nijmeijer, H. [2014] "Tyre/road interaction model for the prediction of road texture influence on rolling resistance," *International Journal of Vehicle Design* **65**(2/3), 202, doi:10.1504/IJVD.2014.060815.
- Chupin, O., Piau, J.-M. and Chabot, A. [2013] "Evaluation of the Structure-induced Rolling Resistance (SRR) for pavements including viscoelastic material layers," *Materials and Structures* **46**(4), 683–696, doi:10.1617/s11527-012-9925-z.
- Delanne, Y. [1994] "The influence of pavement evenness and macrotexture on fuel consumption," in B. Kulakowski (ed.), *Vehicle-Road Interaction* (West Con-

## 24 References

- shohocken, PA: ASTM International), pp. 240–240–8, doi:10.1520/STP13259S.
- Dubois, G., Cesbron, J., Yin, H. P., Anfosso-Lédée, F. and Duhamel, D. [2013] “Statistical estimation of low frequency tyre/road noise from numerical contact forces,” *Applied Acoustics* **74**(9), 1085–1093.
- Ejsmont, J. and Owczarzak, W. [2019] “Engineering method of tire rolling resistance evaluation,” *Measurement* **145**, 144 – 149, doi:10.1016/j.measurement.2019.05.071.
- Ejsmont, J. and Sommer, S. [2021] “Selected aspects of pavement texture influence on tire rolling resistance,” *Coatings* **11**(7), 776, doi:10.3390/coatings11070776.
- Ejsmont, J., Taryma, S., Ronowski, G. and Swieczko-Zurek, B. [2016] “Influence of load and inflation pressure on the tyre rolling resistance,” *International journal of automotive technology* **17**(2), 237–244, doi:10.1007/s12239-016-0023-z.
- Ejsmont, J. A., Ronowski, G., Świczko Żurek, B. and Sommer, S. [2017] “Road texture influence on tyre rolling resistance,” *Road Materials and Pavement Design* **18**(1), 181–198, doi:10.1080/14680629.2016.1160835.
- Ferry, J. D. [1980] *Viscoelastic properties of polymers* (John Wiley & Sons, Inc).
- Gent, A. N. [1958] “On the Relation between Indentation Hardness and Young’s Modulus,” *Rubber Chemistry and Technology* **31**(4), 896–906, doi:10.5254/1.3542351.
- Goubert, L. and Sandberg, U. [2018] “Enveloping texture profiles for better modelling of the rolling resistance and acoustic qualities of road pavements,” in *8th Symposium on Pavement Surface Characteristics: SURF 2018 – Vehicle to Road Connectivity* (Australian Road Research Board (ARRB), Brisbane, Queensland, Australia), pp. 1–12.
- Haider, M., Conter, M., Green, M., Schmidt, B. and Sandberg, U. [2016] “Status of the eu-project ROSANNE,” *Transportation Research Procedia* **14**, 2946–2955, doi:10.1016/j.trpro.2016.05.415, URL <https://www.sciencedirect.com/science/article/pii/S2352146516304215>, transport Research Arena TRA2016.
- Hansen, L. and Larsen, M. [2017] *An experimental investigation of rolling resistance*, Master’s thesis, Roskilde University.
- Hoever, C. and Kropp, W. [2015] “A model for investigating the influence of road surface texture and tyre tread pattern on rolling resistance,” *Journal of Sound and Vibration* **351**, 161–176, doi:10.1016/j.jsv.2015.04.009.
- ISO13473 [2019] “Characterization of pavement texture by use of surface profiles — part 1: Determination of mean profile depth,” Standard ISO 13473-1:2019, International Organization for Standardization, Geneva, CH, <https://www.iso.org/standard/45111.html>.
- ISO18164 [2005] “Passenger car, truck, bus and motorcycle tyres — methods of measuring rolling resistance,” Standard ISO 18164:2005, International Organization for Standardization, Geneva, CH, <https://www.iso.org/standard/33328.html>.

- ISO25280 [2018] "Passenger car, truck and bus tyres — methods of measuring rolling resistance — single point test and correlation of measurement results," Standard ISO 28580:2018, International Organization for Standardization, Geneva, CH, <https://www.iso.org/standard/67531.html>.
- Kawakami, A., Ishigaki, T., Shirai, Y., Terada, M. and Kubo, K. [2017] "Evaluation method of pavement surface characteristics for rolling resistance," *Road Materials and Pavement Design* **18**(sup2), 2–11, doi:10.1080/14680629.2017.1304264.
- Kim, S.-J. and Savkoor, A. R. [1997] "The Contact Problem of In-Plane Rolling of Tires on a Flat Road," *Vehicle System Dynamics* **27**(sup001), 189–206, doi:10.1080/00423119708969654.
- Koumi, K. E., Chaise, T. and Nelias, D. [2015] "Rolling contact of a rigid sphere/sliding of a spherical indenter upon a viscoelastic half-space containing an ellipsoidal inhomogeneity," *Journal of the Mechanics and Physics of Solids* **80**, 1–25, doi:10.1016/j.jmps.2015.04.001.
- Lin, Y.-J. and Hwang, S.-J. [2004] "Temperature prediction of rolling tires by computer simulation," *Mathematics and Computers in Simulation* **67**(3), 235–249, doi:10.1016/j.matcom.2004.07.002.
- Lopez, I. [2010] "Influence of material damping on the prediction of road texture and tread pattern related rolling resistance," in *Proceeding of ISMA 2010* (Leuven, Belgium), pp. 4039–4052.
- Lundberg, O. E., Kari, L. and Arteaga, I. L. [2017] "A compact internal drum test rig for measurements of rolling contact forces between a single tread block and a substrate," *Measurement* **103**, 370 – 378, doi:10.1016/j.measurement.2016.12.041.
- Mansura, D. A., Thom, N. H. and Beckedahl, H. J. [2018] "Numerical and experimental predictions of texture-related influences on rolling resistance," *Transportation Research Record: Journal of the Transportation Research Board* **2672**(40), 430–439, doi:10.1177/0361198118776114.
- Miège, A. J. P. and Popov, A. A. [2005] "Truck tyre modelling for rolling resistance calculations under a dynamic vertical load," *Proceedings of the Institution of Mechanical Engineers, Part D: Journal of Automobile Engineering* **219**(4), 441–456, doi:10.1243/095440705X11176.
- Narasimha Rao, K. V., Kumar, R. K. and Bohara, P. C. [2006] "A Sensitivity Analysis of Design Attributes and Operating Conditions on Tyre Operating Temperatures and Rolling Resistance Using Finite Element Analysis," *Proceedings of the Institution of Mechanical Engineers, Part D: Journal of Automobile Engineering* **220**(5), 501–517, doi:10.1243/09544070JAUTO170.
- Nielsen, N. R., Chatti, K., Nielsen, C. P., Zaabar, I., Hjorth, P. G. and Hecksher, T. [2020] "Method for direct measurement of structural rolling resistance for heavy vehicles," *Transportation Research Record* **2674**(5), 371–380, doi:10.1177/0361198120915699, URL <https://doi.org/10.1177/0361198120915699>.
- Park, H. C., Youn, S., Song, T. S. and Kim, N. [1997] "Analysis of Temperature Distribution in a Rolling Tire Due to Strain Energy Dissipation," *Tire Science and*

- Technology* **25**(3), 214–228, doi:10.2346/1.2137541.
- Pinnington, R. J. [2012] “A particle-envelope surface model for road–tyre interaction,” *International Journal of Solids and Structures* **49**(3), 546 – 555, doi: 10.1016/j.ijsolstr.2011.10.022.
- Pouget, S., Sauzéat, C., Benedetto, H. D. and Olard, F. [2012] “Viscous Energy Dissipation in Asphalt Pavement Structures and Implication for Vehicle Fuel Consumption,” *Journal of Materials in Civil Engineering* **24**(5), 568–576, doi:10.1061/(ASCE)MT.1943-5533.0000414.
- Quan, W., Wang, H., Liu, X. and Zhang, S. [2013] “Multi-fractal Analysis for Pavement Roughness Evaluation,” *Procedia - Social and Behavioral Sciences* **96**, 2684 – 2691, doi:10.1016/j.sbspro.2013.08.301, intelligent and Integrated Sustainable Multimodal Transportation Systems Proceedings from the 13th COTA International Conference of Transportation Professionals (CICTP2013).
- Riahi, E., Ropert, C. and Do, M.-T. [2020] “Developing a laboratory test method for rolling resistance characterisation of road surface texture,” *Surface Topography: Metrology and Properties* **8**(2), 024006, doi:10.1088/2051-672x/ab8aa6, URL <https://doi.org/10.1088/2051-672x/ab8aa6>.
- Sandberg, U., Bergiers, A., Ejsmont, J. A., Goubert, L., Karlsson, R. and Zöller, M. [2011] “Road surface influence on tyre/road rolling resistance,” resreport, VTI, MIRIAM, SP1 Deliverable No. 4.
- Sandberg, U., Haider, M., Conter, M., Goubert, L., Bergiers, A., Glaeser, K.-P., Schwalbe, G., Zöller, M., Boujard, O., Hammarström, U., Karlsson, R., Ejsmont, J. A., Wang, T. and Harvey, J. [2015] “Rolling resistance – basic information and state-of-the-art on measurement methods,” resreport, VTI, MIRIAM, SP1 Deliverable No. 1.
- Sharma, A. K., Bouteldja, M. and Cerezo, V. [2020] “Multi-physical model for tyre–road contact – the effect of surface texture,” *International Journal of Pavement Engineering* **0**(0), 1–18, doi:10.1080/10298436.2020.1769844, URL <https://doi.org/10.1080/10298436.2020.1769844>.
- Stutts, D. and Soedel, W. [1992] “A simplified dynamic model of the effect of internal damping on the rolling resistance in pneumatic tires,” *Journal of Sound and Vibration* **155**(1), 153–164, doi:10.1016/0022-460X(92)90652-E.
- Torbruegge, S. and Wies, B. [2015] “Characterization of pavement texture by means of height difference correlation and relation to wet skid resistance ,” *Journal of Traffic and Transportation Engineering* **2**(2), 59–67.
- Vieira, T., Sandberg, U. and Erlingsson, S. [2019] “Negative texture, positive for the environment: effects of horizontal grinding of asphalt pavements,” *Road Materials and Pavement Design* **22**(1), 1–22, doi:10.1080/14680629.2019.1610476.
- Willis, J. R., Robbins, M. M. and Thompson, M. [2015] “Effects of pavement properties on vehicular rolling resistance: a literature review,” Tech. rep., National Center for Asphalt Technology.
- Wullens, F. and Kropp, W. [2004] “A three-dimensional contact model for

- tyre/road interaction in rolling conditions," *Acta Acustica* **90**, 702–711.
- Yin, H. P., Cesbron, J. and Bui, Q. H. [2015] "A new formulation for solving 3-D time dependent rolling contact problems of a rigid body on a viscoelastic half-space," *Mechanics Research Communications* **64**, 8–14, doi:10.1016/j.mechrescom.2014.12.006.
- Zhang, Y. [2016] *tudy on a test rig of dynamic tyre/road contact forces at the origin of rolling noise*, PhD thesis, École Centrale de Nantes – Université Bretagne Loire.
- Zhang, Y.-F., Cesbron, J., Yin, H.-P. and Bérengier, M. [2017] "Experimental study of normal contact force between a rolling pneumatic tyre and a single asperity," *International Journal of Applied Mechanics* **9**(7), 1750081, doi:10.1142/S1758825117500818, URL <https://doi.org/10.1142/S1758825117500818>.
- Zéhil, G.-P. and Gavin, H. P. [2013] "Three-dimensional boundary element formulation of an incompressible viscoelastic layer of finite thickness applied to the rolling resistance of a rigid sphere," *International Journal of Solids and Structures* **50**(6), 833–842, doi:10.1016/j.ijsolstr.2012.11.020.
- Zöller, M. [2014] "State of the art on rolling resistance measurement devices," techreport, AIT, URL <https://www.rosanne-project.eu/documents?id=7299>, ROSANNE, Deliverable D3.1.

**C.2 Draft: Laboratory for Validation of Rolling  
Resistance Models. II. Rolling Resistance  
of Periodic 3D-Printed Surfaces**

**Laboratory for Validation of Rolling Resistance Models. II. Rolling  
resistance of periodic 3D-printed surfaces**

Morten L. Larsen, Jeppe C. Dyre, Tina Hecksher\*

*Glass and Time, IMFUFA, Department of Science and Environment,  
Roskilde University, P.O. Box 260, DK-4000 Roskilde, Denmark*

(Dated: January 3, 2022)

## Abstract

In order to be able to quantify how a given surface texture affects the rolling resistance of a wheel, a setup is devised for controlled measurements in the laboratory. This “model-validation laboratory” is based on a steel drum of 54 cm inner diameter inside which an 10-15 cm diameter test wheel rolls on a 3d-printed surface. The setup is located in a cube of side length 2 m, defining a thermo-controlled cage. Rolling resistance is determined from measurements of the motor torque required to maintain a constant angular velocity by a calculation that subtracts parasitic losses identified from a skim, i.e., zero-load, measurement. By the use of 3d-printed surfaces, the setup enables systematic investigations of how surface texture affects the rolling resistance. We present data for three different solid rubber wheels at two speeds and several loads, probing different regular 3D printed surfaces placed inside the steel drum. The peak fraction provides a better predictor of the rolling-resistance coefficient than the mean profile depth (MPD), a result that may be understood in terms of a simple toy model.

## I. INTRODUCTION

Any reduction of the rolling resistance (RR) between tyre and road implies a lower energy consumption [1–5]. RR reductions are therefore desirable if they can be achieved without compromising safety, e.g., by maintaining the skid resistance, and if excessive extra costs are avoided. Over the years improvements of tyre rubber’s mechanical loss properties have led to a significant lowering of the RR [6]. Activities to reduce RR by optimizing the road surface are of a newer data; these have now also led to a lowering of the RR, albeit on a much more modified scale [7]. As the result of two research projects carried out in 2011-2015 (COOEE) and 2016-2018 (ROSE) involving Roskilde University, the Danish Road Directorate, and other partners [8, 9], an asphalt mixture has been developed leading to an estimated lowering of the fuel consumption by at least 1.2% [10]. This novel KVS asphalt (“climate-friendly asphalt”) is now the standard wearing course (upper 2 cm on a road) used by the Danish Road Directorate, meaning that KVS asphalt will be applied in the future

---

\* tihe@ruc.dk

systematic maintenance and renewing of all major roads in Denmark.

Systematic studies of how the RR depends on road texture are hampered by the challenge of measuring RR accurately on real roads. While reliable measurements are definitely possible in a given situation, e.g., using the TUG trailer [11], wind, humidity, and temperature affect trailer data in ways that are not easy to compensate for. This presents a complication for any purely scientific investigation of how the road texture affects the RR. An alternative is to switch to well-controlled laboratory measurements [12–15]. In Ref. 16 we described a setup that can do this and presented RR data for a solid wheel on various sandpapers used to mimic surface textures. The present paper first describes an improved version of our setup, which now has a chamber housing the entire setup allowing for good temperature control (Sec. 2). As an example of the use of the new setup, the paper proceeds to present RR data involving extensive measurements on different 3d-printed regular surfaces for three solid rubber wheels and one pneumatic wheel (Secs. 5 and 6). The data are interpreted by means of a simple “toy” model (Sec. 4), which predicts that the RR for a given load is lower the larger the contact area between wheel and surface is. Section 7 investigates which of two texture measures are best at predicting the RR coefficient, the MPD measure or the peak fraction.

## II. ROLLING RESISTANCE AND SURFACE CHARACTERISTICS

Road-surface inhomogeneities exist on all length scales and are traditionally classified as follows [17]: *Unevenness* refers to length scales from 0.5 m to 50 m, *Megatexture* refers to length scales from 50 mm to 500 mm, *Macrotexture* refers to length scales from 0.5 mm to 50 mm, and *Microtexture* refers to length scales below 0.5 mm. A vehicle’s RR depends on inhomogeneities on all length scales. The two standard measures of surface inhomogeneities are *International Roughness Index* (IRI) and *Mean Profile Depth* (MPD). IRI is based on the quarter-car model and primarily reflects road unevenness [18], thus IRI is dominated by inhomogeneities on a length scale much longer than those of interest here. MPD is the average of two consecutive surface-height maxima relative to the average profile height, each evaluated over a stretch of 5 cm [19–21]. This is the standard measure used for quantifying the macrotexture.

As a RR predictor, the MPD suffers from the potential weakness that it does not reflect

the nature of the inhomogeneity. For instance, MPD increases if  $H$  is increased while keeping  $W$  and  $D$  constant for the regular surface of Fig. 5; the RR, however, is not expected to change in a situation where  $H$  is sufficiently large that the wheel only touches the peaks.

In his Ph.D. thesis from 2015, which studied the correlation between RR and surface texture on roads, Andersen introduced an alternative measure to better reflect the area of contact between road and tyre [22]. This novel measure was termed *Texture Penetration Area* (TPA) [22]. TPA quantifies how the profile height averaged over 10 cm changes when the lower-height cutoff is changed; for details the reader is referred to Ref. [22]. Andersen showed that for predicting the RR coefficient, TPA outperforms MPD for the majority of different combinations of tyre type, aggregation length, and enveloping function (the latter is used to smooth data before analysis) [22]. This conclusion was based on data obtained from measurements carried out at the landing strips of the former Værløse Airbase in which the RR data were obtained by means of the TUG trailer of Ejsmont [23] and the texture was probed by a laser profiler.

For the regular surface of Fig. 5, the 50% lower-cutoff TPA is given by  $TPA = HD/2(W + D)$  while MPD is given by  $MPD = HD/(W + D)$  (Eq. (4) below). Both measures are proportional to  $H$  for given values of  $W$  and  $D$ . This is difficult to justify for situations in which the wheel never touches the lower part of the texture, as mentioned above. That observation motivates the toy model developed below, which is based on a simple physical picture of the origin of RR. Henceforth, we shall not discuss the TPA measure, which has served to demonstrate that quantities exist that are better than MPD at predicting the RR coefficient of a given texture. Instead, we focus on the toy model and its comparison to experiments on regular surfaces.

### III. TOY MODEL ILLUMINATING THE ROLE OF THE CONTACT AREA (PEAK FRACTION)

This section develops a model for how the RR for given load, velocity, and wheel material depends on the characteristics of a regular surface. The model is highly idealized because it is based on comparing surfaces like those of Fig. 5 consisting of identical peaks on a regular square array.

To identify the basic physics in play, we first consider the case of perfect springs and ask:

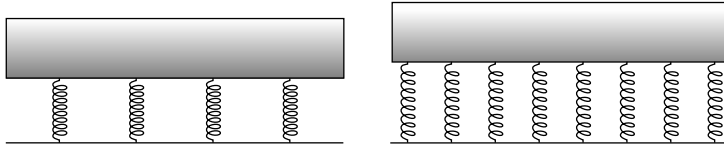


FIG. 1. Illustration of a simple spring model used for justifying the toy-model prediction for how the RR varies with peak fraction. Assuming the same load, each spring to the left stores four times as much energy as a spring to the right. If spring losses are proportional to the stored energy on the relevant time scale, this implies that the case of fewer springs to the left has a twice as large a loss as the case to the right.

How does the total energy stored in springs carrying a given weight depend on the number of springs  $N$  (Fig. 1). The energy of a single spring is  $k(\Delta x)^2/2$  in which  $k$  is the spring constant and  $\Delta x$  is the change of the spring's length from its equilibrium length. For  $N$  springs the energy is  $Nk(\Delta x)^2/2$ . The force from one spring is  $k\Delta x$  and that of  $N$  springs is  $Nk\Delta x$ . The latter is the load, i.e., independent of  $N$ . This implies that  $\Delta x \propto 1/N$  for a given load. When this is substituted into the energy expression, we see that for a given load the total energy stored in the springs, denoted by  $E_0$ , is inversely proportional to  $N$ , i.e.,

$$E_0 \propto \frac{1}{N}. \quad (1)$$

In other words, the more springs involved, the smaller is the total stored energy. For the case of Fig. 1, the right figure involves twice as many springs as the left, implying that the total stored spring energy is half of that of the left figure.

Next we argue that the same applies if the springs are not perfect, i.e., have a loss. Consider the situation of a material rolling over a surface like that of Fig. 4 and Fig. 5. In that case, assuming that all peaks have the same area  $W^2$ , for a given wheel velocity the wheel deformation takes place on a definite time scale. This time scale corresponds to a well-defined frequency range, and the material's elastic loss and storage moduli at these frequencies determine the RR. As before, the storage modulus controls the spring deformation, but now the springs are not perfect. Their loss is also controlled by the spring deformation, however, meaning that the inverse proportionality of Eq. (1) applies also for the loss. An alternative way of arriving at the same conclusion is to replace each spring in Fig. 1 by a parallel combination of a spring and a dashpot.

The toy model thus predicts that for a given load, velocity, and wheel material, the RR is inversely proportional to the number of springs involved. For the surface texture of Fig. 5 this number is proportional to the peak fraction  $P_f$  because the total area of the wheel that is at any given time in near proximity to the surface is, for geometric reasons, independent of  $P_f$ . Thus the toy model predicts that the RR is inversely proportional to  $P_f$ .

To complete the model, we note that the wheel deformation not only consists of the highly localized deformations deriving from each peak being pressed into the wheel. There is also a “global” wheel deformation, the magnitude of which depends on the load but not the nature of the surface. This global deformation also results in an energy loss, of course, but it is to a good approximation independent of  $P_f$  (it is controlled by the frequency-dependence of the elastic modulus at the wheel rotation frequency, which is incidentally much smaller than that controlling the peak-derived losses associated with indentations).

The toy model assumes that the total RR loss is a sum of the “local” and the “global” losses. This leads to the following expression for how the rolling-resistance coefficient  $\mu_{\text{RR}}$  depends on the peak fraction  $P_f$  for given load, velocity, wheel material:

$$\mu_{\text{RR}} = C_0 + \frac{C_1}{P_f}. \quad (2)$$

For a given wheel the two constants  $C_0$  and  $C_1$  in general depend on the temperature, the load, and the velocity. This expression is tested below. We find that the data are consistent with Eq. (2) and that the toy model, in fact, for a given load provides a better RR predictor than the MPD.

## IV. EXPERIMENTAL DETAILS

### A. Setup

This paper presents results obtained by means of a small-scale drum setup (see Fig. 2) capable of measuring RR with a high reproducibility. The setup allows for easy control of the load between surface and wheel, speed/rotation velocity, wheel type, surface texture, and temperature. The setup is “version 2” of a similar one described in Ref. 16 to which the reader is referred for more details. Major improvements are the addition of temperature control of the entire setup and the possibility to use 3d-printed surfaces. Other improvements

include:

- Adjustable aluminium frame as setup mount for easier maintenance and further development
- Lower drum diameter variation of steel drum, i.e, almost perfectly round drum
- Increased drum axle diameter to minimize bending
- Self-centering attachment between drum and drum axle
- Improved cantilever design for measuring the motor torque
- A belt-gear system has been introduced
- Linear rail for improved wheel-height adjustment and rigidity
- Improved load cell for measuring the load between wheel and drum

The setup determines the RR by measuring the motor torque needed to maintain a constant angular velocity [16]. A schematic illustration of the drum setup is shown in Fig. 2(c). The full setup consists of four main sections: Surface drum, wheel section, motor section, and thermo-controlled cage.

The surface drum is a steel cylinder with inner diameter 538 mm; the relative diameter variation is below 0.1 mm. The steel cylinder is attached to a 40 mm iron shaft. The 47 kg weight from surface drum and axle is supported by two bearing stands on each side, allowing for the drum to rotate with little resistance. Connected to one end of the shaft is a tachometer with a resolution of 100 impulses per full rotation.

The wheel section consists of an interchangeable wheel with ball bearings connected to a vertical linear rail via a 30 mm steel shaft. The shaft is connected to an actuator by means of a spring. Moving the actuator increases or decreases the spring tension, thereby increasing or decreasing the load between drum and wheel. The actuator is mounted on top of a load cell connected to the drum-setup frame. This cell is used to measure the load between wheel and drum.

A 110 W DC motor (*GPM12*) rotates the surface drum. The motor is supported by a bearing stands centered horizontally on the surface drum's rotational axis for free movement around the axis. The driving force from the motor is transferred to the drum shaft via belt gears with ratio 1:5. Tests have shown that in order to minimize measurement errors, it is important that all connections from the motor to the drum shaft are centered around the same rotational axis. A small pin is connected to the motor perpendicular to the drum rota-

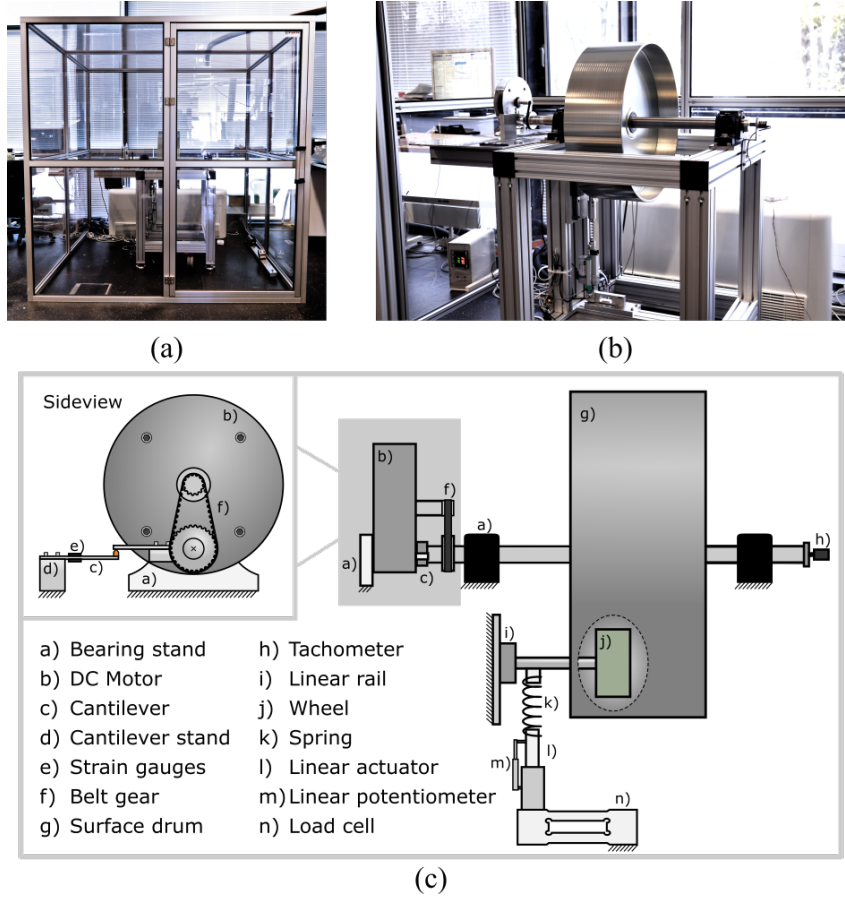


FIG. 2. The drum laboratory setup. (a) The thermo-controlled cage of see-through acrylic panels forming a cube of side length 2 m with a door housing the setup. (b) The steel drum with attached motor (left side of drum) and tachometer (right side of drum), mounted on an aluminium frame. The white box on the floor behind the frame is the air cooler and blower. The test wheel is placed to the left of the drum (hidden in the picture). (c) Schematic illustration of the drum setup and how the different components are connected.

tional axis. The distance from the rotational axis to the tip of the pin is 130 mm. When the surface drum rotates, the torque provided by the motor presses the pin against a cantilever mounted on the aluminium frame. The deformation of the cantilever due to the force from the pin is measured using two strain gauges mounted in a half-bridge configuration on the cantilever. The strain gauge readings and applied force to the cantilever are proportional [24]; the bending of the cantilever spring is thus a direct measure of the resisting force.

The thermo-controlled cage is a closed cubed room of side length 2 m made of an alu-

minium frame and 2 mm thick acrylic panels. This cage maintains the heated or cooled air around the drum setup. For temperature control, a heater and a cooler is placed inside the cage, controlled by a regulator that measures the temperature close to the wheel inside the drum. Stable temperatures can be achieved in the interval 16-39 °C with an estimated accuracy of 0.2 °C. In order to insure that the setup is in full thermal equilibrium, we wait approximately 24 hours from setting a new temperature to the start of a new measurement.

## **B. Protocol**

For given static settings, i.e., surface texture, wheel, and temperature, an experiment consists of a series of measurements of varying speed and load. When performing multiple experiments with the same static settings, the experiments are planned such that no identical experiment are performed consecutively. This is to minimize the effect of any “inherited” properties.

Two lists containing angular velocity target values and actuator position target values are given to the control software. The actuator position values set the actuator and specify the spring deformation and load on the test wheel. The angular velocity is regulated by increasing or decreasing the DC motor voltage using a PID-controller.

When the software estimates that the setup has reached a stable state, the measurements begin and logs for 10 minutes for each target value combination. The order in which speed and load are changed affects the reproducibility of the measurements, due to hysteresis in the potentiometer measuring the actuator position. This is counteracted by always only changing the actuator in direction of increasing loads. When data for a single setting have been collected, the angular velocity is changed to the next target value; when the target values for the angular velocity have been examined, a new target value for the load is set, and so on (compare Fig. 6 below).

For each experiment and velocity, a skim test is performed. This is a measurement in which the wheel just touches the surfaces drum with sufficient load to make the wheel rotate and follow the drum rotation. The idea is that the measured resistance from the skim test identifies the contribution to the RR from parasitic losses like air resistance, bearing friction, etc. We note however that, because the bearing friction depends slightly on the load, the skim test cannot determine all parasitic losses. From the information provided by



FIG. 3. Picture of the four test wheels. From the left: Nitrile butadiene rubber (NBR); Polyurethane (PUR); Continental truck tyre rubber mixture (CON).

the bearing manufacturer (SKF), it is estimated that the additional force at max loads for the setup corresponds to  $8.8 \times 10^{-3}$  Nm on the motor.

### C. Test Wheels

Three different solid wheels were used abbreviated NBR, PUR, and CON (Fig. 3).

**NBR:** is nitrile butadiene rubber, a material that is softer than PUR and CON. The rubber is cast onto an aluminum rim on which two ball bearings are attached. The wheel is 126 mm in diameter and 50 mm in width. The rubber thickness is 16 mm, the weight of the wheel is 1.2 kg.

**PUR:** is polyurethane. This specific wheel is used for indoor pallet lifters. The rubber is cast onto an iron rim on which two ball bearings are attached. The wheel is 124 mm in diameter and 50 mm in width. The rubber thickness is 10 mm, the weight of the wheel is 2.6 kg.

**CON:** is a rubber mixture aimed at reducing the RR of truck tyres produced by the tyre manufacture Continental AG, the detailed composition of which is not known to us. The rubber is glued onto an aluminum rim on which two ball bearings are attached. The wheel is 114 mm in diameter and 45 mm in width. The rubber thickness is 10 mm, the weight of the wheel is 1.1 kg.

All solid wheels are attached the setup using the same steel shaft. Changing wheel is done by simple pressing the shaft on and off and locking with an end cap.

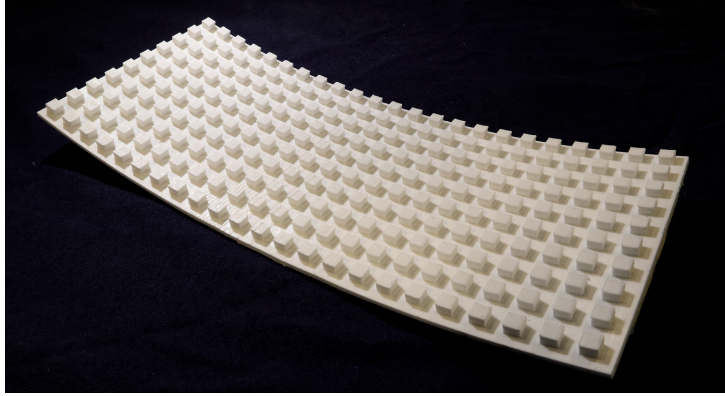


FIG. 4. Picture of a single 3d-printed surface part, printed with a curvature to fit the surface drum. A total of nine parts is made for each texture and attached to the surface drum using thin double-sided tape.

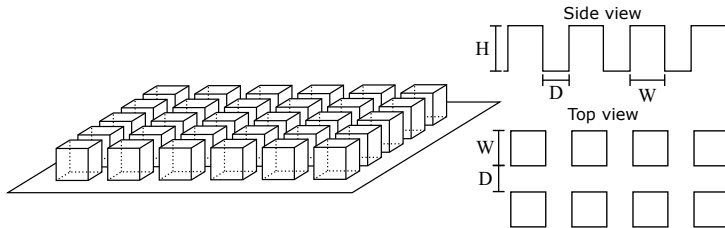


FIG. 5. Schematic illustration of the texture design defined by the following parameters: peak height ( $H$ ), peak width ( $W$ ), and distance between peaks ( $D$ ).

#### D. Textures – 3d prints

The measurements were performed on 3d-printed surfaces made of nine identical parts like the one shown in Fig. 4. An Ultimaker 3 is used to print the texture parts at layer height between 0.15-0.2 mm and 0.4 mm nozzle size. A single part takes approximately 22 hours to print. Polylactic Acid (PLA) is used as printing material due to its low cost, easy use, and high tensile strength (110 MPa [25]), compared to other common printing materials, e.g. Acrylonitrile Butadiene Styrene (ABS).

Figure 5 shows the definition of the three parameters characterizing the 3d-printed textures: peak height ( $H$ ), peak width ( $W$ ), and distance between peaks ( $D$ ). In terms of these parameters, we define the peak fraction  $P_f$  for a given texture by

$$P_f = \frac{W^2}{(W + D)^2}, \quad (3)$$

which describes the contact ratio for a tyre.

## V. RAW DATA

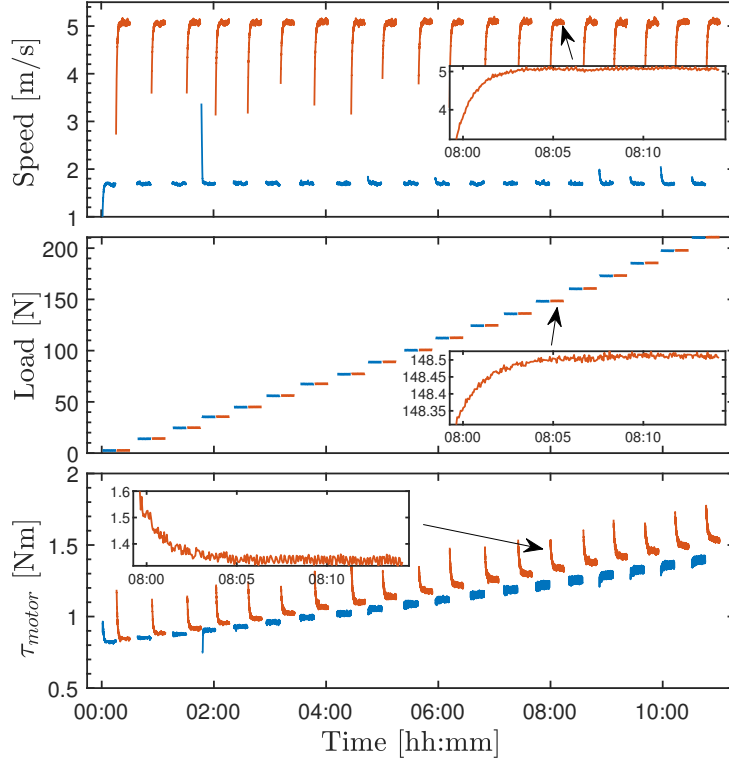


FIG. 6. Raw data from a experiment with the NBR wheel on the steel surface (i.e., with no 3d-printed surface), illustrating the protocol. Each experiment starts at a “zero” load providing the skim-test reading for determining the parasitic losses. Then one loops through the two target velocities before changing to a higher load and repeating.

The data received from the setup are the readings from the load cell strain gauges, cantilever strain gauges, and tachometer. All variables are stored with time stamps for each data point. As an example, the raw data from an experiment with the NBR wheel directly on the steel drum (corresponding to  $P_f = 1$ ) are presented in Fig. 6 showing data for 19 different loads and the two speeds used throughout (1.7 m/s and 5.1 m/s). Figure 6(a) shows the speed, while (b) and (c) show the readings from the strain gauges and tachometer,

converted into the relevant physical quantities. Note that it take a few minutes to stabilize the variables after a change has been implemented. The first measurements is at “zero” load, i.e., a load that is just large enough to ensure the wheel rotates and follows the drum; this provides the above-mentioned skim-test data used for determining the parasitic losses.

Wheel	Focus	Temp. [°C]	Surface
NBR	Load	16	Steel
			23
		T2	
		T4	
		T5	
		T6	
		T7f	
		T7b	
		T8	
		T9	
		T10	
		T11	
		T14	
			39
	Speed	23	Steel
PUR	Load	23	Steel
			T2
			T5
			T6
			T9
			T10
			T11

Wheel	Focus	Temp. [°C]	Surface		
CON	Load	16	Steel		
			23	Steel	
		T2			
		T4			
		T5			
		T6			
		T8			
		T9			
		T10			
		T11			
		T14			
					39
			Speed	23	Steel

TABLE I. Overview of the performed experiments.

Ref. name	H [mm]	W [mm]	D [mm]	MPD [mm]	PF
T2	1	2	2	0.5	0.25
T4	4	2	2	2	0.25
T5	2.5	2	3	1.5	0.16
T6	2.5	1.5	4	1.82	0.0744
T7*	2	**	**	1	
T8	12	3	3	6	0.25
T9	2.5	4	4	1.25	0.25
T10	2.5	5.19	5.19	1.25	0.25
T11	2.5	7.2	7.2	1.25	0.25
T14	1.5	1	5.15	1.26	0.0264

TABLE II. Overview of the different surface textures and parameters. \*T7 is a repeating asymmetric ramp texture; for it the notation “f” (forward) and “b” (backwards) is used. \*\*Ramp dimensions: length 5 mm, height 2 mm.

An overview of the experiments is provided in Table I. Four different wheels were tested, each at two speeds, various temperatures, and different surface textures. A overview of the surface textures is provided in Table II.

## VI. DATA ANALYSIS

This section first discusses how to extract the RR coefficient  $\mu_{RR}$  from the raw data. Thereafter we analyze how  $\mu_{RR}$  depends on peak fraction, load, and temperature. Finally, we briefly present data illuminating how reproducible the data are.

### A. Extracting the rolling resistance coefficient $\mu_{RR}$ from raw data

Figure 7 shows an example of how the RR coefficient  $\mu_{RR}$  is determined from raw data like those shown in Fig. 6. (a) shows the motor-torque data in which the vertical dotted lines mark the zero-load skim tests at the two speeds. The crosses at the bottom of the figure give the extra torque required. (b) shows the calculated  $\mu_{RR}$ . Note that it increases

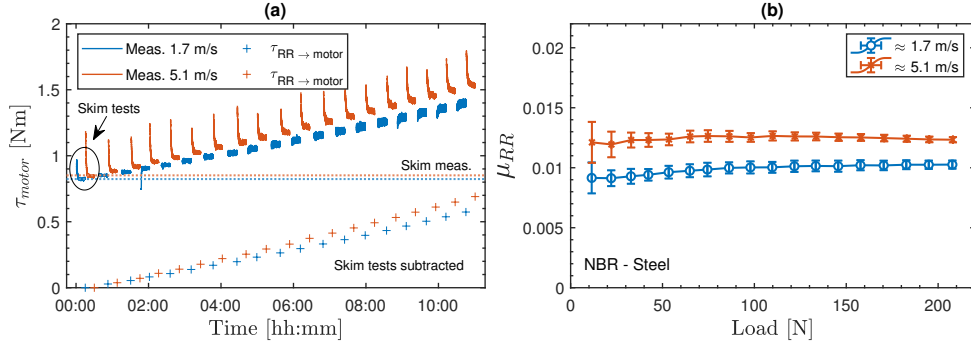


FIG. 7. Determination of the RR coefficient  $\mu_{RR}$ , exemplified by the NBR wheel on the steel surface, i.e., without any 3d-printed surface. (a) Plot of the measured motor torque  $\tau_{motor}$ . The torque contribution from the RR is calculated by subtracting the skim-test data marked as horizontal lines (bottom part of figure). (b) The RR coefficient  $\mu_{RR}$  obtained from the data in (a) plotted as a function of the load. The error bars show the standard deviation for a single data point of each experiment.

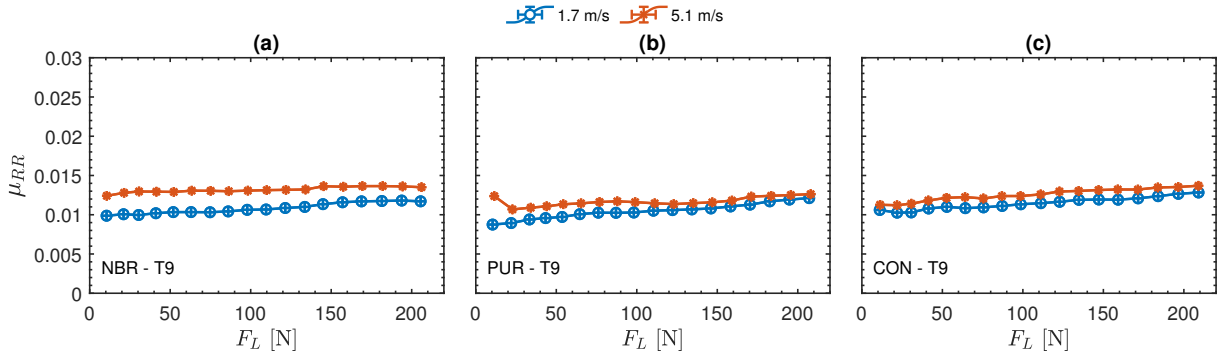


FIG. 8. The RR coefficient  $\mu_{RR}$  obtained from the measurements for all test wheels on texture T9. The error bars show the standard deviation for a single data point of each experiment.

systematically with speed, but is relatively independent of the load. An analysis of all data is given below.

## B. Mean-profile depth dependence and the RR

As an example of how data obtained by the setup may be used for testing proposed correlations, we investigate in Fig. 9 qualitatively whether the mean-profile depth (MPD) is a good RR predictor when the peak fraction  $P_f$  is varied. For the 3d-printed surfaces the MPD

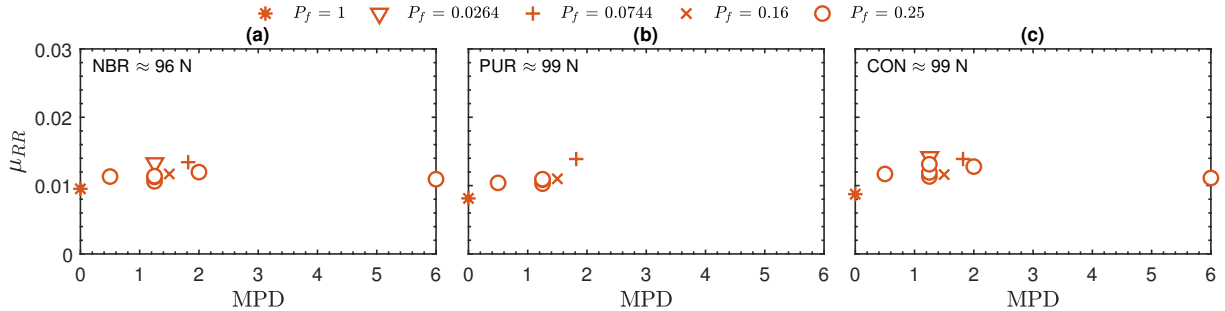


FIG. 9. RR coefficient  $\mu_{RR}$  plotted versus MPD for all three test wheels at 5.1 m/s at a single load close to 100 N. The symbols indicate the peak fraction (unit peak fraction corresponds to the steel surface that has zero MPD). No obvious correlation between  $\mu_{RR}$  and MPD is observed.

is calculated (based on idea behind the MPD ISO standard [21]) to be the number arrived at by subtracting the average peak height from the maximum peak height  $H$ . Referring to Fig. 5 this leads to

$$\text{MPD} = \frac{HD}{W + D}. \quad (4)$$

Figure 9 gives data for the four wheels obtained at a typical load and the highest speed. The circles indicate the  $P_f = 0.25$  situation for which we have most data, other symbols mark data for other values of  $P_f$ . By visual inspection we conclude that the MPD for all four wheels is not a good predictor of  $\mu_{RR}$ . This qualitative conclusion is confirmed by a statistical analysis of all measurements given below (Sec. 7).

### C. Peak-fraction dependence of the rolling resistance

Inspired by the toy model, we next investigate the peak fraction  $P_f$  as a predictor of the RR. Typical data for the four wheels are presented in Fig. 10. As for the MPD there is also for  $P_f$  only a weak dependence of the RR coefficient  $\mu_{RR}$ . However, there is a now tendency that lower peak fractions imply a higher RR coefficient. The dashed lines give the best fit to the toy model prediction Eq. (2). From such fits the two constants  $C_0$  and  $C_1$  are extracted for each wheel, load, and velocity.

Before discussing our results for  $C_0$  and  $C_1$ , we briefly consider how reliable such the extraction of  $C_0$  and  $C_1$  from data can be expected to be. In order to fit reliably to Eq. (2),

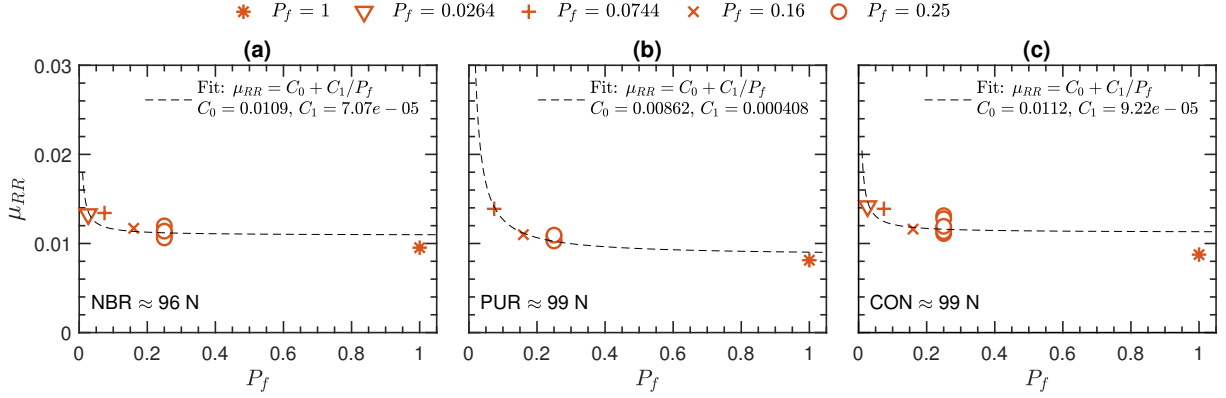


FIG. 10. The RR coefficient  $\mu_{RR}$  plotted as a function of the peak fraction  $P_f$  of all four test wheels at 5.1 m/s. The fits to data is the function derived for the toy model Eq. (2).

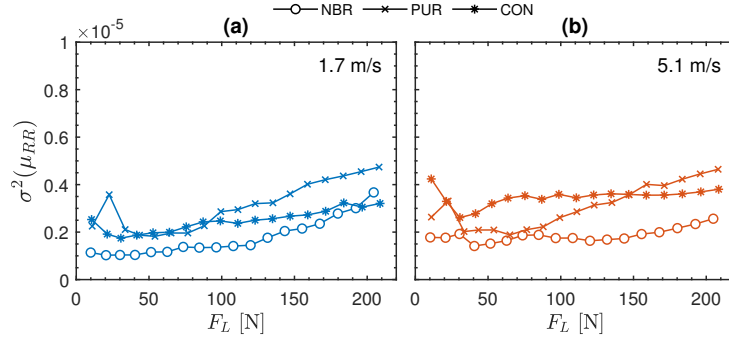


FIG. 11. Variance of the RR coefficient,  $\sigma^2(\mu_{RR})$ , for the different surface textures (excluding T7), plotted as a function of the load  $F_L$ . A large variance implies a better determination of the constants  $C_0$  and  $C_1$ , so these constants are most reliably determined for the PUR and CON wheels.

a certain variation of the RR coefficient is necessary. Figure 11 plots the variance,  $\sigma^2 = \frac{1}{N-1} \sum_{i=1}^N (\mu_{RR,i} - \langle \mu_{RR} \rangle)^2$ , of the  $\mu_{RR}$  as a function of the load for each wheel and speed setting. The largest variation is found for PUR and CON, implying that for these two wheels the  $C_0$  and  $C_1$  data are most reliable.

How are the two constants  $C_0$  and  $C_1$  expected to depend on the load? As long as the wheel mechanical properties are described by a standard linear strain-stress convolution integral, the RR force is proportional to the load for a given setup and neither  $C_0$  nor  $C_1$  depends on the load. At some point, however, the load becomes so large that linearity begins to break down. Since the constant  $C_0$  reflects the overall wheel deformation while  $C_1$  reflects the local deformation due to indentation, the strain deformations associated with

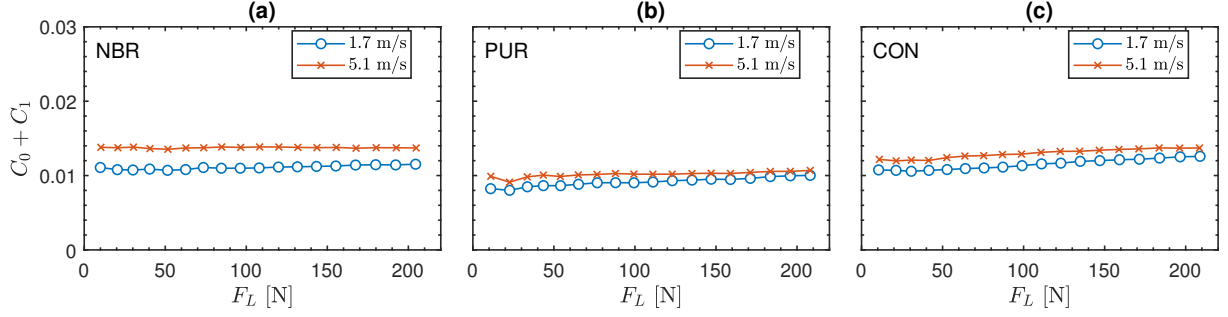


FIG. 12. The constant  $C_0$  for the fit of  $\mu_{RR}$  as a function of  $P_f$  plotted as a function of the load.

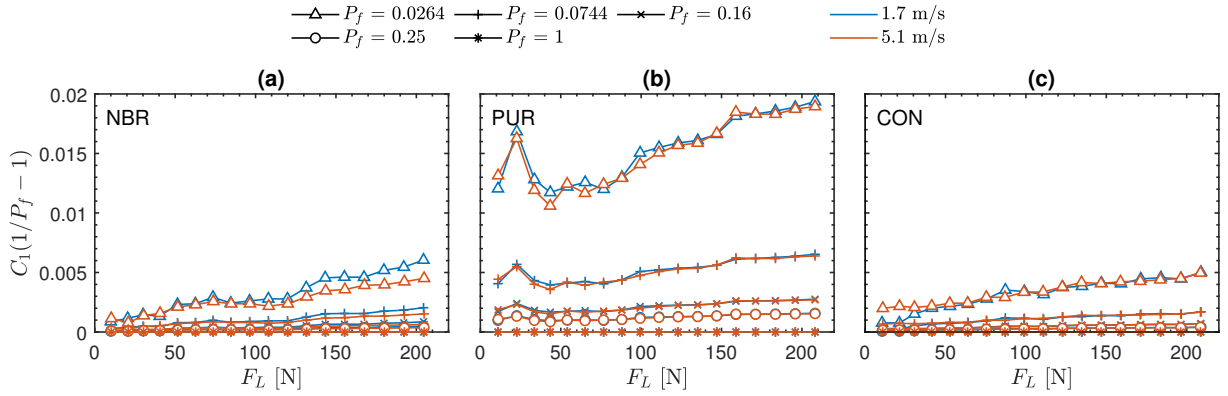


FIG. 13. The constant  $C_1$  for the fit of  $\mu_{RR}$  as a function of  $P_f$  plotted as a function of the load.

$C_0$  are much smaller than those associated with  $C_1$ . Consequently, we expect the latter to become nonlinear and thus load dependent at significantly lower loads than  $C_0$ .

Figure 12 shows the load dependence of  $C_0$ . With the exception of the pneumatic wheel (POW) that, as mentioned, gives less reliable data, we see that  $C_0$  is indeed roughly load independent. This is in contrast to Fig. 13, which shows that  $C_1$  increases consistently with load for the three solid wheels (POW with its less reliable data has  $C_1$  decreasing with increasing load).

In regard to the velocity dependence of the two constants, Fig. 12 shows that a higher velocity leads to a higher  $C_0$ , i.e., a higher RR contribution from the overall wheel deformation. The same is also observed for  $C_1$  (Fig. 12), though less pronounced. In both cases we interpret this as an effect of the magnitude of the loss, which is described by the imaginary part of the relevant frequency-dependent elastic constant: The  $C_0$  data corresponding to the overall wheel deformation reflect the wheel rotation frequency, which is considerably lower than the relevant frequency for the  $C_1$  data. From the  $C_0$  data's velocity dependence we

conclude that the relevant loss increases with frequency – consistent with this, the increase with frequency continues to the much higher frequencies relevant for  $C_1$ .

#### D. Temperature dependence of the rolling resistance

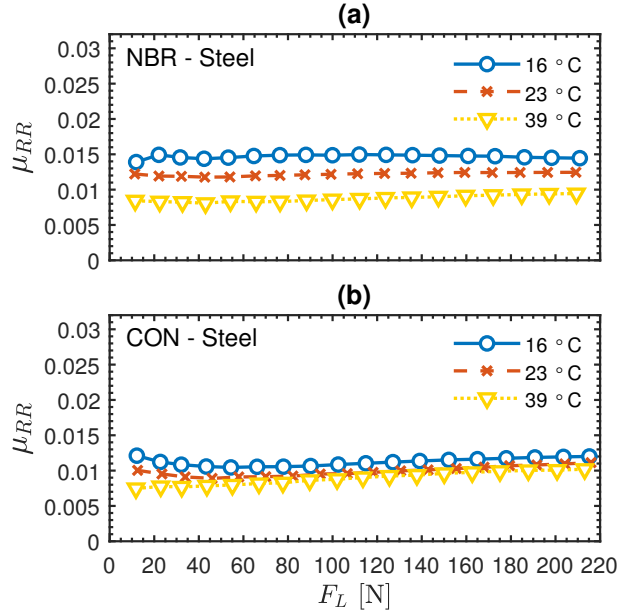


FIG. 14. RR coefficient plotted as a function of the load ( $F_L$ ) at different temperatures for the NBR and CON wheels, on the steel surface ( $P_f = 0$ ) at 5.1 m/s. The NBR wheel results at 23 °C represent a mean of eleven repeated experiments, compare Fig. 18 below.

We have also investigated the temperature dependence of  $\mu_{RR}$ . Figure 14 shows data for the three solid wheels at three temperatures, plotting the RR coefficient as a function of load. In all cases  $\mu_{RR}$  is higher, the lower the temperature is. Assuming time-temperature superposition, this finding is consistent with the  $C_0$  and  $C_1$  data given above showing that the loss increases with frequency.

#### E. Results for asymmetric surfaces

The fact that the constant  $C_1$  of Eq. (2) is not load independent indicates, as mentioned, a breakdown of linear viscoelasticity. Another way of testing this breakdown is to study the RR coming from a surface for which rolling “forward” is different from rolling “backward”.

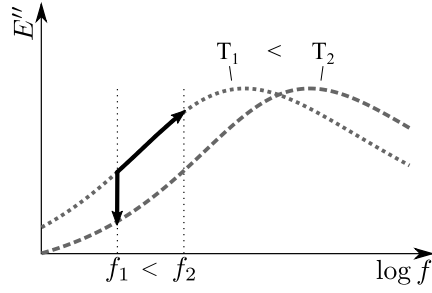


FIG. 15. Illustration of a typical frequency,  $f$ , dependence of loss modulus,  $E''$ , at two temperatures,  $T$ . The green arrow indicate an increase in  $f$ , while red arrow indicate an increase in  $T$ . Arrows indicate movements for increase in  $T$  or increase in  $f$ .

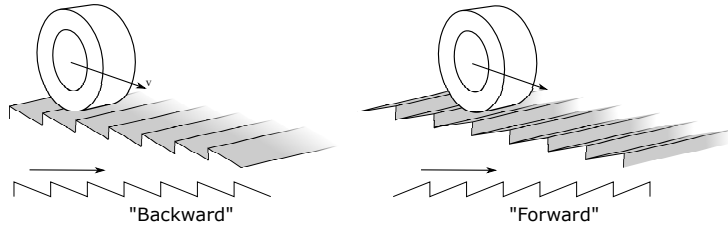


FIG. 16. The asymmetric surface texture (T7), showing what we term “backwards” and “forwards” motion.

Figure 16 shows such a surface, here with a ramp pattern. Within the context of linear viscoelasticity there is no difference between the RR coefficient of the two situations. This is tested in Fig. 17 which shows no observable difference between the two rolling directions. While this may be surprising in view of the above discussed load dependence of  $C_1$ , it does not by itself present an inconsistency in our data. We included this test here to illustrate how the

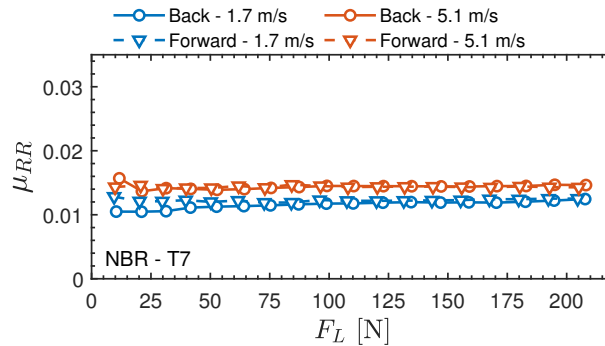


FIG. 17. RR coefficient as a function of the load of the NBR test wheel at speeds 1.7 and 5.1 m/s with the T7 surface texture.

setup and how user-specified 3d-printed surfaces may be used to investigate systematically various aspects of RR.

### F. The reproducibility challenge

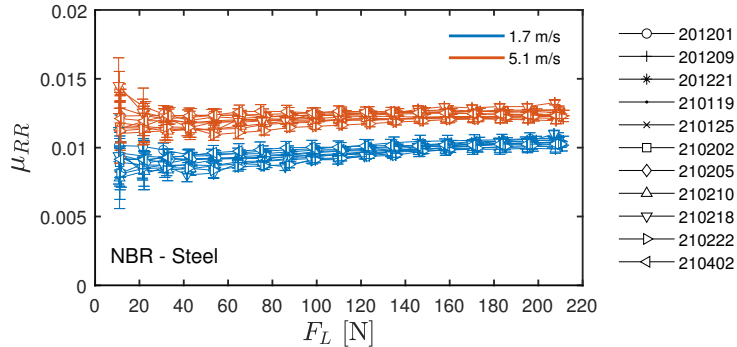


FIG. 18. RR coefficient as a function of load for the NBR test wheel at the two velocities. Results are presented for eleven experiments repeated over a period of four months. The legend shows the data for each experiment in the format YYMMDD, the error bars show the standard deviation for a single data point of each experiment.

We end this section by an analysis of how reproducible the data are. This was investigated by systematically repeating the same experiment over a period of four months for the NBR wheel at various loads and both speeds (Fig. 18). The reproducibility is better for higher loads than for smaller ones. For higher loads we find a variance of the data of order 5%, while this number is above 14% for the lowest loads.

### VII. MPD VERSUS $P_f$ AS PREDICTOR OF THE RR COEFFICIENT

In Fig. 9 we presented a qualitative analysis investigating to which degree MPD is a good RR predictor. The analysis, which was limited to a single typical value of the load, concluded that MPD appears to have little predictive value for determining  $\mu_{RR}$ . We now present a systematic statistical analysis involving all data taken at 23 °C in order to determine which of the two quantities, MPD or  $P_f$ , is best at predicting  $\mu_{RR}$ . To make things as simple as possible we employ best linear fits between  $\mu_{RR}$  and, respectively, MPD and  $P_f$ . Admittedly,

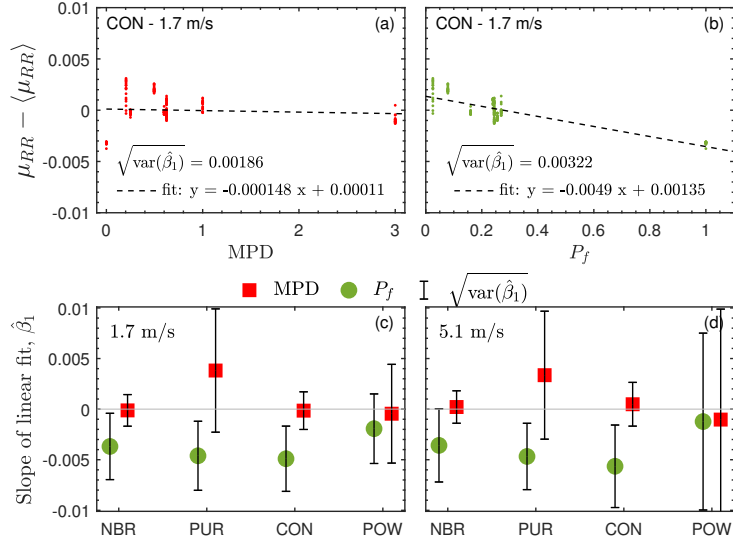


FIG. 19. Slope analysis of the data sets for all loads at 23 °C. (a) and (b) show for the CON wheel linear least-squares fit to the RR coefficient subtracted its average over the same load over all surfaces studied, plotted as a function of  $P_f$  and MPD. (c) and (d) show the slopes obtained plotted with error bars.

this ignores the toy-model prediction of a nonlinear dependence of  $\mu_{RR}$  on  $P_f$ , but as we shall see fitting with a linear function is sufficient to reach a firm conclusion.

The idea of the analysis is presented in Fig. 19(a) and (b) dealing with the CON wheel data at 1.7 m/s. Because of the load dependence of the RR which is not under investigation here, we subtract from  $\mu_{RR}$  for each data point the average RR coefficients of all surfaces with same wheel, velocity, and load; this quantity is in the figure for brevity denoted by  $\langle \mu_{RR} \rangle$ . Figure 19(a) shows  $\mu_{RR} - \langle \mu_{RR} \rangle$  as a function of  $P_f$  while (b) shows the same quantity as a function of MPD. Each such data set is least-squares fitted by a line, resulting in a slope that is denoted by  $\beta_1$ . Although (b) visually indicates a more systematic dependence than (a), the data are noisy and it is necessary to evaluate the slope uncertainty to determine whether this is statistically significant. For this we use the standard theory of linear least-squares fit that allows one to calculate the variance of  $\beta_1$  from a given data set. Figure 19(c) and (d) plot the linear slopes (points) plus/minus the square root of the slope variances (lines) for each of the two velocities. We see that for MPD the slope is zero within the uncertainty, indicating no correlation between MPD and  $\mu_{RR}$ . For the peak fraction  $P_f$  on the other hand, the PUR and CON wheels show a systematic  $P_f$  dependence of the RR

coefficient. These are the two wheels for which the variance of the RR coefficient measured for the different textures is considerably larger than for the NBR and POW wheels (Fig. 11).

In summary, a simple-minded statistical analysis reveals that in so far as there is a sizable texture dependence of the RR coefficient (PUR and CON), for a given load the peak fraction provides a better predictor than MPD. Even for the NBR wheel  $P_f$  is more convincing; only for the pneumatic POW wheel do we find no clear difference in the ability of the two quantities to predict  $\mu_{RR}$ .

## VIII. SUMMARY

This paper has reported results from an improved version of the Roskilde University RR model-validation laboratory, the first version of which was described in Ref. 16. As a test case, we have investigated how the RR of a periodic 3d-printed surface depends on peak fraction and load for three solid wheels and one pneumatic tyre, each studied at two speeds. It has been demonstrated that reliable determination of the RR coefficient  $\mu_{RR}$  is possible by means of the setup.

The data obtained are consistent with the prediction of a simple toy model according to which a low peak fraction leads to a high RR coefficient. For the toy model's "global" parameter  $C_0$  we find little load dependence, whereas the parameter  $C_1$  reflecting the local wheel deformation from the local indentations is load dependent. This shows that the breakdown of linear elasticity takes place considerably earlier for the latter parameter than for the former, which is consistent with significantly higher strains generated by indentations compared to those of the global wheel deformation. For the three solid wheels the RR coefficient increases as temperature is lowered, a finding that is consistent with the fact that  $C_0$  increases with velocity (assuming time-temperature superposition). No difference was observed between forward and backward rolling for an asymmetric triangular surface. Finally, we find that for a given load the peak fraction  $P_f$  is a better predictor of the RR coefficient  $\mu_{RR}$  than the MPD, which is often used assumed to determine  $\mu_{RR}$ . In summary, the data can be interpreted within a consistent picture accounting for the fact that the RR increases with increasing velocity, that the RR increases with decreasing temperature, and that the toy-model parameter  $C_1$  is more load dependent than  $C_0$ .

Having thus shown that the RR model-validation laboratory can be used to systemat-

ically investigate how the RR depends on texture, wheel, load, and temperature, future investigations can focus on the study of RR for more realistic surfaces and tyres. Although much remains to be done, we believe the approach of small-scale measurements in a laboratory setting provides a promising tool for understanding how the RR depends on a given surface texture. Hopefully, this approach will eventually provide the basic understanding needed for designing road pavements that reduce the RR and thus lead to substantial energy savings.

## ACKNOWLEDGEMENTS

This work was supported financially by the VILLUM Foundation's Matter (Grant No. 16515), by Innovation Fund Denmark as a part of the ROSE Project (No. 5160-00009B), and by the Danish Road Directorate. We thank Continental AG for kindly providing CON wheel.

- 
- [1] C. Bester, Effect of pavement type and condition on the fuel consumption of vehicles, *Transportation Research Record* (1984).
  - [2] J. Barrand and J. Bokar, Reducing tire rolling resistance to save fuel and lower emissions, *SAE International Journal of Passenger Cars - Mechanical Systems* **1**, 9 (2008).
  - [3] L. G. Andersen, J. K. Larsen, E. S. Fraser, B. Schmidt, and J. C. Dyre, Rolling resistance measurement and model development, *Journal of Transportation Engineering* **141**, 10.1061/(asce)te.1943-5436.0000673 (2015).
  - [4] M. Djordjevic, A. Jankovic, and B. Jeremic, Rolling resistance as the risk factor for fuel consumption, *International Journal of Vehicle Systems Modelling and Testing* **4**, 185 (2009).
  - [5] N. Cordoş, A. Todoruţ, C. Iclodean, and I. Barabás, Influence of the dynamic vehicle load on the power losses required to overcoming the rolling resistance, in *The 30th SIAR International Congress of Automotive and Transport Engineering*, edited by I. Dumitru, D. Covaciu, L. Racila, and A. Rosca (Springer International Publishing, Cham, 2020) pp. 195–202.
  - [6] Michelin, *The tyre: Rolling resistance and fuel savings* (2003), société de Technologie Michelin.

- [7] U. Sandberg, A. Bergiers, J. A. Ejsmont, L. Goubert, R. Karlsson, and M. Zöllner, *Road surface influence on tyre/road rolling resistance*, resreport (2011) MIRIAM, SP1 Deliverable No. 4.
- [8] B. Schmidt and J. C. Dyre, CO2 emission reduction by exploitation of rolling resistance modelling of pavements, *Procedia - Social and Behavioral Sciences* **48**, 311 (2012).
- [9] M. Pettinari, E. Nielsen, and B. Schmidt, *Alternative laboratory characterization of low rolling resistance asphalt mixtures* (American Society of Civil Engineers, 2017).
- [10] The Danish Road Directorate, Klimavenlig asfalt resultater, [https://api.vejdirektoratet.dk/sites/default/files/2019-11/KVS - Konklusionsnotat\\_wcag.pdf](https://api.vejdirektoratet.dk/sites/default/files/2019-11/KVS - Konklusionsnotat_wcag.pdf) (2019), accessed: 21-10-2021.
- [11] J. A. Ejsmont, G. Ronowski, B. Świeczko Żurek, and S. Sommer, Road texture influence on tyre rolling resistance, *Road Materials and Pavement Design* **18**, 181 (2017).
- [12] J. Ejsmont and S. Sommer, Selected aspects of pavement texture influence on tire rolling resistance, *Coatings* **11**, 776 (2021).
- [13] A. Bergiers, L. Goubert, F. Anfosso-Lédée, N. Dujardin, J. A. Ejsmont, U. Sandberg, and M. Zöllner, *Comparison of Rolling Resistance Measuring Equipment - Pilot Study*, resreport (2011) mIRIAM, SP1 Deliverable No. 3.
- [14] E. Riahi, C. Ropert, and M.-T. Do, Developing a laboratory test method for rolling resistance characterisation of road surface texture, *Surface Topography-metrology and Properties* **8**, 10.1088/2051-672X/ab8aa6 (2020).
- [15] J. P. C. Araújo, C. A. Palha, F. F. Martins, H. M. Silva, and J. R. Oliveira, Estimation of energy consumption on the tire-pavement interaction for asphalt mixtures with different surface properties using data mining techniques, *Transportation Research Part D: Transport and Environment* **67**, 421 (2019).
- [16] M. L. Larsen, J. J. Cesbron, F. A. Lédée, C. Ropert, J. C. Dyre, and T. Hecksher, *Laboratory for the validation of rolling-resistance models* (2021), manuscript submitted for publication.
- [17] U. Sandberg, *Tyre/road noise reference book* (INFORMEX, Kisa, Sweden Harg, Sweden, 2002).
- [18] M. W. Sayers, Two quarter-car models for defining road roughness: Iri and hri, *Transportation Research Record* , 165–172 (1989).
- [19] ASTM E1845 - 09, *Standard Practice for Calculating Pavement Macrotecture MeanProfile Depth*, Standard (American Society for Testing and Materials (ASTM), 2009).

- [20] ISO, *Characterization of pavement texture by use of surface profiles - Part 1: Determination of mean profile depth*, Standard 13473-1:1997 (International Organization for Standardization, Geneva, CH, 1997).
- [21] ISO, *Characterization of pavement texture by use of surface profiles - Part 1: Determination of mean profile depth*, Standard 13473-1:2019 (International Organization for Standardization, Geneva, CH, 2019).
- [22] L. G. Andersen, *Rolling Resistance Modelling: From Functional Data Analysis to Asset Management System*, phdthesis, Roskilde University, Roskilde, Denmark (2015).
- [23] B. Świczko-Żurek, P. Jaskula, J. A. Ejsmont, A. Kędzierska, and P. Czajkowski, Rolling resistance and tyre/road noise on rubberised asphalt pavement in poland, *Road Materials and Pavement Design* **18**, 151 (2016).
- [24] L. S. Hansen and M. L. Larsen, *An experimental investigation of rolling resistance*, mathesis, Roskilde University, Roskilde, Denmark (2017).
- [25] RS PRO, 2.85mm white PLA 3D printer filament, 1kg, <https://docs.rs-online.com/1c7d/A700000007511229.pdf>, accessed: 20-10-2021.